Abstract of "Topics in the mechanics of self-organizing systems" by Dhananjay Tambe, Ph.D., Brown University, May, 2008.

Self-organization, in one of its accepted definitions, is the appearance of non-random structures in a system without explicit constraints from forces outside the system. In this thesis two self-organizing systems are studied from the viewpoint of mechanics. In the first system — semiconductor crystal surfaces — the internal constraints that lead to self-assembly of nanoscale structures on silicon-germanium (SiGe) films are studied. In the second system — actin cytoskeleton — a consequence of dynamic self-organization of actin filaments in the form of motion of micron-sized beads through a cytoplasmic medium is studied.

When Ge film is deposited on Si(001) substrate, nanoscale features form on the surface and self-organize by minimizing energy contributions from the surface and the strain resulting from difference in lattice constants of the film and the substrate. Clean Si(001) and Ge(001) surfaces are very similar, but experiments to date have shown that atomic scale defects such as dimer-vacancies self-organize into vacancy lines only on Si(001). Through atomic simulations, we show that the observed difference originate from the magnitude of compressive surface strain which reduces formation energy of the dimer-vacancies. During initial stages of the film deposition, the surface is composed of steps and vacancy lines organized in periodic patterns. Using theory of elasticity and atomic simulations we show that these line defects self-organize due to monopolar nature of steps and dipolar nature of the vacancy lines. This self-organized pattern further develops to form pyramidal islands bounded with (105) facets and high Ge content. Mismatch strain of the island is then reduced by incorporation of Si from the substrate surrounding the island leaving behind trenches whose depth is proportional to the basewidth of the island. Using finite element simulations we

show that such a relationship is an outcome of competition between elastic energy and surface energy. Some experimental studies also report observation of steeper (103) and (104) facets on pyramidal islands. Using numerical simulations we derive a phase diagram which shows that the steeper facets are stabilized because they provide better relaxation of mismatch strain with only slight increase in surface energy.

In the second system, the actin cytoskeleton is a key structural and propulsion element of eukaryotic cells. Micron-sized "cargoes", which under pathological conditions include bacteria, are propelled by dynamic self-organization of the actin filaments. Recently it is shown that the trajectories of a bacterium, *Listeria monocytogenes*, propelled by actin filaments are *periodic*; implying that the organization of actin filaments impart an effective force that spins about the axis of the bacterium. We show that the motion of spherical beads is also non-random; the effective force has an additional degree of freedom due to the spherical symmetry of the bead. Agreement of the theoretical trajectories with experimental observations suggest that the actin-based motility can be *generally* described using deterministic equations. We also propose microscopic basis for the effective force model which can guide development of microscopic theory to predict the long term trajectories of actin propelled objects.

Topics in the mechanics of self-organizing systems

by

Dhananjay Tambe

B. E., Mechanical Engineering,
University of Pune, 1999
M. Tech., Mechanical Engineering,
Indian Institute of Technology (Madras), 2001
Sc. M., Applied Mathematics,
Brown University, 2004

A dissertation submitted in partial fulfillment of the
requirements for the Degree of Doctor of Philosophy
in the Division of Engineering at Brown University

Providence, Rhode Island
May, 2008

This dissertation by Dhananjay Tambe is accepted in its present form by the Division of Engineering as satisfying the dissertation requirement for the degree of Doctor of Philosophy.

Date _____ _____

Professor Vivek B. Shenoy, Adviser

Recommended to the Graduate Council

Date _____ _____

Professor L. Ben Freund, Reader

Date _____ _____

Professor Eric Chason, Reader

Approved by the Graduate Council

Date _____ _____

Shiela Bonde
Dean of the Graduate School

Vita

Dhananjay Tambe was born on March 5, 1978 in Andersul, India. He studied up to 10th grade in Rangubai Junnare High School and two years of junior college in Sciences Division of Karmaveer Thorat Hiray Murkutay College. He then joined Pravara Rural Engineering College, Pune University, in 1995 for his Bachelors degree in Mechanical Engineering. After his graduation in 1999, Dhananjay joined Indian Institute of Technology, Madras for Masters degree in Machine Design. He then continued research activities at Eicher Motors as Assistant Manager and in Indian Institute of Sciences, Aerospace Engineering Department as research assistant. He joined Mechanics of Solids and Structures program at Brown University in fall 2002. En route to his Ph.D. he received Masters degree in Applied Mathematics in 2006. After his Ph.D he plans to do postdoctoral research at the Harvard School of Public Health with the aim of career in scientific research.

Acknowledgments

Graduate courses and interactions with professors, postdoctoral associates and fellow graduate students provided me with ability to analyze information conveyed by physical systems from a broad perspective of mechanics of materials. I owe much of my understanding and approach to my thesis advisor Professor Vivek Shenoy. His enthusiasm in different topics in Physics and dedication to a problem at hand have guided my thoughts about scientific research in general. I will be always grateful to Vivek for the faith he has shown in me while seeking solutions to many interesting problems. I was also fortunate to have worked with Cristian, his strategies for tackling research problems have often lead me in making smart plans. Interactions with Dhiraj, Ashwin, Vishal, Guru, Ganesh, Nikhil, Ram, Bharathi, Mandar, Jing, Prabhat, and Don were quite useful.

In the winter semester of 2006, I had an opportunity to work with Rob Phillips group at Caltech. During this period, Rob, Hernan, Mandar and all other Phillips lab members helped me understand many concepts in experimental and theoretical cell mechanics. This training gave me enough confidence in experimental microbiology which later on helped me in making a detailed protocol for bead motility assay. I would like to thank Professor Freund and Professor Tang for their encouragement and help in preparing this protocol. Without timely help from Liz, Deepa, Yifeng and Hyeran, it would have been difficult to carry out numerous procedures for this assay in such a short amount of time.

I would like to express my gratitude to Professor Freund and Professor Chason for taking time out of their busy schedule to review and comment on my research work.

All these years of study would not have been possible without the firm support and encouragement of my parents, my brother and my vahini.

To Aee and Dada

Contents

⋆ Parts of this thesis have appeared in the following publications:

Shenoy, V. B., Tambe, D. T., Prasad, A., and Theriot, J. A. (2007), 'A kinematic description of the trajectories of *Listeria monocytogenes* propelled by actin comet tails', *Proceedings of the National Academy of Sciences of the USA*, **104** (20), 8229–8234.

Tambe, D. T., Ciobanu, C. V., and Shenoy, V. B. (2005), 'Self-assembly of steps and vacancy lines during the early stages of Ge/Si(001) heteroepitaxy', *Applied Physics Letters*, **87**(25), 251908–1:3.

Tambe, D. T., and Shenoy, V. B. (2004), 'On the energetic origin of self-limiting trenches formed around Ge/Si quantum dots', *Applied Physics Letters*, **85**(9),

1586–1588.

Ciobanu, C. V., Tambe, D. T., and Shenoy, V. B. (2004), 'Comparative study of dimer vacancies and dimer-vacancy lines on Si(001) and Ge(001)', *Surface Science*, **556**(2-3), 171–183.

List of Tables

List of Figures

Chapter 1

Introduction and overview

Self-organization, in one of its accepted definitions, is the appearance of a non-random structures in a system without explicit constraints from forces outside the system. For scientists, self-organization can probably be appreciated best by pondering on how inhospitable the universe would be had the values of fundamental physical constants been slightly different. Nature has presented self-organization in many forms one of which is a means to construct functional units and this form has been studied by researchers from sciences and humanities in different contexts. Two of such contexts discussed in this thesis are, atomic scale structures and nanoscale morphological features on silicon-germanium (SiGe) crystal surfaces and dynamic organization of actin proteins leading to propulsion of micron-sized objects inside cell cytoplasmic medium.

In the field of semiconductor devices, keeping up with the trend of Moore's Law has been at center stage for the last 40 years. Currently we are a little ahead of that trend and still there is plenty of room to go even smaller in size, with the main limitation being the production of a perfect array of identical structures. To this end, self-assembly is the only cost effective solution to produce high density devices on an industrial scale. Strain-driven self assembly in Ge/Si(001) has received particular

attention, as 3D islands formed in this system can be integrated as devices that are compatible with well-developed Si technology. Typically, an array of tiny charge confining SiGe structures (quantum dots) are produced by depositing Ge film epitaxially from the vapor phase onto the Si substrate. Since Ge has a larger lattice constant than Si, the deposited film is in compression. Many chemical and morphological changes take place in the film to relieve the mismatch strain. The morphological changes are in the form of atomic scale and nanoscale defects on a flat crystal surface which interact through long range anisotropic elastic fields. Due to the characteristic fields of the defects, their formation energy is lowest if they occur in a specific pattern. This is the mechanical basis for self-assembly of quantum dots.

In a biological context, examples of self-organization are abound ranging from fractal patterns to embryogenesis. At the level of a single eukaryotic cell, one of the fundamental questions investigated by scientists since the early 1950's (eg. Mitchison (1950)) is how does the cell takes its first step in the form of pseudopods. At the core of this process is a novel self-organizing system, "actin cytoskeleton". A minimum of four cytoskeletal proteins (actin, arp2/3, capping protein and cofilin) utilize the chemical energy released during hydrolysis of ATP to form an actin motor, which works on dynamic self-organization of these set of proteins to carryout propulsion.

In this thesis, two important aspects of self-organization are discussed: its *internal constraints* and its *consequence*. Both aspects will be presented from the point of view of the mechanics of solids and structures. In the first four chapters we will study the *internal constraints* that lead to self-organization of nanoscale features on semiconductor crystal surfaces. In the last chapter, we will study the *consequence* which is motion arising from dynamic self-assembly of the actin network around the objects of a few microns in size.

1.1 Self-organization on semiconductor crystal surfaces

Atoms on semiconductor crystal surfaces minimize free energy of those surfaces in a process known as "reconstruction" where the atoms move from their bulk truncated positions to reduce the number of dangling bonds. Reconstruction introduces anisotropy in certain physical properties of the surface such as diffusion, stress, and energy, which gives directionality to the self-assembly of surface defects. In Chapter 2, we will look at the (001) surface of Si and Ge which has surface atoms reconstructing to form dimer rows as shown in Fig. 1.1.

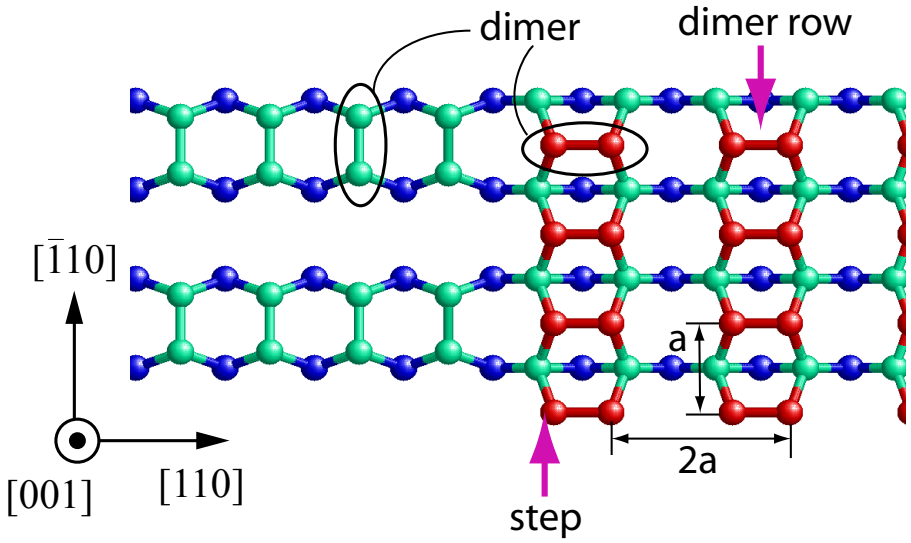

Figure 1.1: 2×1 reconstruction of Si or Ge (001) surface which consists of rows of dimers. Color of the atoms denote the out-of-plane distance. The step shown separates two planes that have a height difference of one monolayer. The upper terrace has dimers oriented normal to the dimers on the lower terrace.

The Si(001) surface has a tensile stress along the dimer bonds ($\sigma_{\parallel}$) and a compressive stress along the dimer rows ($\sigma_{\perp}$) with stress anisotropy $\sigma_{\parallel} - \sigma_{\perp} = 70$ meV/Å^2 (Webb *et al.* (1991)). Although the clean Si(001) and Ge(001) surfaces are very similar, experiments to date have shown that dimer-vacancy (DV) (where one of the

dimers from 2×1 reconstruction shown in Fig.1.1 is missing) defects self-organize into vacancy lines (VLs) on Si(001), but not on Ge(001). In Chapter 2, we identify three energetic parameters which characterize the DVs on the two surfaces: the formation energy of a single DV, the attraction between two DVs in adjacent dimer rows, and the strain sensitivity of the formation energy of DVs and VLs. Through the strain sensitivity analysis, we show that there is a reduction in the formation energies of defects when a compressive strain is applied to the surface. This is key to the formation of VL on Ge(001) surface.

If a layer of atoms is removed from the surface, as shown in Fig. 1.1, then a step is formed at the interface of the two terraces. During the initial stages of epitaxial growth, the surface contains such steps and VLs. In Chapter 3 we derive analytic expressions for optimum spacing between these line defects for different periodic arrangements. We have shown that the mathematical representation of a step as a line of monopoles and a VL as a line of dipoles predicts the periodic pattern observed by Sutter *et al.* (2003). This pattern further develops into a pyramidal island. The as-grown islands have high Ge content and hence to reduce their strain energy, Si atoms migrate from the substrate surrounding the island to alloy the pyramid. As a result, a few nanometer deep trenches form around the island. Since the area surrounding the island is highly stressed, the trench also relaxes the mismatch strain of the island. In Chapter 4 it is shown that the linear relationship between the island size and trench depth is determined by the competition between elastic energy and surface energy.

The quantum dots are bounded by facets that are reconstructed to minimize the surface energy. However, during reconstruction new electronic surface states are created which impede application of the quantum dots in an electronic circuit. For SiGe quantum dots, this problem is overcome by capping the islands with Si. However, the capping process seems to stabilize pyramidal islands with much steeper ((103) and

(104)) facets compared to the usual (105) that is observed during growth experiments. In Chapter 5 we show that pyramidal islands with (103) and (104) facets are preferred in the region where the (105) pyramid is not observed to be stable (Rastelli *et al.* (2001)). To generate the phase diagram of pyramidal quantum dots, we have also obtained a reconstruction for (104) surface using a stochastic optimization technique called the genetic algorithm. The reconstruction proposed for the (104) surface, at the level of Tersoff's empirical potential (Tersoff (1989)), has a surface energy density close to that of the (105) surface in an equi-biaxially compressed state. Further experiments and calculations with higher level potential are required to locate the region in the phase diagram which is more accessible to the Si overgrowth process.

In this thesis, all the molecular static calculations are done with atomic interactions defined using an empirical potential (Tersoff (1989)). The reason for this choice lies in the computational power required to extract the energetic parameters of the surface defects without being influenced by the proximity of the boundaries. For example, the long-range behavior of VL-VL interactions require slabs that are at least 10 layers thick. Due to a the large number of atoms the calculations of interaction of line defects using density functional or tight-binding theory remained prohibitive until recently, (Gavini *et al.* (2007)). The Tersoff potential for Si and Ge (Tersoff (1989)), on the other hand, gives a satisfactory description of defects on the (001) surface (Zandvliet (2000), Poon *et al.* (1992), Liu and Lagally (1996)) and it is a widely accepted potential for Si-Ge systems with a large number of atoms. However, the nature of defect interactions which gives rise to the self-assembly described in this thesis are independent of the model for interatomic potential.

1.2 Motility arising from the self-organization of cytoskeletal proteins

Actin cytoskeleton is a key structural element of eukaryotic cells. Amongst a multitude of its functions, the actin cytoskeleton is also used in intracellular transport of "cargoes" such as organelles and vesicles. In this transport machinery, energy gained by actin polymerization is utilized in displacing the "cargo" as well as deforming the actin filaments. It is also readily hijacked by various pathogens to move within and across the cells. Ever since Theriot *et al.* (1992) discovered that the motility machinery of *Listeria monocytogenes* is actin cytoskeleton, the biochemistry of this process has been in the forefront. Loisel *et al.* (1999) found that there are a set of four minimum proteins (see Fig. 1.2) required to make this actin polymerization motor function. Now such actin-based motility can also be mimicked using some special protein (eg. VCA, ActA, WASP) coated polystyrene beads, oil drops, or vesicles.

Several theoretical models have been proposed to understand the force-velocity relationship and some transient phenomena of actin based motility (eg. Gerbal *et al.* (2000), Carlsson (2001), Dickinson and Purich (2002), Mogilner and Oster (2003), Alberts and Odell (2004), Dickinson (2006)). But none of the models describe the variety of trajectories (which are traces of the growth front of the actin network) that these actin propelled cargoes display when their motion is confined to a plane. Recently Shenoy *et al.* (2007) observed that the shape of the trajectories of *Listeria monocytogenes* have a striking similarity to the trajectories of a particle propelled by a constant torque that is spinning at a constant rate about the direction of propulsion. However, this model cannot explain the trajectories displayed by spherical and elliptical beads. In Chapter 6 we show that the trajectories of spherical beads are actually

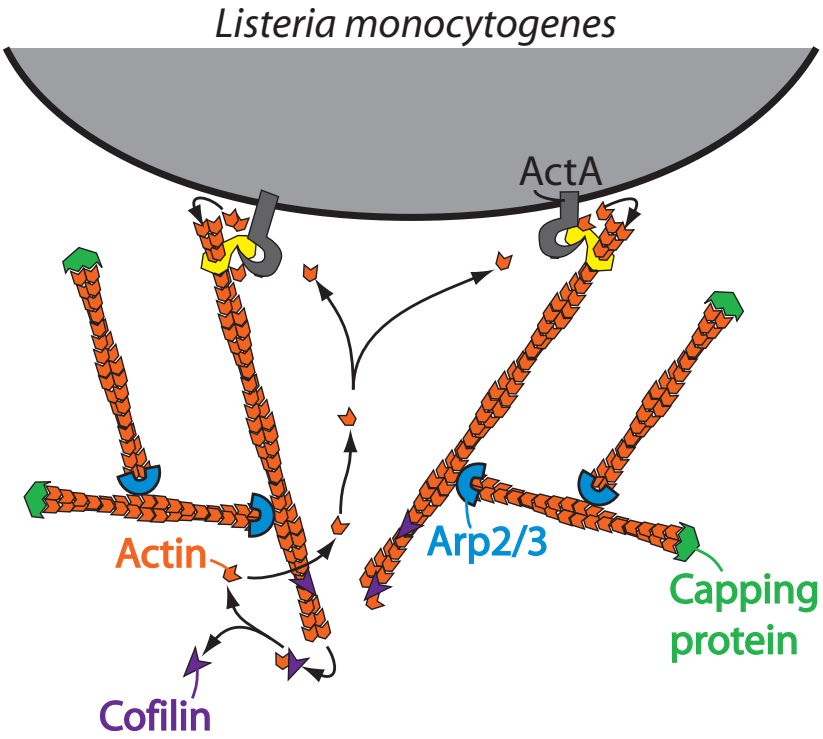

Figure 1.2: Minimum set of proteins participating in the dynamic self-assembly that lead to the actin based motility of *Listeria monocytognes* (Loisel *et al.* (1999)). Actin is the main structural unit of the polymerization motor and it has the faster polyermizing (barbed) end facing the cargo, and a slow polymerizing (pointed) end away from the cargo. Cofilin severs actin monomers from the trailing end of the actin filament and keeps a steady source of actin monomers to the pointed end. Arp2/3 forms a stable nucleus which can grow into a filament and also create branches in existing filaments. Capping proteins block polymerization of the barbed ends which are not in proximity of the cargo surface so that most of the polymerization gives rise to propulsion.

similar to those of *Listeria* except for a difference in the value of their mean curvature. We have generalized the model originally proposed for the motion of *Listeria* to explain the trajectories of spherical beads. Apart from showing that the phenomenon arising from dynamic self-organization of actin filament can *generally* be described using deterministic equations, we also propose microscopic mechanisms that can give

rise to the kinematics assumed in our model. We propose that while uniform polymerization of actin filaments against a flat cargo surface will give rise to a straight trajectory, inhomogeneous polymerization and relaxation of the bending energy of the filaments can provide motion along curved paths. For a curved cargo like spherical beads, the freely growing filaments in front of the cargo becoming part of the actin network located at the rear of the cargo can also account for the kinematics predicted by our model. This chapter also contains the implications of the kinematic as well as the microscopic model on motion of elliptical beads and oil drops. The propositions made in this chapter can guide development of microscopic theory which that could predict long term trajectories of actin propelled objects. Some predictions like the existence of relative motion between the spherical bead and its comet tail can be readily verified with simple *in vitro* experiments.

Chapter 2

Self-assembly of dimer-vacancies on Si-Ge(001) surface

2.1 Introduction

In the early stages of Ge/Si(001) growth, the surface changes its reconstruction from the 2×1 structure to a $2\times N$ pattern, which consists of an array of long, parallel lines of dimer vacancies. It has recently been shown that the $2 \times N$ reconstruction can be an excellent template for the nanofabrication of 1-dimensional structures with unique electronic transport behavior (eg. Li *et al.* (2001), Wang *et al.* (2002), Miki *et al.* (1999), Owen *et al.* (2003)). From a fundamental point of view, the current state-of-the-art in scanning tunneling microscopy has helped renew the general interest in the $2 \times N$ structures on Si(001). For example, Rastelli *et al.* (2003) have recently discovered that the $2\times N$ reconstruction on the Ge-covered Si(001) surface disappears upon Si capping, confirming in an ingenious way the role played by the mismatch strain in determining the stability of the vacancy lines.

Rapid progress has been made after the discovery of the $2 \times N$ structure (eg. Mo

and M.G. (1991), Köhler *et al.* (1992)), and two authoritative reviews summarizing the present understanding of the growth of germanium films on Si(001) have been published (eg. Liu *et al.* (1997), Voigtländer (2001)). Dimer vacancies (DVs) form easily on the Si(001) surface, but they only organize into vacancy lines (VLs) when there is a sufficient amount of Germanium deposited (close to 1 ML). The mismatch strain created by epitaxial deposition increases the number of dimer vacancies per unit area, and the interactions between these vacancies become important at sufficiently high vacancy concentrations. The interaction between two DVs is long-range repulsive when the DV's belong to the same dimer row, but weakly attractive when they belong to adjacent dimer rows (eg. Chen *et al.* (1994), Weakliem *et al.* (1995)). Such anisotropy of the interactions determines the alignment of the DVs in the direction perpendicular to the dimer rows. This physical picture for the origin of the $2 \times N$ reconstruction has emerged from the experimental work of Chen *et al.* (1994). The mechanism for the formation of vacancy lines is consistent not only with experiments done on other epitaxial systems (e.g., Bi/Si(001) Park *et al.* (1994)), but also with the observations of the Si(001) surface with metal impurities such as Ag (Chang *et al.* (1996)) or Ni (Zandvliet *et al.* (1995), Koo *et al.* (1995)).

While the physical origin of the vacancy lines on Si(001) has been elucidated (Chen *et al.* (1994)), it remains a puzzle as to why vacancy lines are not normally observed on the very similar Ge(001) surface. The fact that the Ge(001) surface is virtually defect free (eg. Chey and Cahill (1997), Zandvliet (2003)) suggests that the formation energy of the vacancies on Ge(001) is substantially larger than that of the vacancies on Si(001). Quantitative data from atomic-scale calculations on the Ge system is not available, although the need for such calculations was emphasized almost a decade ago in the work of Yang *et al.* (1994). The purpose of our paper is to address the differences between Ge(001) and Si(001) concerning the formation of dimer-vacancies

and their self-assembly into vacancy lines. The work presented in this chapter fits well into the current efforts of Zandvliet (2003) explain the differences between the two technologically important surfaces.

We have calculated the formation energies of point and line defects on the (001) surfaces and their dependence on applied strain, using empirical potential models (Tersoff (1988, 1989)) for interactions . The results obtained offer an explanation for the differences between the vacancies on Si(001) and Ge(001) and are consistent with experimental findings; moreover, these results could foster further work based on more accurate descriptions of the atomic interactions such as tight-binding or density functionals. We have considered both the heteroepitaxial system Ge/Si(001) for different values of Ge coverage, as well as pure Si and Ge surfaces under external strain. While the results concerning the epitaxial Ge/Si(001) systems have been previously obtained in different forms (eg. Pandey (1985), Tersoff (1992), Liu and Lagally (1996)), the variation of the energetic parameters of DVs and VLs on the (001) surface with applied strains has not been systematically addressed in the past. Such a study of the energetics of defects on (001) surfaces as a function of applied strain is presented here. Two new results obtained in our calculations are:

(a) the formation energy of the dimer-vacancies on Ge(001) and its decrease under compressive, biaxial strains. In the case of unstrained surfaces, we have found that the formation energy for single DV on Ge(001) is three times larger than the corresponding value for the single DV on Si(001). Therefore, in order for the formation energy of a single-DV on Ge(001) to become negative, a large compressive strain should be applied, either biaxially or in the direction of the dimer rows.

(b) the formation energy of vacancy lines on Si(001) and Ge(001) as a function of

applied strain. Using a simple model based on the interactions of nearest-neighbor vacancies in a VL, we have also identified the formation energy of a single DV and the attractive interaction (binding) between two DVs in adjacent dimer-rows as the dominant contributions to the formation energy of a VL.

The organization of this chapter is as follows. In section 2.2 the competition between the formation energy of the vacancy lines is outlined and their elastic interactions as the general energetic mechanism that leads to the appearance of the $2 \times N$ reconstructions. In contrast to interpretations of Liu *et al.* (1997), we will see that there is no long range attraction between the vacancy lines, as their interactions are purely repulsive. As in most other studies to date, the formation of vacancy lines is regarded here as a purely thermodynamic phenomenon, thus the kinetics concerning the diffusion of vacancies during their alignment are not considered. In section 2.3 the computational details of the total energy calculations based on Tersoff potentials (Tersoff (1988, 1989)) are described. The next two sections are devoted to the formation energies and repulsion strengths for single-vacancy lines (VLs) on Ge-covered Si(001) (section 2.4) and for different types of VLs on pure Si(001) and Ge(001) (section 2.5). We investigate the formation energies of individual dimer vacancies on (001) surfaces and their strain dependence to identify the differences between the defects on Si and Ge surfaces. The possible relevance of these results for future experimental work will be discussed in section 2.5. The conclusions are summarized in section 2.6.

2.2 *Energy of vacancy lines on* $2 \times N$ *surfaces*

The $2 \times N$ reconstruction is a structural pattern on the (001) surface of Si, characterized by the periodic lengths $2a$ and Na, where N is a positive integer and $a = 3.84$Å is the lattice constant of the unreconstructed Si(001) surface. This reconstruction is obtained by eliminating every N-th dimer from each dimer row, such that the dimer

vacancies created in this manner are in registry with one another and form straight lines perpendicular to the dimer rows. To lower the number of dangling bonds at the surface, the second-layer atoms below the dimer vacancy rebond such that they are fully coordinated, at the cost of introducing some surface stress (eg. Pandey (1985), Tersoff (1992), Liu and Lagally (1996)). Depending on the preparation details of the surface, other types of atomic structures of VLs can be obtained (eg. Liu *et al.* (1997), Park *et al.* (1994), Chang *et al.* (1996), Zandvliet *et al.* (1995), Koo *et al.* (1995), Men *et al.* (1995), Smith *et al.* (1996), Feil *et al.* (1992)). In this section we focus on the general features of the energetics of the $2 \times N$ surface, without reference to a specific atomic structure. We start by partitioning the surface energy into a contribution from the 2×1 surface and a contribution from the vacancy lines:

$$\gamma_{2\times N} = \gamma_{2\times 1} + \frac{\lambda}{L_x}, \tag{2.1}$$

where $\gamma_{2\times N}$ and $\gamma_{2\times 1}$ denote the surface energies of $2 \times N$ and 2×1, respectively, λ is the energy per unit length of the vacancy lines, and $1/L_x$ is the density of lines in a periodic array of VLs with a spacing of $L_x \equiv Na$. Eq. (2.1) defines the energy per unit length λ of the vacancy lines as an excess energy with respect to the defect-free 2×1 surface. We note that the energy of the vacancy lines λ includes the formation energy of the lines, as well as their elastic interactions. Guided by the early work of Marchenko and Parshin (1980), we expect the interactions to be inversely proportional with the square of the separation between VLs, so that the line energy λ can be written as

$$\lambda = \Lambda + \frac{\pi^2}{6}\frac{G}{L_x^2}, \tag{2.2}$$

where Λ is the formation energy of a VL and G is the strength of the repulsion between lines. The numerical factor $\pi^2/6$ arises since we treat a periodic array of

line defects rather than two isolated VLs. Using Eq. (2.2) in (2.1) we can write the surface energy of the $2 \times N$ reconstruction as a function of N:

$$\gamma_{2\times N} = \gamma_{2\times 1} + \frac{\Lambda}{Na} + \frac{\pi^2}{6}\frac{G}{N^3 a^3} \tag{2.3}$$

where we have used the fact that $L_x = Na$.

Analyzing Eq. (2.3), we note that:

(a) if Λ is positive then $\gamma_{2\times N} > \gamma_{2\times 1}$, so the 2×1 structure is energetically favorable.

(b) for any $\Lambda < 0$, Eq. (2.3) has only one minimum located at:

$$N = N^* \equiv \frac{\pi}{a}\sqrt{\frac{G}{(-2\Lambda)}} \tag{2.4}$$

For the case of negative formation energy Λ, a typical plot of the surface energy difference $(\gamma_{2\times N} - \gamma_{2\times 1})$ as a function of N is shown in Fig. 2.1. The condition $\Lambda < 0$ is sufficient to ensure the stability of the $2 \times N$ reconstruction (over the 2×1 structure), because for $N = N^*$ we have $\gamma_{2\times N} - \gamma_{2\times 1} = (2/3)\Lambda < 0$. This analysis of Eq. (2.3) shows that, *irrespective of the atomic-scale features of the VLs, the* $2\times N$ *reconstruction is always stable when the formation energy of a vacancy line is negative*. The optimal value of N is given by the competition between the formation energy Λ and the strength G of the repulsive interactions, as shown in Eq. (2.4). The magnitudes of Λ and G are determined by atomic-scale details, and incorporate the effects of the VL structure (eg. Pandey (1985), Tersoff (1992)), wetting layer composition (eg. Liu *et al.* (1997), Liu and Lagally (1996), Voigtländer and Kästner (1999)), as well as the anisotropy of surface stress and relaxation (eg. Tersoff (1992), Liu and Lagally (1996)).

The following two sections are devoted to the computation of the line formation energies and repulsion strengths for various VL structures, and to the investigation

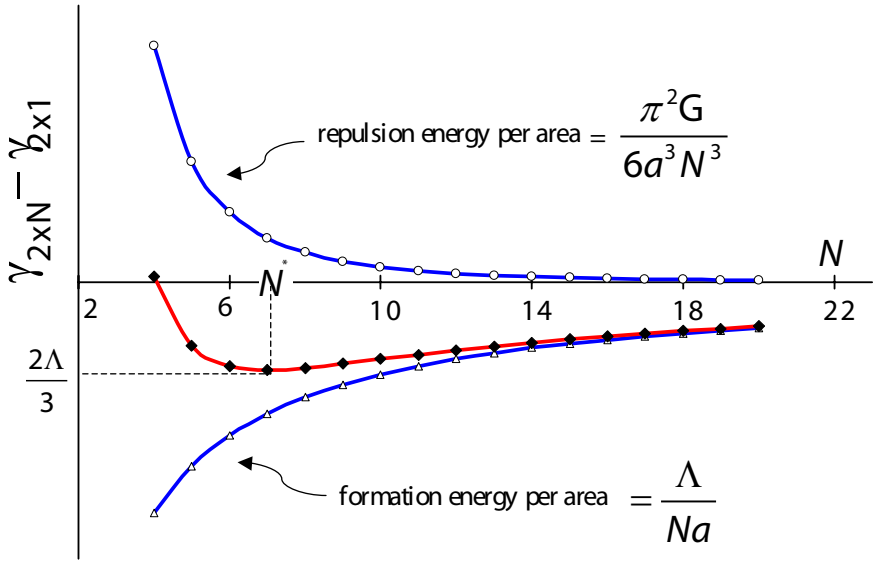

Figure 2.1: A typical plot of the surface energy difference $\gamma_{2\times N} - \gamma_{2\times 1}$ as a function of N (solid diamonds). The minimum of the surface energy $\gamma_{2\times N}$ is determined by the competition between the negative formation energy (triangles) and a repulsive (positive) interaction between the vacancy lines (circles).

of the behavior of these quantities as a function of germanium coverage and applied strain. Before we proceed with the numerical results, we draw a connection with previous work on the energetics of the $2 \times N$ surface. The above theory of the energetics of the vacancy lines is similar to Men and Hsu (1998), Natori *et al.* (1997), since it explicitly considers the competition between the (negative) formation energy of a VL and the repulsive (positive) interaction between the VLs as the physical origin of the $2 \times N$ structure. Men and Hsu (1998) however, emphasize the surface stress anisotropy, and the treatment of the two-domain (i.e. $2 \times N$ and $N \times 2$) surfaces obliterates the simplicity of the VL energetics outlined above.

A word of caution is due concerning the mechanisms of formation of the $2 \times N$ reconstruction proposed by Voigtländer and Kästner (1999) and in the review article Liu *et al.* (1997). In Voigtländer and Kästner (1999), the conclusions based on the energetic competition between "trench formation" and "strain relaxation" are fortuitous, since the N-dependence of each of these two energetic contributions is incorrect [1]. The sign of the "trench energy" and the magnitudes of the two energetic contributions are also incorrect, though these aspects are probably outside the scope of the simple Frenkel-Kontorova model used in Voigtländer and Kästner (1999). Liu *et al.* (1997) asserts that "in the dimer-row direction the VL-VL interaction is short-range repulsive and long-range attractive", which seems plausible given the behavior of the $\gamma_{2\times N}$ in the limit of large N. However, we note that what appears to be an attractive long-range interaction between VLs is in fact the formation energy of one VL per unit cell of the $2 \times N$ surface. As shown in the sections to follow, the VL-VL interaction takes a purely repulsive form once the vacancy line energy is extracted from the surface energy.

[1] We believe that the energetic competition that determines the $2 \times N$ reconstruction is described by Eq. (2.3).

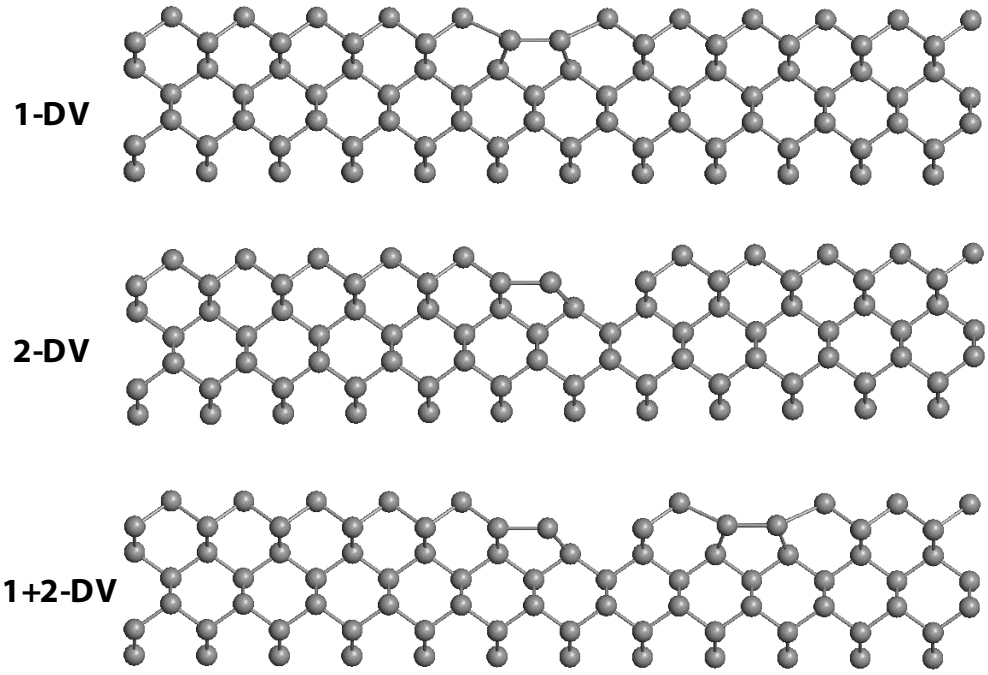

Figure 2.2: Atomic structures of the vacancy lines, with the nomenclature given in Wang *et al.* (1993). The 1+2-DV complex is made of a 2-DV complex and single DV, separated by one dimer row.

2.3 Computational Details

2.3.1 Structure of the vacancy lines

In the terminology of Wang *et al.* (1993), the vacancy lines considered here are made of 1-DV, 2-DV and 1+2-DVs, as shown in Fig. 2.2. The choice of these structures is motivated by the experimental observations of the atomic-scale details of vacancy lines on different surfaces: the 1-DV structure is present on Ge-covered Si(001) (eg. Liu *et al.* (1997), Pandey (1985), Tersoff (1992), Liu and Lagally (1996)), while lines with the 2-DV and 1+2-DV configurations have been observed on Si(001) with Ni (eg. Zandvliet *et al.* (1995), Koo *et al.* (1995)) and Ag (Chang *et al.* (1996))

impurities, as well as on radiation-quenched Si(001) (eg. Men *et al.* (1995), Smith *et al.* (1996)).

2.3.2 *Total energy calculations*

Accurate calculations of the long-range behavior of the VL-VL interactions are very demanding, requiring slabs that are both long ($N > 10$) and thick (at least 10 layers). Earlier density-functional and tight-binding calculations were restricted to thin slabs with 4–6 moving layers, due to limitations in computational power (eg. Tsai *et al.* (1997), Kim and Chen (2002), Yu and Oshiyama (1995)). At present, density-functional and tight-binding calculations have become possible (Oviedo *et al.* (2002), Li *et al.* (2003)), though they remain computationally expensive for the purpose of determining the long-range interactions between line defects. Such calculations are still prohibitive for point defects on the surface, since these defects require simulation cells that are large in all three directions. As more studies would probably become available for various types of vacancy lines in the near future, it is worth pointing out that a good test for their total-energy convergence is to check that the line energies λ can be fitted well with the inverse-square power law given by Eq. (2.2). Such a test would also indicate whether or not the chosen thickness of the computational slab is sufficient. This type of analysis is routinely performed for steps on crystal surfaces (eg. Jeong and Williams (1999), Zandvliet (2000), Giesen (2001) and references therein) in order to determine the step formation energy and step-step interactions, but it has almost never been applied to the case of vacancy lines.

Since we will investigate vacancy lines as well as individual vacancies (point defects) on the surface, we employ empirical potentials to model the atomic interactions. We use the Tersoff potential for Si and Ge (Tersoff (1988, 1989)), since it satisfactorily describes the structure and energetics of steps on (001) surfaces (eg. Zandvliet (2000),

Poon *et al.* (1992)), as well as the surface energies of the $2 \times N$ reconstructions (eg. Liu and Lagally (1996)). Despite known limitations, the empirical potential described in Tersoff (1989) represents a widely accepted standard for Si-Ge systems with large numbers of atoms. Our aim is restricted to a meaningful comparison (rather than an accurate determination) of the properties of dimer vacancies on Si(001) and Ge(001). For this purpose, the use of the Tersoff potential is appropriate, and even desirable as a starting point.

For simulation cells with a thickness of 200Å and values of N in the range $4 \leq N \leq 36$, we have performed conjugate-gradient structural optimizations. From the minimized total energy E of the atoms in the simulation cell we compute the surface energy $\gamma_{2\times N}$. When there is only one atomic species in the simulation cell (e.g., Si), the surface energy is given by:

$$E = ne_{Si} + \gamma_{2\times N} L_x L_y, \tag{2.5}$$

where e_{Si} is the bulk cohesion energy per Si atom and n denotes the number of atoms in the simulation cell that are allowed to relax. For the case of two atomic species in the simulation cell, the surface energy is given by:

$$E = n_{Ge}\mu_{Ge} + n_{Si}\mu_{Si} + \gamma_{2\times N} L_x L_y, \tag{2.6}$$

where n_{Ge}, μ_{Ge} (n_{Si}, μ_{Si}) are the number of atoms and chemical potential of Ge (Si). Since we are considering deposition on Si(001), the chemical potential of Si is set to the bulk cohesion energy per atom e_{Si}. For low Ge coverages (1–3ML), the chemical potential of Ge (μ_{Ge}) depends on the deposition conditions and is not known, although its value is usually set to the bulk cohesion energy of (unstrained) Ge, e_{Ge} (eg. Liu *et al.* (1997), Liu and Lagally (1996), Voigtländer and Kästner (1999), Yu

and Oshiyama (1995)). Exceptions are found in the work of Oviedo *et al.* (2002) and Li *et al.* (2003), who carefully define a reference state from which the surface energies are measured; the procedure in Oviedo *et al.* (2002), Li *et al.* (2003) is equivalent to computing the chemical potential of Ge based on a wetting layer composition assumed to be thermodynamically stable. From the results of Oviedo *et al.* (2002), Li *et al.* (2003) we infer that for a pure Ge wetting layer (no intermixing), setting $\mu_{Ge} = e_{Ge}$ is a poor approximation for monolayer and sub-monolayer coverages, but it becomes reasonable for 2 ML and 3 ML of Ge coverage. Though we use $\mu_{Ge} = e_{Ge}$ in the present work, we will also address the effects of changing the chemical potential of Ge.

2.4 Vacancy lines on the Ge-covered Si(001) surface

In this section, we calculate the surface energy of the $2 \times N$ surface with 0–3 ML Ge coverage, then compute the line formation energy and the VL-VL interactions. Our results for the surface energies are very close to the ones originally obtained by Liu and Lagally (1996); the deviations are due to the slightly different versions of the Tersoff potentials [2]. What differentiates the results of this section from those of Liu and Lagally (1996) is that we pursue the determination of the line formation energy and VL-VL interaction strength, whereas Liu and Lagally address the interplay between surface stress and stoichiometry.

Using Eq. (2.1), we have computed the line energy λ and plotted it as a function of the inverse square of the line spacing $(1/L_x^2)$ in Fig. 2.3. The line energy λ is a linear

[2]The parameter λ_3 of the Tersoff potential given in Tersoff (1988) is set to zero in Tersoff (1989), thus modifying the original T3 parametrization for pure Si. Here, we have found it convenient to use a form of the interactions that reduces to Tersoff (1988) in the limit where only one atomic species is present in the simulation cell.

WL	Λ(meV/Å)	G (eVÅ)	N^*
0 ML	−20.44	15.562	
1 ML	−27.95	15.603	14
2 ML	−129.92	13.526	6
3 ML	−134.61	13.818	6
1.5 ML (i)	−11.03	7.968	15
2 ML (i)	−12.20	8.541	15

Table 2.1: Formation energy Λ of the vacancy lines and their repulsion strength G calculated with the Tersoff potential Tersoff (1989) for the Ge-covered Si(001) surface. The first four rows correspond to a wetting layer (WL) of pure Ge 0–3 ML thick, and the last lines represent two intermixed (i) structures with the composition given in Liu and Lagally (1996). The last column shows the values of N^* obtained from Eq. (2.4).

function of $1/L_x^2$ for each integer value of the Ge coverage between 0ML and 3ML (Fig. 2.3). This behavior confirms the expectation (Eq. (2.2)) that the interactions between the vacancy lines are dipolar in nature (Marchenko and Parshin (1980)). The parameters of the linear fits shown in Fig. 2.3 give the line formation energy Λ (intercept) and the line-line repulsion strength G (slope), and are listed in Table 2.1. The table also includes the fitting parameters for two cases of intermixed wetting layer compositions. We have verified that the the dipolar character of the line-line interactions is not changed by intermixing in the wetting layer. These intermixing cases are considered here only for the purpose of illustration, as the actual structure of the wetting layer at given Ge coverage is under debate (eg. Rastelli *et al.* (2003), Liu and Lagally (1996), Voigtländer and Kästner (1999), Yeom *et al.* (1997)). The data in Table 2.1 shows that for both of the wetting layer compositions considered (pure Ge or intermixed), the formation energy decreases strongly with increasing Ge coverage, which is consistent with previous findings (Liu *et al.* (1997)). The repulsion strength G is very sensitive to the WL composition, as the elastic interactions are largely transmitted through the first few layers: different intermixed compositions affect the

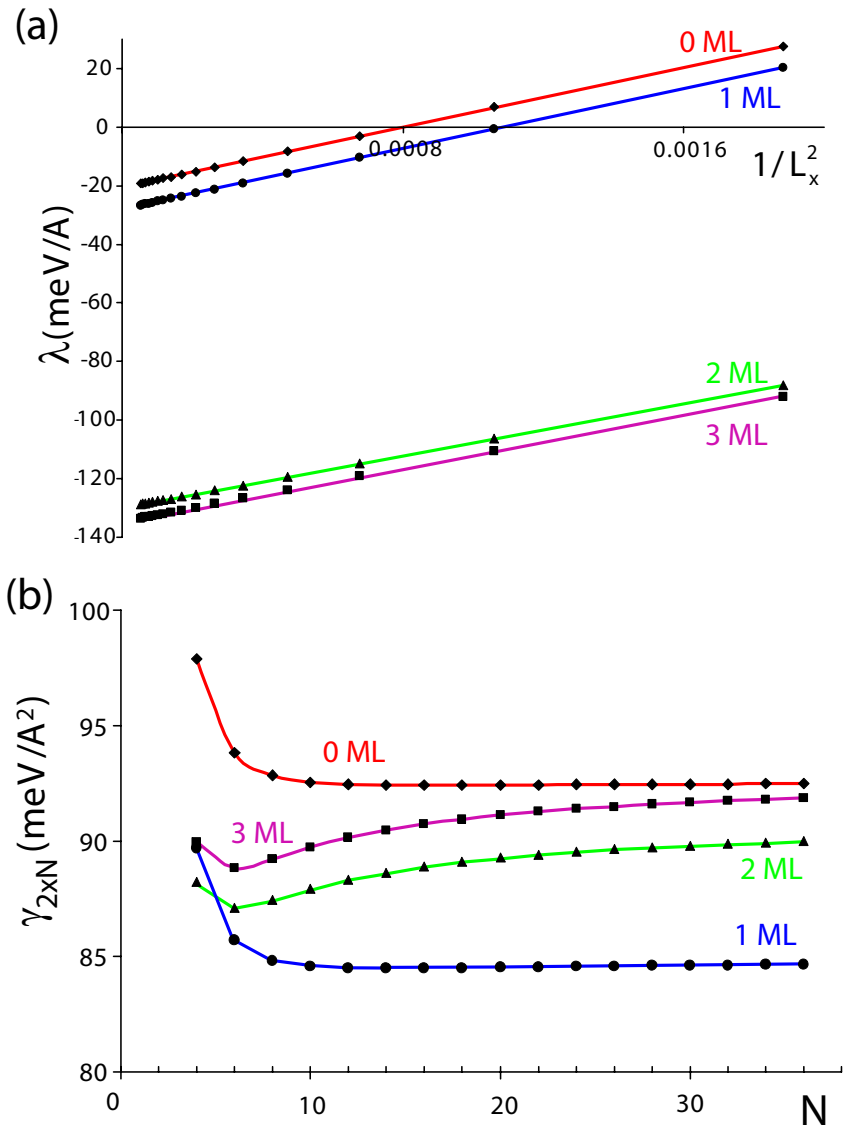

Figure 2.3: Vacancy line energy λ plotted as function of inverse square of the line spacing $(1/L_x^2)$ for different Ge coverages: 0 ML (diamonds), 1 ML (circles), 2ML (triangles) and 3 ML (squares). The inset represents the energy of the $2 \times N$ surface as a function of N Liu and Lagally (1996), computed with the Tersoff potential T3 Tersoff (1988, 1989).

elastic properties of the film and thus the strength of the repulsive interactions.

The trends shown in Table 2.1 are well understood (eg. Liu *et al.* (1997)) and physically meaningful, although we emphasize that the exact values of the formation energy Λ are influenced by the choice of the chemical potential for the deposited Ge atoms. By taking finite differences in Eq. (2.6), we note that a change $\delta\mu_{Ge}$ in the chemical potential of Ge introduces a change $\delta\gamma_{2\times N}$ in the surface energy of the $2\times N$ structure given by:

$$0 = n_{Ge}(\delta\mu_{Ge}) + (2Na^2)(\delta\gamma_{2\times N}), \tag{2.7}$$

where we have used the values for the periodic lengths, $L_x = Na$ and $L_y = 2a$. Similarly, for a 2×1 surface with the same area, thickness, and WL composition, we have

$$0 = (2 + n_{Ge})(\delta\mu_{Ge}) + (2Na^2)(\delta\gamma_{2\times 1}), \tag{2.8}$$

where the number of Ge atoms was increased by 2, as no dimers are missing from the 2×1 structure. Subtracting Eq. (2.8) from Eq. (2.7) and using Eq. (2.2) we obtain

$$\delta\mu_{Ge} = Na^2\left(\frac{\delta\Lambda}{Na} + \frac{\pi^2}{6}\frac{\delta G}{N^3a^3}\right), \tag{2.9}$$

where $\delta\Lambda$ and δG are the changes in the line formation energy and repulsion strength generated by the change in chemical potential $\delta\mu_{Ge}$. From Eq. (2.9) in the limit of large N, we find that $\delta\Lambda = \delta\mu_{Ge}/a$ and $\delta G \equiv 0$. Therefore, modifications of the Ge chemical potential amount to shifting the line formation energy while leaving the VL-VL interactions unchanged –a conclusion which is independent of the model used to describe the atomic interactions.

In summary, we have computed the line formation energies and the repulsion strengths for certain Ge coverages and WL compositions. As shown in Table 2.1, the line formation energy Λ is sensitive to the WL thickness and composition, while the

VL-VL interactions are mostly sensitive to composition. To gain further insight into how strain affects the interactions and self-organization of vacancy lines, we will now consider $2 \times N$-reconstructed surfaces of pure species (either Si or Ge) under external applied strain.

2.5 Defects on Si(001) and Ge(001) under applied strain

The study of vacancy lines and dimer vacancies on uniformly strained Si(001) and Ge(001) surfaces has two technical advantages: (a) the ambiguity regarding the value of chemical potential of Ge is removed, and (b) the uncertainties related to intermixing in the wetting layer obviously do not arise when studying systems with only one atomic species. Therefore, the study of defects on clean surfaces under external strain allows for a more direct comparison between Si(001) and Ge(001).

2.5.1 Vacancy lines on strained surfaces

The surface energy of the $2 \times N$ structure under external strain can be computed using formula (2.5) in which the bulk cohesion energy is also a function of the applied strain. The in-plane deformations are applied along the dimer rows ($\epsilon_x \equiv \varepsilon,\ \epsilon_y = 0$), perpendicular to the dimer rows ($\epsilon_x = 0,\ \epsilon_y \equiv \varepsilon$), or equibiaxially ($\epsilon_x = \epsilon_y \equiv \varepsilon$). For each type of deformation we vary the strain in the range $-2\% \leq \epsilon \leq 2\%$, by appropriately scaling the atomic coordinates. In this range of deformation, we find that the line formation energy Λ is a linear function of strain:

$$\Lambda(\epsilon_x,\ \epsilon_y) = \Lambda_0 + \Lambda'_\alpha \varepsilon, \tag{2.10}$$

	VL structure	G_0 eVÅ	Λ_0 meV/Å	Λ'(meV/Å) uniax (x)	uniax (y)	equibiax.
Si	1-DV	15.56	−20.56	4868.5	−412.55	4468.5
	2-DV	5.01	51.57	2879.3	−822.08	2067.7
	1+2-DV	33.33	30.56	6530.6	−1228.5	5354.2
Ge	1-DV	11.12	32.48	4112.0	−559.72	3559.3
	2-DV	4.00	69.613	2543.1	−846.11	1709.6
	1+2-DV	24.36	104.64	5617.1	−1396.5	4230.8

Table 2.2: Repulsion strength G_0 and line formation energy Λ_0 at zero strain for the vacancy line structures shown in Fig. 2.2. The last three columns show the strain sensitivity Λ' of the line formation energy for different types of in-plane deformation. The results in this table are obtained using the Tersoff potentials Tersoff (1988, 1989) .

where Λ_0 is the line formation energy in the absence of strain, and the subscript α denotes the uniaxial strain along different directions ($\alpha = x$, or $\alpha = y$) or the equibiaxial strain ($\alpha = xy$). A consequence of the linear relation described in Eq. (2.10) is that the biaxial strain sensitivity Λ'_{xy} is the sum of the two sensitivities Λ'_x and Λ'_y that correspond to the uniaxial deformations:

$$\Lambda'_{xy} = \Lambda'_x + \Lambda'_y. \tag{2.11}$$

For the VL structures shown in Fig. 2.2, we have computed all the strain sensitivities Λ'_α ($\alpha = x,\ y,\ xy$) independently, and found that formula (2.11) holds to within 1–2% of Λ'_{xy}. These strain sensitivities are listed in Table 2.2, along with the formation energies Λ_0 and repulsion strengths G_0 computed in the absence of strain. The strain-dependence of the line formation energy Λ is strongly anisotropic. As shown in Table 2.2, the strain sensitivity Λ'_x along the dimer row is positive, while Λ'_y is negative and several times smaller (up to one order of magnitude for 1-DV vacancy lines) in magnitude than Λ'_x. This indicates that for all the vacancy structures

shown in Fig. 2.2, the rebonding in the second layer plays a crucial role in determining the strain dependence of the line formation energy. In the absence of strain, the bonds that "bridge" the second-layer atoms in the vacancy lines are stretched compared to their bulk values, and are especially sensitive to strains applied parallel to them. Therefore, compressive strains along the dimer rows will decrease the amount of stretch in those bonds, lowering the formation energy of the vacancy lines. This correlation between atomic bonding and formation energy is consistent with the ones given previously for the case of 1-DV lines (see, for example Liu *et al.* (1997), Pandey (1985), Tersoff (1992), Liu and Lagally (1996)). On the other hand, an uniaxial strain applied perpendicular to the dimer rows only indirectly affects the formation energy of the vacancy lines via a Poisson-type effect: a stretch along the y-direction creates a small compressive stress in the x-direction, which in turn lowers the line formation energy.

While the formation energy Λ of the vacancy lines varies significantly with applied strain, the VL-VL repulsion strength G shows a weak strain dependence, changing by less than ten percent for the values of strain considered here. The reason for the weak strain-dependence of the VL interactions is that the relaxations that occur after applying external strains to an already relaxed $2 \times N$ surface are rather small, since no bonds are broken or formed. Consequently, the VL–VL interactions are not substantially affected by external strains as long as these strains remain in the small-deformation regime given by Eq. (2.10).

By comparing the Si and Ge data (Table 2.2) for each type of VL structure, we find several systematic trends: (a) the repulsion strengths G are stronger for Si than for Ge, (b) the formation energies Λ_0 are smaller for Si than for Ge and (c) the strain sensitivities along dimer row (Λ_x) and biaxial (Λ_{xy}) are larger for Si than for Ge. Most notably, the formation energy of a single-DV line on Si(001) is negative, while for the

case of Ge(001) it is positive. While there is a possibility that this sign difference between Si(001) and Ge(001) might be due to artifacts of the empirical potential, it is consistent with the observation of self assembly of DVs on Si(001) (Feil *et al.* (1992)) and not on Ge(001) (Yang *et al.* (1994), Chey and Cahill (1997), Zandvliet *et al.* (1998), Fukuda and Ogino (1998)). Some of these trends are related to the formation and binding of individual dimer vacancies, as will be shown in the next section.

The occurrence of the vacancy lines is a consequence of the strongly anisotropic interactions between the individual dimer vacancies, coupled with the preference of the DVs to diffuse along the dimer rows. As discovered by Chen *et al.* (1994), two DVs that belong to the same dimer row repel one another, while DVs in adjacent dimer rows experience a weak attraction at short distances. This finding was confirmed by other independent experiments (Zandvliet *et al.* (1995), Chang *et al.* (1996)), as well as by theoretical studies (Weakliem *et al.* (1995)). Thus the physics of vacancy lines is intrinsically related to the formation, interactions and diffusion of individual dimer-vacancies. In what follows, we show how the strain dependence of the formation energy of the VLs is linked to the behavior of individual dimer vacancies under strain.

2.5.2 Dimer vacancies on Si(001) and Ge(001)

In this section, we compute the formation energy of three types of DVs on Si(001) and Ge(001), as well as the attractive energy of two vacancies placed in adjacent dimer rows. In the case of Si(001), a similar calculation was performed by Wang *et al.* (1993), and has served as useful reference for many subsequent investigations. In contrast, we have found no similar studies for the formation energies of defects on Ge(001). Here we perform such a study using the Tersoff potential (Tersoff (1989)), and identify the differences between the vacancies on the two surfaces, Si(001) and Ge(001). We denote the formation energy of a DV complex by u, and that of an

isolated pair of complexes lying in adjacent dimer rows (called a *bound pair* form here on) by u_p. The binding energy of the pair is defined [3] as the difference between the pair's formation energy and the formation energies of two isolated DVs:

$$w \equiv u_p - 2u. \tag{2.12}$$

We have calculated the formation and binding energies for different vacancy complexes, and have listed the results in Table 2.3.

We shall first discuss the formation energy u, and compare our results with those of Wang *et al.* (1993), which were obtained using density-functional calculations coupled with an empirical potential. The advantages and disadvantages of such a coupling scheme are clearly discussed in the original paper Wang *et al.* (1993). In the case of 1-DV vacancy on Si(001), we find the formation energy of single DV's $u \approx 0.19$ eV, in good agreement with the value of 0.22 eV reported in Wang *et al.* (1993). For the other vacancy complexes, the agreement with Wang *et al.* (1993) is poor because the empirical model Tersoff (1988) does not accurately capture the relaxations of the under-coordinated second-layer atoms that are present in the 2-DV and 1+2-DV complexes. Due to this limitation, the Tersoff potential (Tersoff (1988)) predicts that the 2-DV complex is unstable with respect to the formation of two isolated single DVs, $u_{2-\mathrm{DV}} > 2u_{1-\mathrm{DV}}$. We find however that the empirical potential is still able to predict that a 2-DV and a 1-DV on the same dimer row can bind to form a 1+2-DV complex (i.e. $u_{1+2\mathrm{DV}} < u_{2-\mathrm{DV}} + u_{1-\mathrm{DV}}$), though the binding energy for the 1+2DV complex is about half the value obtained from Wang *et al.* (1993). In the case of Ge(001) surface, the potential (Tersoff (1989)) fares better than the silicon parametrization (Tersoff (1988)) in describing the stability of DV complexes. Both the 2-DV and 1+2-DV vacancies on Ge(001) are stable against breaking into isolated

[3] With this definition, the negative sign is retained to indicate the stability of the bound pair.

	DV complex	u (eV)	w (eV)	$\frac{u+w}{2a}$ (meV/Å)	Λ (meV/Å)
Si	1-DV	0.186 (0.22)*	−0.281 (−0.1)†	−12.37	−20.56
	2-DV	0.505 (0.33)*	−0.106	51.94	51.57
	1+2-DV	0.619 (0.42)*	−0.322	38.66	30.56
Ge	1-DV	0.549	−0.239	38.75	32.48
	2-DV	0.699	−0.136	70.37	69.61
	1+2-DV	1.218	−0.330	110.00	104.64

* Wang *et al.* (1993)
† Weakliem *et al.* (1995)

Table 2.3: Formation energies u of vacancy complexes and binding energies w corresponding to a bound pair of vacancy complexes situated in adjacent dimer rows. The last two columns give the line formation energies estimated using formula (2.13), as well as the ones obtained from total energy calculations (Table 2.2). The results of Wang *et al.* Wang *et al.* (1993) and Weakliem *et al.* (1995) for the case of silicon are indicated in parentheses.

smaller complexes, as indicated by their respective formation energies in Table 2.3. This result is in agreement with the observations of Wang *et al.* (1993), who report that 1+2-DVs and 2-DVs are predominant on the Ge(001) surface .

We now turn to a discussion of the binding energies of DV pairs w given in Table 2.3. There are two main issues that complicate the comparison of theoretical results in Table 2.3 with the experimentally determined binding energies. First, we note that the binding energy of an isolated bound pair computed here and in Weakliem *et al.* (1995) are defined in a different manner than what is usually obtained from experiments. Experiments measure the binding energy when the DVs are part of a vacancy line, while calculations address an isolated pair of vacancies. We have estimated that the binding of two vacancies (on an average) within a VL is up to $\approx 40\%$ stronger than the binding within an isolated bound pair. Secondly, the experiments report the binding energies for DVs on Si(001) with a certain amount of Ge coverage (Chen *et al.* (1994)) or metal contamination (Chang *et al.* (1996), Zandvliet *et al.* (1995)), as

opposed to clean surfaces. Given these two concerns related to experimental conditions, as well as the use of an empirical potential in this study, discrepancies between the binding energies w listed in Table 2.3 and the ones reported experimentally are expected. However, we have found that there is reasonable agreement with the experimental data. For the single DVs on a Ge-covered Si(001) surface (1.5ML) (Chen *et al.* (1994)) estimate the binding energy in the range $-0.18\text{eV} < w < -0.25\text{eV}$, while our result for 1-DVs on pure Ge(001) is -0.24 eV and -0.28 eV on pure Si(001) (refer to Table 2.3). On the Ni-contaminated Si(001) surfaces, Zandvliet *et al.* (1995) report an average attractive interaction per unit length of -0.11 eV$/a$; since the distance between two neighboring dimer rows is $2a$, we infer that the binding energy of a pair within a VL is -0.22 eV. Chang *et al.* report a similar figure for the binding energy (-0.24 eV) of DVs on Ag-contaminated Si(001) surfaces (Chang *et al.* (1996)). On both Ni- and Ag- contaminated Si(001) the vacancy lines contain almost equal proportions of 2-DVs and 1+2-DVs (Koo *et al.* (1995), Zandvliet *et al.* (1995), Chang *et al.* (1996)) and we note that the binding energies reported in Zandvliet *et al.* (1995), Chang *et al.* (1996) lie between the calculated (Table 2.3) binding energy of a 2-DV pair (≈ -0.11 eV) and that of an 1+2-DV pair (≈ -0.32 eV) on Si(001).

The vacancy formation energy u of a vacancy complex and the binding energy w of a pair determine the formation energy of the vacancy lines to a large extent. Chen *et al.* (1994) and Weakliem *et al.* (1995) have found that interactions between single DVs that belong to different dimer rows which are not adjacent can be neglected. This approximation implies that the DVs that make up a vacancy line can be treated as a 1-dimensional system with nearest-neighbor interactions. For such a system, the formation energy per unit length can be written as:

$$\Lambda \approx \frac{u+w}{2a}, \tag{2.13}$$

where $2a$ is the distance between two DVs in a straight vacancy line. The data in Table 2.3 shows that the formation energies given by Eq. (2.13) are in good agreement with the line formation energies obtained from the $2 \times N$ surface energies (Table 2.2).

The differences between the line formation energies shown in the last two columns of Table 2.3 are due to the presence of interactions between a given vacancy with higher-order neighbors in the same VL, which are neglected in formula (2.13). While such effects could be considered small, note from Table 2.3 that they systematically lead to a lowering of the formation energy of vacancy lines below the estimate given by (2.13). As seen in the next section, the DVs are more stable as part of a vacancy line than as members of a bound pair, which is due to the presence of interactions with higher-order neighbors.

2.5.3 Experimental implications

The Si(001) and Ge(001) surfaces have been investigated intensely due to their technological and fundamental importance. As noted by Zandvliet (2003) and Zandvliet *et al.* (1998) there are still gaps in understanding the Ge(001) surface in comparison to Si(001), despite the similarity of the two surfaces. One aspect where the two surfaces show remarkable differences is that the vacancy lines appear easier to form on Si(001) rather than on Ge(001), as illustrated by the much larger number of reported observations in the case of silicon. To our knowledge, the only observation of vacancy lines on Ge(001) is for the case of Bi deposition (1ML) (Louwsma *et al.* (1997)). No vacancy lines have so far been observed on clean Ge(001) (Chey and Cahill (1997), Yang *et al.* (1994), Zandvliet *et al.* (1998), Fukuda and Ogino (1998)), while two different groups report the observation of vacancy lines on the clean Si(001) surface (Feil *et al.* (1992), Men *et al.* (1995), Smith *et al.* (1996)).

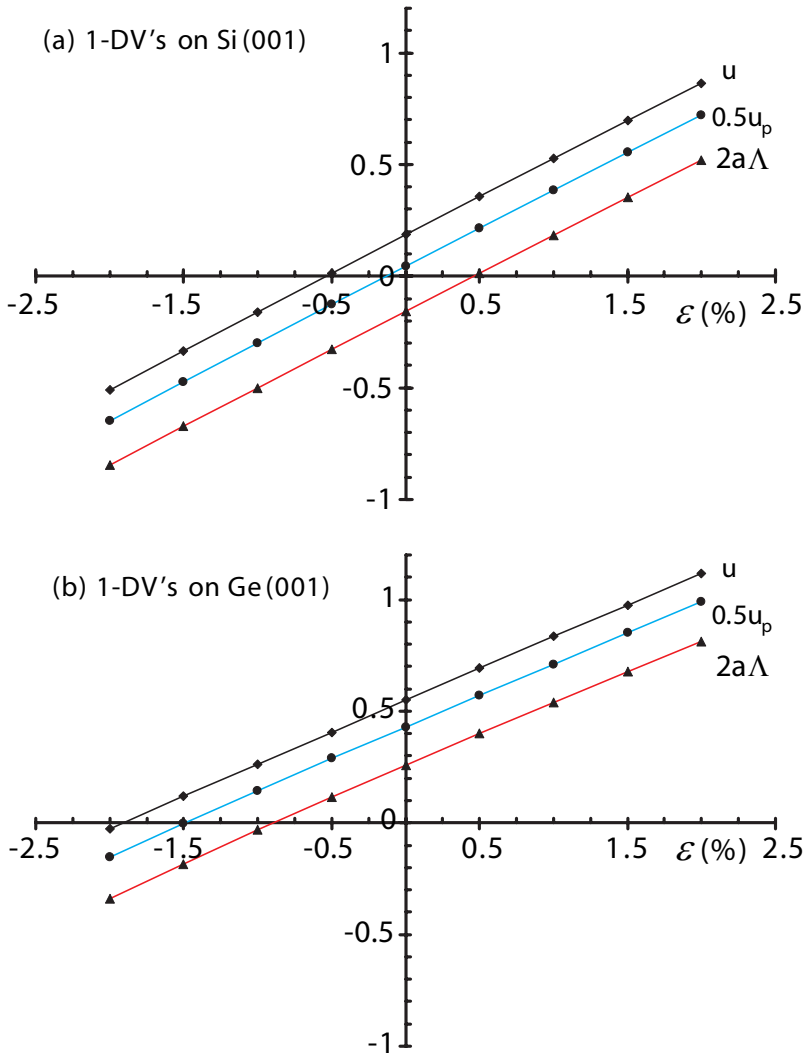

Figure 2.4: Formation energy (eV) *per 1-DV vacancy* for an isolated DV (u), a bound pair ($0.5u_p$), and a 1-DV vacancy line ($2a\Lambda$) as function of biaxial strain ε. The upper and lower figures represent the case of Si(001) and Ge(001), respectively. Note that a and Λ are the surface lattice constant and VL formation energy, both of which depend on ε. In each figure, the stability of DVs increases from the isolated DV to the vacancy lines, at given strain. Compressive strains lower the formation energy per DV both in the case of Si(001) and Ge(001), though in the case of Ge larger compressive strains must be applied in order to achieve negative formation energies.

We look for the differences between DVs on clean Si(001) and Ge(001) by comparing their formation and binding energies in the presence of strain. Focusing on single DVs, we compare the *formation energy per vacancy* for isolated vacancies, bound pairs and vacancy lines under biaxial strain. This comparison is performed separately for the case of Si and Ge surfaces. The results plotted in Fig. 2.4 which show that the formation energy per DV, to a good approximation, is a linear function of strain for strains in the range -2%–2%. In contrast, we have found that the binding energy $w = u_p - 2u$ exhibits strong nonlinear character in this strain range; the strains at which w remains linear is limited to a much smaller range, $\pm 0.2\%$. Compressive strains lower the formation energy per DV both for the case of Si and Ge, consistent with the previous results on vacancy lines (i.e. with the positive sign of the biaxial strain sensitivities shown in Table 2.2. We can now identify the difference between DVs on Si(001) and Ge(001). From Table 2.3 note that the formation energy u of a single DV is positive both for Ge(001) and Si(001), but in the case of Ge(001) it is about 3 times higher than that of an isolated DV on Si(001). Therefore, in the absence of any kinetic effects, a compressive strain of -0.5% would be required to create stable DVs ($u < 0$) on Si(001), which is readily achievable as result of quenching Men *et al.* (1995), Smith *et al.* (1996). In contrast, the critical value of compression needed to have single DVs on Ge(001) is four times larger, -1.9%. As seen in Fig. 2.4, when DVs are part of a bound pair the compression at which the formation energy per DV becomes negative decreases due to the attractive interaction between DVs: for Si(001) the critical compression becomes -0.1%, while for DVs on Ge(001) it remains rather large, -1.5%.

Based on these results (Fig. 2.4), we propose that organization of the DVs into vacancy lines on Ge(001) could be observed provided that the surface is under compressive strains of $\approx 2\%$. Biaxial strains are somewhat difficult to apply and control

accurately in practice. A simple way to provide some compression would be quenching, as done in Men *et al.* (1995), Smith *et al.* (1996). As far as lowering the formation energy of DVs is concerned, uniaxial strains along the dimer row direction are more efficient than biaxial deformations. Therefore, the use of ultraflat, single-domain surfaces under uniaxial compression along the dimer row can lead to observations of vacancies organizing into lines on Ge(001).

2.6 Conclusions

In conclusion, we have performed an investigation of the VLs and DVs on strained Si(001) and Ge(001). We have found that the dimer-vacancies on the two surfaces exhibit differences in terms of the formation energy, their strain sensitivity, and the binding energy of two DVs in adjacent dimer rows. With the present model of atomic interactions (Tersoff (1988, 1989)), each of these energetic parameters appear to favor the self-organization of DVs into vacancy lines on Si(001), but not on the Ge(001) surface.

The most important difference concerns the formation energy of single DVs, which was found to be 0.55 eV for Ge(001), but only 0.19 eV in the case of Si(001). The formation energy difference between single DVs on Si and Ge surfaces seems robust with respect to the empirical potential used: we have recalculated these energies with the Stillinger-Weber model (Stillinger and Weber (1985), Ding and Andersen (1986)), and found similar results, though the difference between the two formation energies predicted by the Stillinger-Weber potential was larger. This finding cannot be explained by scaling the DV formation energies with the bulk cohesive energy (or melting temperature) of Si and Ge. Rather, it could likely be due to subtle details in the relaxation of the atoms that surround the vacancy, particularly to the interplay between the lateral and vertical relaxation; further studies are underway in order to

elucidate this point. While it is well known that the stability of DVs on (001) surfaces is strongly enhanced by kinetic effects (i.e. two atoms are unlikely to find the DV and fill it at the same time (Zhang and Metiu (1993))), it is conceivable that the large gap between the formation energies of DVs on Si(001) and Ge(001) determines their different physical behavior.

Based on studies of how the formation energy varies with external strains, we have proposed that the self-assembly of vacancies on clean Ge(001) would be possible if compressive strains are applied either biaxially or along the dimer row direction. Pending an increase in the available computational power and methodologies, the results of this article warrant future studies using higher-level total-energy methods such as tight-binding or density functional calculations. The use of such methods is expected to bring quantitative improvements of the energetic properties computed here. Furthermore, higher-level methods can also address other important aspects of the self-assembly of vacancies such as the energetic barriers associated with the creation and diffusion of DVs on Si(001) and Ge(001). Future investigations regarding the kinetics of dimer vacancies would be invaluable for fully elucidating the differences between Si(001) and Ge(001).

Chapter 3

Interaction between the steps and the vacancy lines

3.1 Introduction

The strained-layer Ge/Si(001) system shows a remarkable variety of structural and morphological changes depending on growth conditions and Ge coverage. The system undergoes transformations from the 2×1 structure in the absence of Ge, to the $2 \times N$ reconstructed wetting layer, to the formation of hut and dome quantum dots at Ge coverages larger than about three monolayers (ML). While the formation of pyramid and dome clusters has been actively studied in the last two decades, in comparison, the initial roughening of the wetting layer (Sutter and Lagally (2000), Tromp *et al.* (2000), Sutter *et al.* (2003)) that occurs just before the formation pyramids has remained virtually unexplored. The scanning tunneling microscopy (STM) experiments of Sutter *et al.* (2003) have recently provided important insights on the initial roughening of the Ge film using microscopy techniques capable of achieving

a remarkable degree of detail and image statistics over wide areas of the film surface. Their work shows that the interactions between the S_A steps and the vacancy lines (VLs) (see Figure 3.1 for structural details) drive the roughening of the Ge film through the formation of ordered stripe patterns.

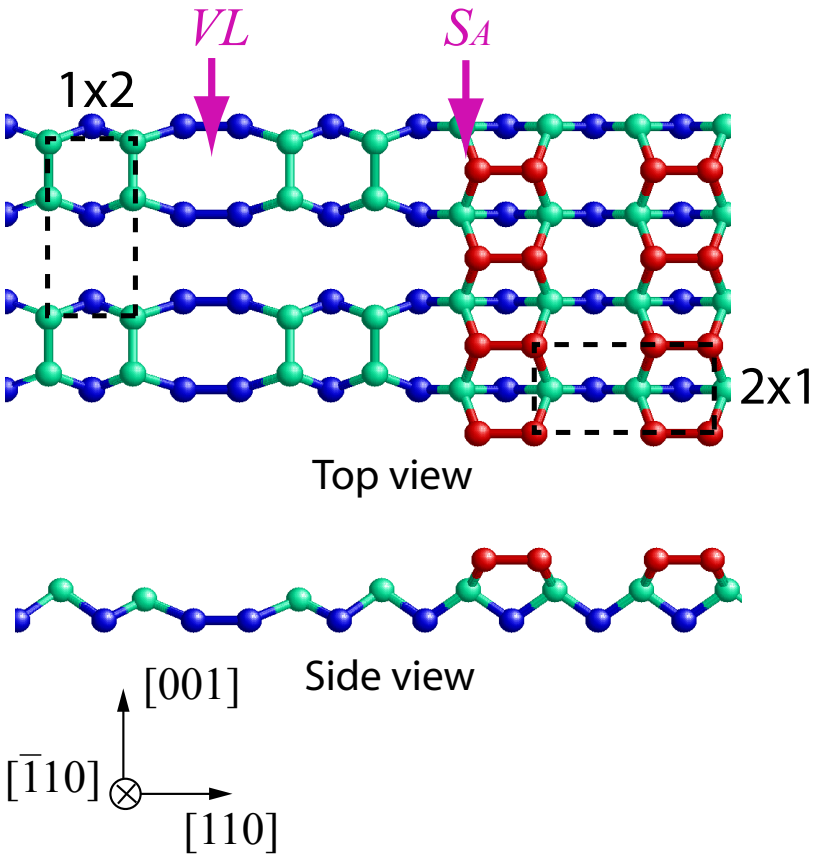

Figure 3.1: Arrangement of atoms on a surface with a S_A step and a vacancy line. Color of the atoms denote out of plane elevation in the top view. The dimer rows behind the step are parallel to it and the ones in front are perpendicular. So the 2×1 reconstruction rotates to 1×2 across the step.

Motivated by these elegant experiments of Sutter *et al.* (2003), we will investigate the energetics of the observed patterns, using both atomistic simulations and elastic theory of surface defects. The aim of our calculations is to determine the interactions between the S_A steps and VLs and to study the role of these interactions in the

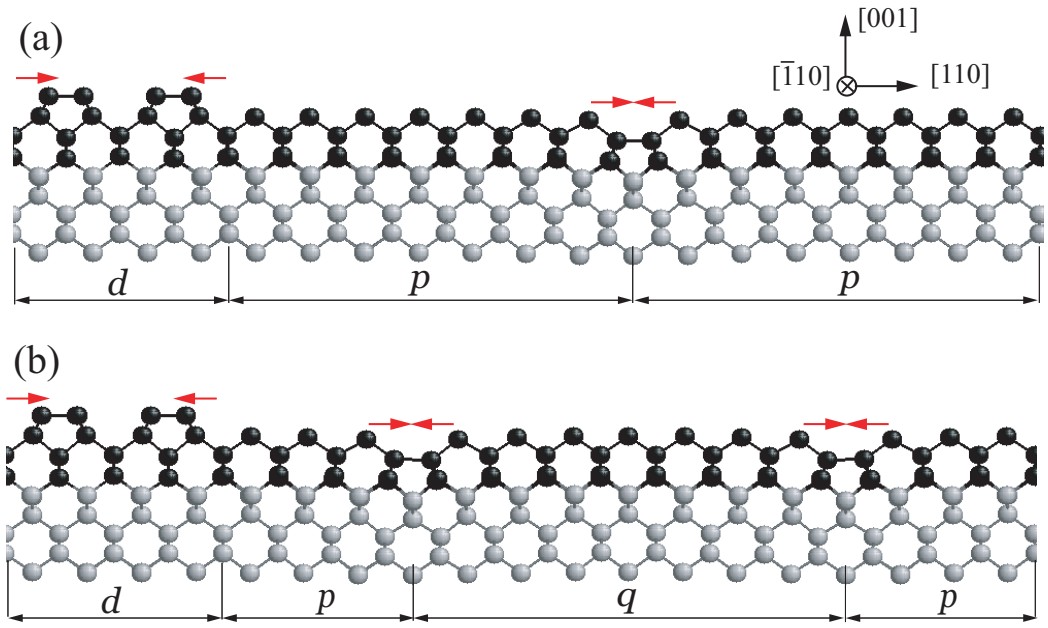

Figure 3.2: Surface unit cells for the stretch (a) and squeeze (b) configurations reported in Sutter *et al.* (2003). The Ge film is shown in black, and the Si substrate in gray. The island size is d and the distance between an S_A step and a VL is p. Configuration (b) requires another parameter q to denote the distance between the two VLs of the unit cell. The periods D along the [110] direction are $D = 2p + d$ and $D = 2p + d + q$ for models (a) and (b), respectively . The periodic length of the cells in the [$\bar{1}$10] direction is $2a$ ($a = 3.84$Å). The horizontal arrows schematically show the force monopoles and dipoles at the steps and VLs, respectively.

spatial ordering of these line defects. The simulations presented here predict that the repulsive S_A-VL interactions decay with an inverse-distance law, in agreement with the behavior expected for lines of monopoles interacting with dipoles through their elastic fields. Furthermore, we will show that these interactions modify the mean distance between the VLs, depending on the way the S_A steps and VLs are distributed on the surface.

3.2 Structural models for the initial surface roughening

The structural models that correspond to the *stretch* and the *squeeze* arrangements are illustrated in Figure 3.2. In the former case, an island of width d bounded by S_A steps is sandwiched between VLs, which leads to an increase (or stretching) in the mean spacing of the VLs. In contrast, the two VLs sandwiched between the similar islands are observed to be "squeezed" by the S_A steps in the latter case. Using the Tersoff potential for Si-Ge (Tersoff (1989)), we have performed relaxations for 90 layer thick computational cells with 2ML or 3ML Ge coverage [1] and for periods $D = Na$ ($2<N<40$), where $a = 3.84$Å is the lattice constant of the Si(001) surface. From the total energy of the slab E, we compute the surface energy $\gamma = (E - n_{Si}\mu_{Si} - n_{Ge}\mu_{Ge})/A$ as the excess energy per area $A = 2aD$, where n_{Ge}, μ_{Ge} (n_{Si}, μ_{Si}) are the number of atoms and the chemical potential of Ge (Si), respectively. The overall surface energy γ can be written as

$$\gamma = \gamma_u \frac{d}{D} + \gamma_l \frac{D-d}{D} + \frac{\lambda}{D}, \tag{3.1}$$

where the surface energy γ_u (γ_l) of the upper (lower) terrace can be obtained from separate calculations for defect-free Ge/Si(001) surfaces and λ (subsequently referred to as λ_a or λ_b for the two cases in Figure 3.2) includes the formation energies of S_A steps and VLs and their interactions.

[1] The two coverages used in the study (2ML and 3ML) lead to very similar conclusions; we therefore only report the results obtained for the 3ML case.

3.3 Energetics of periodic arrays of line defects

Before presenting the results for the interactions between S_A steps and VLs, it is useful to separately consider the energetics of periodic arrays of each of these line defects. Since the VLs can be described as elastic-force dipoles in the plane of the surface, they interact with each other with a repulsive inverse-square distance law (Ciobanu *et al.* (2004)). The energy per unit length of an array of VLs with the spacing D can then be written as

$$\lambda_{\rm VL}(D) = \Lambda^0_{\rm VL} + \Lambda^1_{\rm VL}\pi^2/(6D^2), \tag{3.2}$$

where $\Lambda^0_{\rm VL}$ is the formation energy of a VL and the second term is the interaction energy of the uniform array, where $\Lambda^1_{\rm VL}$ is the strength of the dipolar interaction. The up- and down-S_A steps on the sides of an island, on the other hand, behave like force monopoles [2] due to the discontinuity of surface stress at the island edges (Marchenko (1981), Alerhand *et al.* (1988)). Following the notations in Eq. (3.2), the energy of a periodic array of such islands of width d and period D is given by (Alerhand *et al.* (1988), Poon *et al.* (1992))

$$\lambda_{S_A}(d, D) = 2\Lambda^0_{S_A} - \Lambda^1_{S_A} \log\left(\frac{D}{\pi c}\sin\left(\frac{\pi d}{D}\right)\right), \tag{3.3}$$

where $c = a/2$ is an atomic scale cut-off introduced to regularize the logarithmic divergence [3]. The parameters Λ^0 and Λ^1 in Eqs. (3.2), (3.3) obtained from atomistic simulations as described in Ciobanu *et al.* (2004), and Poon *et al.* (1992) are given in Table 3.1.

[2] In general, surface steps also have dipole moments. For the S_A steps, the dipole strength is negligible due to the absence of rebonding at the step-edge (Poon *et al.* (1992)).

[3] The cut-off radius c is of the order of a, but otherwise arbitrary. Eq. (3.3) shows that the choice of c affects the formation energy $\Lambda^0_{S_A}$ but does not change the interaction coefficient $\Lambda^1_{S_A}$.

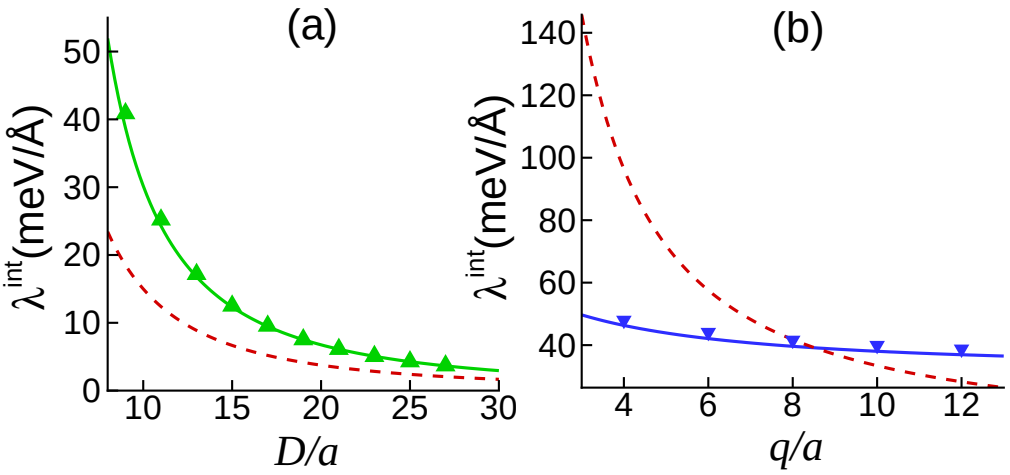

Figure 3.3: Interaction energy of S_A steps and VLs obtained from atomistic simulations in the stretch configuration ((a), triangles up) and in the squeeze pattern ((b), triangles down), along with the fitting curves given by Eq. (3.5) and Eq. (3.8), respectively. The dashed curves show the interaction energy between VLs (refer to Eqs. (3.2) and (3.7)) in the two configurations. The island size is $d = 4a$ in both cases, and the S_A-VL distance in case (b) is $p = 2.5a$.

defects	Λ^0 (meV/Å)	Λ^1
VL	-133.934 ± 0.201	13434±89 meVÅ
S_A	-1.56 ± 0.11	4.556±0.076 meV/Å
S_A-VL		254.677±1.077 meV

Table 3.1: Defect formation energies Λ^0 and interaction strength parameters Λ^1 computed using the Tersoff interatomic potential (Tersoff (1989)).

3.4 Interaction energy of the "stretch" and the "squeeze" configurations

We now consider the stretch configuration (Figure 3.2(a)), for which the defect energy can be written as

$$\lambda_a(d, D) = \lambda_{\text{VL}} + \lambda_{S_A} + \lambda^{\text{int}}_{a,S_A\text{-VL}}, \tag{3.4}$$

where λ_{VL} and λ_{S_A} are given by Eqs. (3.2) and (3.3), respectively, and the third term denotes the interaction between the monopoles at the S_A steps and the dipoles at the VLs. We have calculated this term from atomistic relaxations of the stretch structure (Figure 3.2(a)) and plotted it in Figure 3.3(a) as a function of the VL spacing D, for fixed island width $d = 4a$. In order to extract the strength of the S_A-VL interaction from this data, we note that according to elasticity theory, a single S_A step interacts with a single VL with a power law that decays as the inverse of the distance between them. Using $\Lambda^1_{S_A\text{-VL}}$ to denote the strength of this monopole-dipole interaction, the contributions corresponding to the steps and VLs in the unit cell of the stretch configuration and its periodic images can be summed analytically to

$$\lambda^{\text{int}}_{a,S_A\text{-VL}} = \Lambda^1_{S_A\text{-VL}} \frac{2\pi}{D} \tan\left(\frac{\pi d}{2D}\right). \tag{3.5}$$

It can be seen from Figure 3.3(a) that this functional form provides an excellent fit to the results of the simulations. Furthermore, the coefficient $\Lambda^1_{S_A\text{-VL}}$=254.7 meV obtained from the fitting procedure is very close to the geometric average $\sqrt{\Lambda^1_{\text{VL}}\Lambda^1_{S_A}}$=247.4 meV that is expected [4] for the interaction of a monopole with a dipole. These observations confirm that the S_A-VL interaction is accurately modeled using the elastic theory of surface defects.

In the case of squeeze configurations (Figure 3.2(b)), the defect energy can be written as

$$\lambda_b(d,q,D) = 2\Lambda^0_{\text{VL}} + \lambda_{S_A} + \lambda^{\text{int}}_{b,\text{VL}} + \lambda^{\text{int}}_{b,S_A\text{-VL}}, \tag{3.6}$$

where λ_{S_A} is given by Eq. (3.3) and the second and third term correspond to the VL-VL and S_A-VL interactions, respectively. Since there are two (one) VLs in the unit cell of the squeeze (stretch) configuration, these terms are different for the two cases. We have computed the last two terms in Eq. (3.6) analytically by summing the series of dipole-dipole and monopole-dipole contributions :

$$\lambda^{\text{int}}_{b,\text{VL}} = \Lambda^1_{\text{VL}}\frac{\pi^2}{3D^2}\left[1 + 3\csc^2\left(\frac{\pi q}{D}\right)\right] \tag{3.7}$$

$$\lambda^{\text{int}}_{b,S_A\text{-VL}} = \Lambda^1_{S_A\text{-VL}}\frac{2\pi}{D}\left[\cot\left(\frac{\pi p}{D}\right) - \cot\left(\frac{\pi(p+d)}{D}\right)\right] \tag{3.8}$$

Since the strengths of all defect interactions have already been determined, each term in Eq. (3.6) can be evaluated without the need for atomistic relaxations of the squeeze structures. We have, however, performed these calculations to further confirm that the parameters in Table. I accurately describe the S_A-VL interactions, as shown in Figure 3.3(b).

[4] Denoting the monopole (dipole) strength by A_x (A_{xx}), the interaction coefficients Λ^1 can be written as $\Lambda^1_{\text{VL}} = \alpha A^2_{xx}$, $\Lambda^1_{S_A} = \alpha A^2_x$, $\Lambda^1_{S_A\text{-VL}} = \alpha A_x A_{xx}$, where α is related to the elastic moduli of the substrate (Marchenko (1981)). It then follows that $\Lambda^1_{S_A\text{-VL}} = \sqrt{\Lambda^1_{S_A}\Lambda^1_{\text{VL}}}$.

3.5 Self-assembly of the steps and the vacancy lines

With the information on the defect formation and interaction energies, we can now discuss their spatial ordering in the wetting layer. In the absence of S_A-bounded islands, the spacing between VLs is determined by minimizing the defect energy per period of the defect array, which is $\lambda_{\rm VL}/D$ (refer to Eq. (3.2)). As shown by Ciobanu *et al.* (2004), a competition between the negative formation energy of VLs and their repulsive interactions leads to a mean spacing $D = 6a$, which compares favorably with the experimental value of $(8 \pm 0.9)a$ (Sutter *et al.* (2003)). To see how this spacing is altered in the two structures in Figure 3.2, we have plotted $\lambda_{a,b}/D$ (from Eq. (3.4) and Eq. (3.6)) as functions of the spacing between the VLs in Figure 3.4, choosing a typical island width of $d = 4a$. While the island width d and the VL-VL separation D determine the S_A-VL spacing $((D-d)/2)$ in the stretch configuration, this spacing (p) is an independent parameter for the squeeze structures. We have found, however, that the defect energy per period λ_b/D is minimum at the S_A-VL separation of $p = 2.5a$ for island widths in the range $2a \leq d \leq 8a$. This result is in agreement with the observations of Sutter *et al.* (2003), who find that S_A-VL spacings of $1.5a$ and $2.5a$ occur much more frequently than any other S_A-VL separation. In what follows, we discuss the variation of the defect energy λ/D as a function of VL-VL distance.

A comparative analysis of the VL-VL spacing between stretch, free and squeeze configurations reveals a remarkable consistency with experimental findings. As seen in Figure 3.4, the optimum VL-VL distance in the stretch case is $D = 10a$, which is larger than the spacing of free VLs (Ciobanu *et al.* (2004)) by four Si(001) lattice constants. A similar increase in the VL spacing has been observed by Sutter *et al.* (2003), who report separations of $(8.0 \pm 0.9)a$ and $(11.9 \pm 1.7)a$ for the free and stretch

configurations, respectively. For squeeze structures with $d = 4a$ and $p = 2.5a$, we find nearly the same optimum VL-VL distance ($q \simeq 6a$) as in the case of free VLs. This finding is also consistent with the STM observations (Sutter *et al.* (2003)), which show only small change in the VL-VL distance from $(8.0 \pm 0.9)a$ (free) to $(7.1 \pm 0.9)a$ (squeeze). The close agreement of the computational and analytical results with experiments suggests that the empirical potential (Tersoff (1989)) used in our work is able to capture the key features of the interactions of line defects on Ge/Si(001).

The pronounced difference between the statistics of VL separations in the stretch and squeeze configurations (Sutter *et al.* (2003)) can be understood by considering the relative contributions of the monopole-dipole and dipole-dipole interactions to the surface energy of each configuration. In the stretch case, the S_A-VL (monopole-dipole) interactions are stronger than the VL-VL interactions, as seen in Figure 3.3(a). Therefore, the optimum spacing of $6a$ determined for a uniform array of VLs (Ciobanu *et al.* (2004)) will be increased significantly by the presence of islands between the VLs (Figure 3.2(a)). In the squeeze case (Figure 3.3(b)), since the islands are located between *pairs* of VLs, the VL-VL repulsion dominates the SA-VL interaction. Indeed, the monopole-dipole terms are found to have little influence on the VL-VL distance in the squeeze configuration.

3.6 Conclusions

In conclusion, we have studied the energetics of self-organized patterns of S_A-VL patterns observed on the wetting layer during early stages of growth (Sutter *et al.* (2003)) using a linear elasticity based approach combined with atomistic simulations. Analytical expressions derived from representation of step as a monopole and VL as a dipole provides excellent fit to the atomic simulation. Our study demonstrates the existence of an effective repulsion between steps and VLs, which has been identified

as a key factor in the initial roughening of the Ge/Si(001) system. Our analysis also predicts optimal separations for the VLs in agreement with recent microscopy experiments Sutter *et al.* (2003).

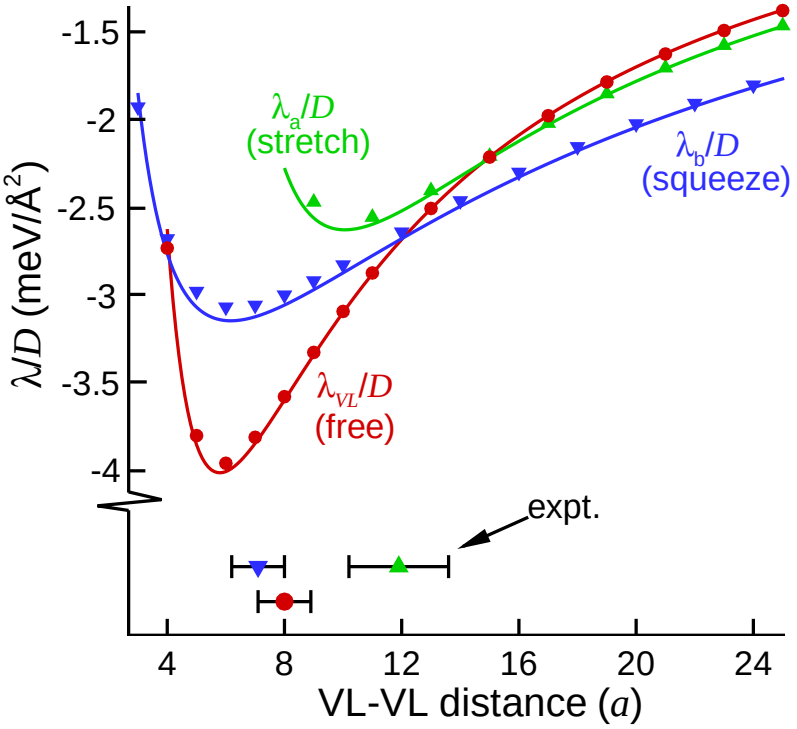

Figure 3.4: Surface energy contributions λ_a/D (at $d = 4a$) and λ_b/D (at $d = 4a$, $p = 2.5a$) corresponding to the arrays of line defects shown in Figure 3.2(a) and (b), respectively. The case of free VLs (i.e., without steps) is also plotted for comparison. In the stretch and free configurations, the VL-VL distance is simply the period along [110], D. For the squeeze case, the VL-VL separation is q, as shown in Figure 3.2(b). The curves correspond to the analytical expressions given in Eqs. (3.2), (3.4), and (3.6), while the data points are calculated from atomistic simulations. The optimum VL separations determined from STM experiments (expt.) Sutter *et al.* (2003) are shown along with error estimates.

Chapter 4

Energetic origin of trench depth

4.1 Introduction

In the heteroepitaxial system, it is well known that mismatch strain at low Ge coverages is relaxed by the formation of pyramid-shaped islands with {105} facets. As these islands grow in size, they transform into what are called domes with steeper sidewall angles. Even larger islands show strain relaxation through the injection of misfit dislocations. In high temperature growth (T $> 600^0$C), strain relaxation is also achieved by trenches that form around the bases of both coherent and dislocated islands (Chaparro, Zhang and Drucker (2000), Chaparro, Zhang, Drucker, Chandrashekhar and Smith (2000), Drucker *et al.* (2000), Drucker (2002), Denker *et al.* (2001, 2002), Kamins *et al.* (1997), Floro *et al.* (1997)). Denker *et al.* (2005) observed that the trenches serve as a source of Si which mixes with Ge that is being captured by the island which reduces its mismatch strain. Even during capping with Si, the trenches form around the new expanded base area of the island (eg. Katsaros *et al.* (2007)). Experimental work of Chaparro, Zhang and Drucker (2000) has shown that the trenches at the base of dome-shaped islands are self-limiting, in the sense that their depths saturate at a level, linearly proportional to the base-width of the island.

While it has been suggested that this behavior is due to kinetic limitations (eg. Chaparro, Zhang and Drucker (2000)), quantitative estimates for the self-limiting depth and a reason for its linear dependence of the island size have not been provided. In this chapter, we will consider the energetics and strain relaxation of islands surrounded by trenches using finite element simulations and show that the self-limiting nature of trenches can be explained on the basis of a competition between the elastic energy gained by the formation of the trenches and the surface energy cost involved in creating the trenches. These calculations employ trenches whose dimensions and shapes are comparable to the ones observed in experiments, predict a linear dependence of the trench depth on the island base-width, in good quantitative agreement with experimental data.

4.2 Strain relaxation due to formation of trenches

We will first consider strain relaxation due to trench formation around a cone shaped island shown in Fig. 4.1(a). The cone radius and angle are denoted by R and θ, respectively, while a trench of depth h is modeled using two inclined surfaces at angles β and α shown in Fig. 4.1(a). In the case of trenches observed in experiments (Chaparro, Zhang and Drucker (2000), Chaparro, Zhang, Drucker, Chandrashekhar and Smith (2000), Denker *et al.* (2001)), β is comparable to or bigger than the island sidewall angle θ, while the angle α is much smaller, usually a few degrees. A displacement based finite element method with linear shape functions is used to obtain the elastic fields in the island and the substrate. Strain in the structure can be expressed as

$$\varepsilon_{ij} = \varepsilon^0_{ij} + u_{ij}$$

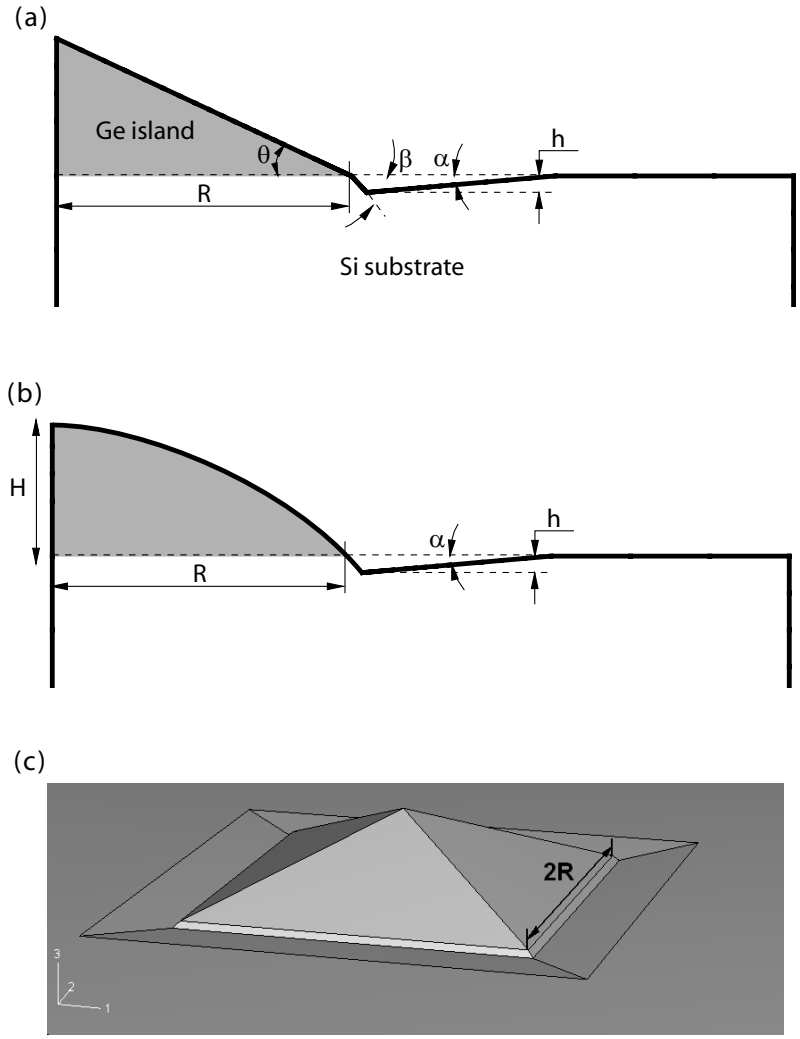

Figure 4.1: Schematic of the axisymmetric model of a (a) cone-shaped, and (b) dome-shaped, and a 3D (c) pyramidal Ge island. The islands have a half base size R and cone angle θ. The depth of trench around the base of the island is denoted by h and the trench angles β and α are shown in the figure.

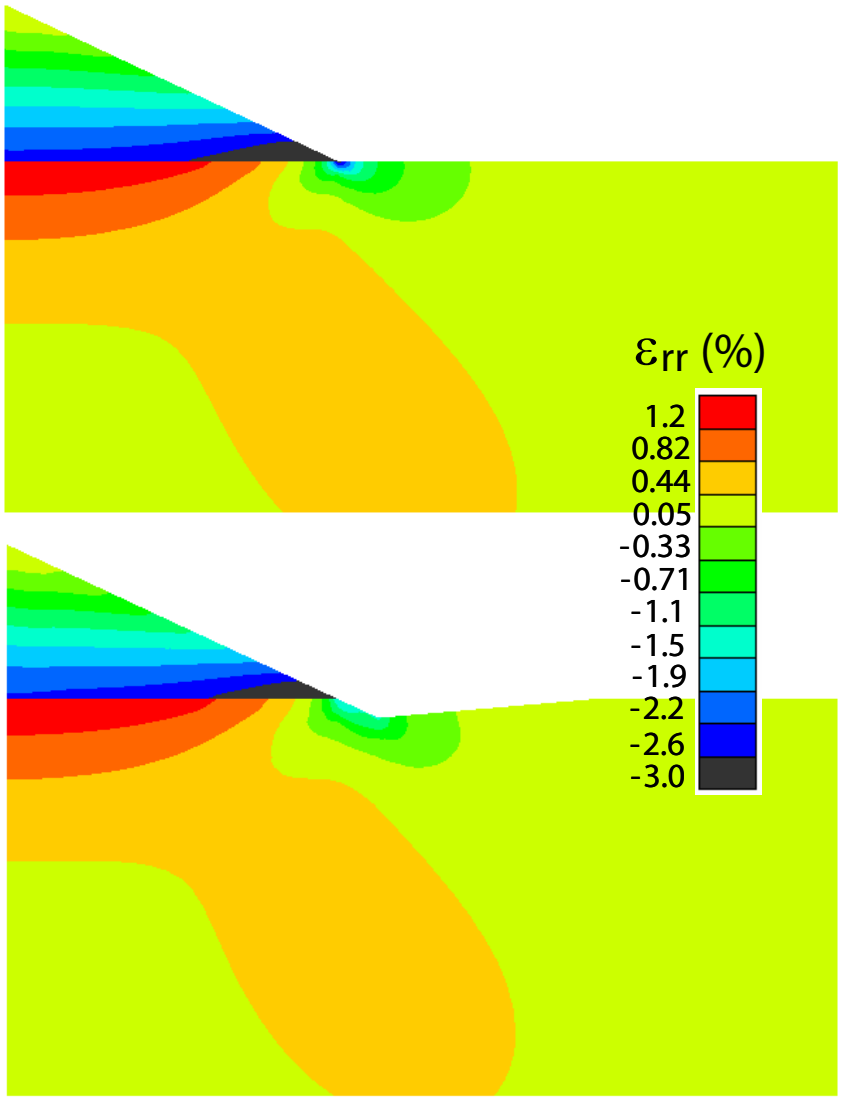

Figure 4.2: Contour plots of distribution of radial strain ε_{rr} for a cone-shaped island with (bottom) and without trench (top). Here h = 10nm, R = 125, θ=β =25^0 and α=5^0.

where, ε_{ij}^{0} is the mismatch strain (present only in the island) and u_{ij} is the *additional* strain due to elastic relaxation. The non-zero components of the relaxation stress tensor (in cylindrical coordinates) are given by

$$\begin{pmatrix} \sigma_{rr} \\ \sigma_{\theta\theta} \\ \sigma_{zz} \\ \sigma_{rz} \end{pmatrix} = \begin{pmatrix} C_{11} & C_{12} & C_{12} & 0 \\ C_{12} & C_{11} & C_{12} & 0 \\ C_{12} & C_{12} & C_{11} & 0 \\ 0 & 0 & 0 & (C_{11}-C_{12})/2 \end{pmatrix} \begin{pmatrix} u_{rr} \\ u_{\theta\theta} \\ u_{zz} \\ u_{rz} \end{pmatrix},$$

where the elastic constants of the Si substrate and the Ge island are taken to be C_{11} = 165.7 GPa, C_{12} = 63.9 GPa and C_{11} = 128.5 GPa, C_{12} = 48.3 GPa, respectively. If the strain fields are obtained from finite element calculations, the free energy of the system, which is the sum of the energy gained through elastic relaxation and the increase in surface energy due to formation of the trench, can be written as

$$E_f = E_r + E_s = -\frac{1}{2}\int_{V_S} \sigma_{ij} u_{ij} dV + \gamma \Delta A. \tag{4.1}$$

Here, the first integral is evaluated over the volume V_S of the system, which includes the island and the substrate with the trench, ΔA denotes the increase in surface area due to formation of the trench and γ is the surface energy of the substrate, assumed to be independent of strain and orientation [1].

The radial strain (ε_{rr}) distribution in the island with and without the trench for $\beta = \theta = 25^0$, $\alpha = 5^0$ and an equibiaxial mismatch strain of -4% is shown in Fig. 4.2. In both the cases, the radial strain ε_{rr} changes sign across the island substrate interface with the substrate side under tension. The apex of the island is

[1] Since data on the strain and orientation dependence of surface energies is not available from experiments or accurate quantum mechanical calculations, we use $\gamma = 1.5$ J/m^2, which is typical for semiconductor surfaces.

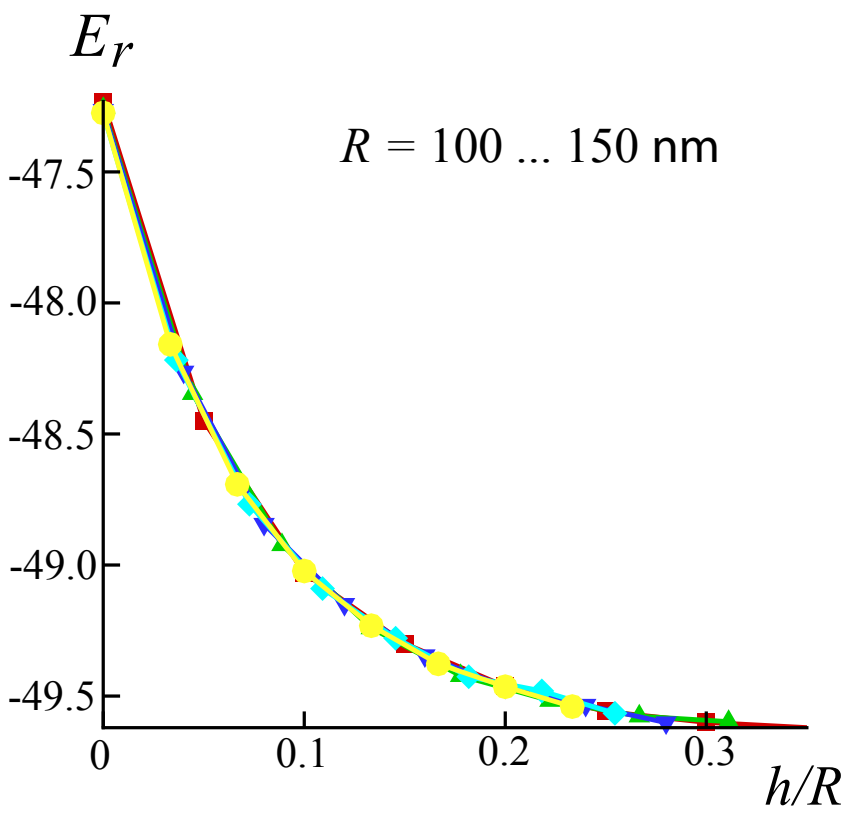

Figure 4.3: Elastic relaxation energy of an island with a trench normalized by the total strain energy of the island prior to relaxation $M\epsilon_0^2 V$, plotted versus the ratio of trench depth h to island radius R. Note that the relaxation energy attains saturation at $h/R \sim 0.3$. The surface orientations (refer to Fig. 4.1) in this calculations are α=5^0 and β=θ=25^0.

slightly over-relaxed [2]. The key difference between the case with the trench compared to the case without the trench relates to the strain distribution around the base of the island. The presence of trench leads to an effective relaxation of the large near-surface compressive strain at point where the island makes contact with the substrate. At the same time, the trench also allows relaxation of tensile strain ε_{zz} near the base of the island.

[2] A similar tensile strain at the top of islands has also been observed in calculations reported by Johnson and Freund (1997), Spencer and Tersoff (2001)

The elastic relaxation energy as a function of trench depth h is given in Fig. 4.3 for islands of different radii, but fixed surface orientations θ, β and α. Here, we have plotted the first term in Eq. (4.1) normalized by the total strain energy of the island prior to relaxation, $M\epsilon_0^2 V$, where M is the biaxial modulus [3], $\epsilon_0 = -4\%$ is the mismatch strain and $V = (\pi R^3 \tan\theta)/3$ is the volume of the island. As the trench depth is increased, the elastic energy initially decreases at a rapid rate, but eventually saturates at $h/R \sim 0.3$. Since the strain fields decay rapidly from the island substrate interface, the energy gained by extending the trenches to relatively unstrained regions is small, leading to the observed saturation in strain relaxation. We also find that normalized energies for islands of different radii fall on a single curve if the trench depth is scaled with the radius of the island, which shows that deeper trenches are required to achieve saturation of elastic energy for bigger islands. While elastic energy is relaxed by increasing trench depth, deeper trenches also lead to an increase in the total surface energy of the system.

4.3 Optimum trench depth

Figure 4.4 shows that the net change in surface energy is comparable to the energy gained via strain relaxation for an island with $R = 125$ nm. Furthermore, a competition between these two effects leads to a self-limiting trench size, h_0, which corresponds to the minimum in the free energy E_f (refer to Eq. 2) as shown in the inset in Fig. 4.4. We point out that while the gain in elastic energy by formation of trenches is only 2% of the total strain energy of the structure without trench, this corresponds to 3.55×10^5 k_BT at 600^0C for the island in Fig. 4.4; the trenches should then be very stable against thermal fluctuations. The net gain in free energy and the

[3] The biaxial modulus can be written in terms of the elastic constants as $M = C_{11} + C_{12} - 2C_{12}^2/C_{11}$.

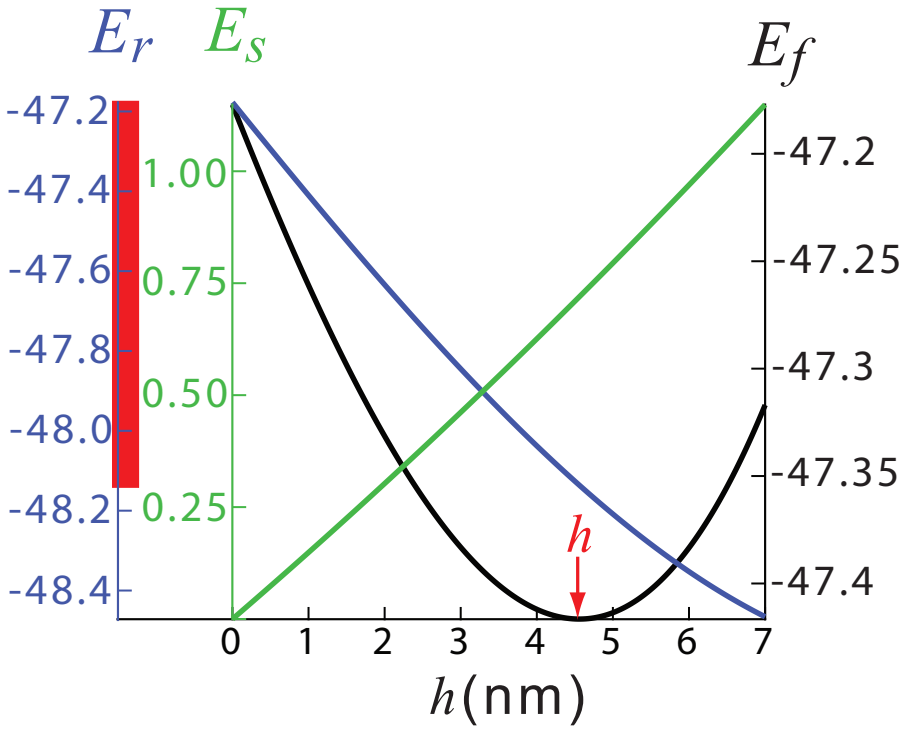

Figure 4.4: Competition between the elastic relaxation energy (blue) and the change in surface energy (green, normalized by 100 $M\epsilon_0^2 V$) resulting in a minimum in the total free energy (black) at an optimum trench depth (h_0) for an island with $R = 125$ nm and γ=1.5 J/m^2. Gain in elastic energy of magnitude 3.55×10^5 k_BT at 600°C due to formation of trenches is shown with a red band.

β	ΔE_f	h_0	α	ΔE_f	h_0	θ=β	ΔE_f	h_0
25°	2.21	4.56	5°	2.21	4.56	15°	-	-
33°	2.48	4.92	10°	0.62	3.0	20°	0.23	2.50
47°	2.83	5.51	15°	0.19	1.42	25°	2.21	4.56

Table 4.1: Effect of variations in the surface orientations β, α and θ for a cone-shaped island on the optimum trench depth (h_0 in nm) and the normalized relaxation energy ($\Delta E_f \times 10^{-3}$, where $\Delta E_f = E_f(h = 0) - E_f(h = h_0)$) with respect to the ungrooved structure. When the variations of a particular parameter is considered, the default values of other parameters are, $\theta = \beta$=25°, α=5° and γ=1.5 J/m^2.

self-limiting trench depth depends on the surface orientations of the island and the trench and the size of the island. We consider these effects in the following paragraph.

The data in the first column of Table 1 shows that the optimum trench depth h_0 increases by about 1nm when the trench angle β is increased from 25^0 to 47^0 at fixed θ and α for $R = 125$nm. We can understand this trend by noting that larger β leads to more effective relaxation of the compressive strain at the point where the island meets the substrate and the tensile strain in the substrate. While the free energy of the system can be lowered for larger β, the opposite is true for the trench angle α (refer to the second column of Table 1). Lower values of α allow better relaxation of the tensile strain in the substrate and involve a smaller change in surface energy. This result is in agreement with experimental observations (Chaparro, Zhang and Drucker (2000), Drucker *et al.* (2000), Chaparro, Zhang, Drucker, Chandrashekhar and Smith (2000), Denker *et al.* (2001, 2002)) that show steep (large β) and shallow (small α) surface orientations of the trench close to and away from the island, respectively; the two-angle model in Fig. 4.1 therefore provides a good geometric description of the observed trenches[4]. If the sidewall angle of the island is lowered by choosing $\beta = \theta$ and by holding α constant, optimum trench depth h_0 decreases in a monotonous

[4]We have also studied other trench geometries, in particular, wedge-shaped trenches considered in Chaparro, Zhang and Drucker (2000) and trenches shaped like circular arcs. Saturation of trench depths was observed in both of these geometric models.

manner (refer to the third column in Table 1) until it becomes unfavorable to form trenches for $\theta \leq 15^0$. This result would indicate that the trenches would not be observed at around the hut-shaped {105}-faceted islands whose base-widths are $\leq$ 200 nm, in agreement with experimental observations Chaparro, Zhang, Drucker, Chandrashekhar and Smith (2000). Next, we consider the evolution of the trench depth with the radius of the island, with the aim of comparing the predictions of our calculations with the data reported in Chaparro, Zhang and Drucker (2000).

Since the AFM and TEM images of the cross-sections of the domes (Chaparro, Zhang and Drucker (2000), Chaparro, Zhang, Drucker, Chandrashekhar and Smith (2000), Drucker *et al.* (2000)) indicate that the steeper face of the trench is at the same orientation as the sidewall of the dome cluster, we take $\beta = \theta = 25^0$, which is very close to the angles made by the {113} and {102} facets with the substrate. The dependence of the optimum trench depth as a function of the island radius is given in Fig. 4.5 for the axisymmetric cone (Fig. 4.1) and for a dome-shaped island whose sidewall is an arc of a circle with aspect-ratio (ratio of height H to radius R as shown in Fig. 4.5) of 0.3. The figure also shows the optimum trench depth for a pyramid-shaped island[5] (with a square base as shown in Fig. 4.5) as a function of its half-base width, R. In all the cases, we find a nearly linear increase of the optimum trench depth with the island base width, which is in good quantitative agreement with experimental data from Chaparro, Zhang and Drucker (2000). Our results therefore clearly indicate that the saturation of the trench depths is consistent with the energetics of trench formation. It should also be noted that the self-limiting trench depths observed in Chaparro, Zhang and Drucker (2000) do not change as the temperature is raised from 600°C to 650°C, which provides further evidence for the energetic origin of the observed behavior. Measurements of trench depths at

[5]The calculations for the pyramid-shaped islands were carried out using the finite element program ABAQUS.

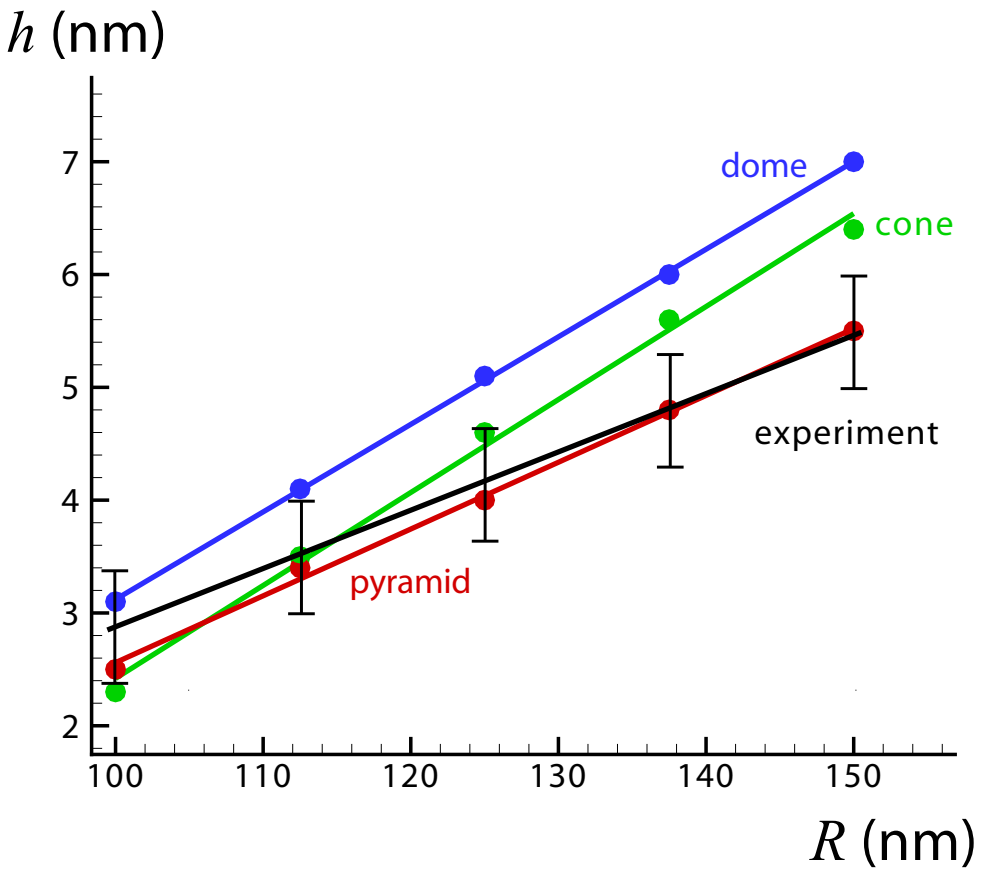

Figure 4.5: Self-limiting trench depth plotted as a function of the island radius for the axisymmetric cone (Fig. 4.1) and dome-shaped (inset (b)) islands and versus the half-base width of a pyramid-shaped island shown in inset (a). All the islands are surrounded by the two-angle trench shown in Fig. 4.1 with β=25^0, α=5^0. The side-wall angle of the cone and the pyramid-shaped islands are taken to be θ=25^0, while H/R =0.3 for the dome-shaped island. The surface energy is γ =1.5 J/m^2 in all the cases. Saturation depth observed in the experiments (Chaparro, Zhang and Drucker (2000)) is shown by the filled circles.

even higher temperatures can perhaps provide further insights into the mechanisms responsible for the saturation of trench depths.

4.4 Conclusions

In conclusion, we have shown that the self-limiting behavior of the trenches around the bases of SiGe quantum dots can be explained on the basis of a competition between elastic relaxation and the surface energy cost of creating the trench surface. The gain in elastic energy by formation of trenches is orders of magnitude greater than the thermal energy (k_BT) and ensures stability of trenches against thermal fluctuations. The optimum trench depth obtained from our analysis has an approximate linear dependence with the island radius, due to the fact that more elastic energy can be relaxed by trench formation in the case of larger islands.

Chapter 5

Emergence of (103) and (104) facets on pyramidal islands

5.1 Introduction

During deposition of Ge on Si(001) substrate, the mismatch strain is relieved by forming pyramidal islands. With further deposition, the island undergoes morphological transformation and acquires multifaceted dome shape. Each stable intermediate shape of the quantum dot has a unique opto-electronic application. Recently, some experimental studies have shown that the pyramidal islands with facets steeper than, widely observed, (105) are also stable. During growth experiments Le Thanh *et al.* (2000), Yam *et al.* (2001) observe stable (103) and (104) faceted pyramids, similar shape is observed by Wu *et al.* (2005, 2007) during Si overgrowth experiments. Goal of this chapter is to find physical reasons for stability of pyramidal islands with facets steeper than (105).

Observed morphology of a epitaxially grown heterostructure is either a thermodynamically preferred configuration or a kinetically limited state. In this chapter,

we determine thermodynamic stability of the pyramidal islands where the minimum energy configuration is a compromise between increase in free energy by creation of new surfaces and decrease due to relaxation of mismatch strain. Main results of this chapter are:

- The pyramidal islands with (103) and (104) facets emerge due to their ability to relax the mismatch strain better.
- Atomic reconstruction for Ge (104) surface which, at the level of empirical potential (Tersoff (1989)), has free energy close to the SR reconstructed (105) surface in a biaxially compressed state.
- An equilibrium phase diagram for (103), (104), and (105) faceted pyramidal islands where unique equilibrium facet orientation can be obtained as a function of composition and volume of the island.

5.2 Review of experimental observations

When the dome shaped SiGe islands are capped with Si at 640°C, the Ge content of the island is diluted due to intermixing of the capping material with the island. As a result, the islands undergo remarkable changes in morphology and electronic properties[1] Kummer *et al.* (2000), Rastelli *et al.* (2001), Capellini *et al.* (2005), Wu *et al.* (2005), Li *et al.* (2006), Lang *et al.* (2006). Morphologically, the islands transform from a multifaceted dome shape to a (105) pyramid with intermediate phases where the pyramidal islands are bound by (103) and (104) facets. However, when a film containing pyramidal islands with steeper facets are annealed at room temperature for a period of twelve months, the (103) facets flatten to (104) Wu *et al.* (2007).

[1]Ge content of the island decreases which shrinks the island and also lowers the confinement potential for holes. In-plane tensile strain in the Si region below the island also reduces which lowers the confinement potential for electrons.

(103) and (104) facets are rarely observed during growth process Yam *et al.* (2001), Le Thanh *et al.* (2000). Major difference between the growth and Si overgrowth process is the availability of Si which reduces mismatch strain of the island. During growth process, silicon is recruited from the substrate which creates trenches around the island Chaparro, Zhang and Drucker (2000), whereas during Si overgrowth process, the capping material serves as an additional source of Si. Hence the capped islands undergo a unique morphological transformation Rastelli *et al.* (2001). From the accessibility of the physical details of island morphology in capping experiments of Wu et al., it is likely that capping stabilizes steeper facets on the pyramidal islands. However, the morphological transformation during Si overgrowth can be kinetically suppressed by depositing at least a few capping monolayers at low temperature Rastelli *et al.* (2002), Wu *et al.* (2005), Lin *et al.* (2007), Li *et al.* (2007).

From thermodynamics perspective, a shape is stable if any change leads to an increase in total free energy E_f by an amount much greater than the thermal energy k_BT. In the next section we will evaluate the total free energy of an epitaxially grown SiGe pyramidal island on Si substrate and obtain parameters for which (103) and (104) pyramidal islands are equilibrium morphologies.

5.3 Total free energy of a pyramidal heterostructure

The equilibrium shape of the island minimizes the total free energy E_f per unit volume V of the island. For an island substrate system, assuming uniform composition for the island [2] and neglecting the corner and edge energies, the total free energy is

[2] Denker *et al.* (2003) do not find any reduction of strain energy between the constant composition and experimentally observed silicon enrichment of the corners.

given by

$$E_f(h,b,\alpha) = E_r(h,b,\alpha) - M(\alpha)\epsilon(\alpha)^2 V(h,b) + \gamma(h/b,\alpha)A_p(h,b) + \gamma((001),\alpha)A_s(h,b). \tag{5.1}$$

The strain energy E_r and the surface energy density γ are both function of average mismatch strain α and facet orientation $\theta = \arctan(2h/b)$ of the island. Second term

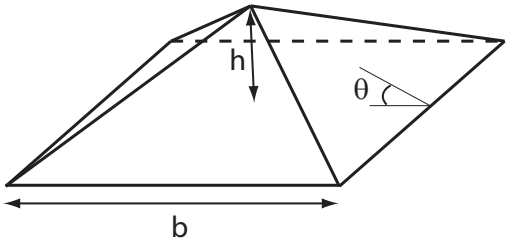

$$A_p(h,b) = 2b\sqrt{\frac{b^2}{4} + h^2}$$

$$A_s(h,b) = (10h)^2 - b^2$$

$$V(h,b) = \frac{b^2 h}{3}$$

Figure 5.1: Schematic of a pyramidal island of height h and base width b. Expressions for surface area of the pyramid A_p and the substrate exposed by steeper facets of same volume A_s are given along with the volume V of the pyramid.

in the Equation 5.1 is the strain energy in the island prior to relaxation. In this term the biaxial modulus $M(\alpha)$ [3] is calculated using weighted average of elastic properties Si and Ge [4]. The strain energy is calculated using finite element method [5] where the mismatch strain is represented in the form of higher thermal expansion coefficient for the island compared to the substrate. Surface energy, on the other hand, is evaluated using atomic simulations which require knowledge of positions of surface and near-surface atoms. Since we are interested in (103), (104), and (105) surfaces and only (103) (Ciobanu *et al.* (2007)) and (105) (Khor and Das Sarma (1997)) surface reconstructions are known, the first task of this calculation is to obtain reconstruction of (104) surface. In the next section we obtain the best possible arrangement of

[3] $M = C_{1111} + C_{1122} - 2C_{1122}^2/C_{1111}$

[4] $C_{ijkl}(\alpha) = \alpha C_{ijkl}(Ge) + (1-\alpha)C_{ijkl}(Si)$

[5] This 3D boundary value problem is solved with the help of a commercially available finite element software ABAQUS.

atoms on a bulk truncated (104) surface using a stochastic optimization technique and evaluate the influence of biaxial compression on its free energy.

5.3.1 Atomic reconstruction and energy of (104) surface

Energy of the surface is determined structure of the bonds formed between the surface atoms (eg. Fujikawa *et al.* (2002), Raiteri *et al.* (2002), Shenoy *et al.* (2002)). Physical significance of the bond structure has been shown by Shenoy *et al.* (2002) in the context of (105) facet; it is shown that the stretched bonds formed between two distant surface atoms impart stability to the surface under biaxial compressive strain. This stabilizing surface strain is present in the quantum dot heterostructure due to the mismatch in lattice parameters of the surface and the substrate. In this section, we find the structure of the bonds formed on the Ge (104) surface using a stochastic optimization [6] technique called genetic algorithm Chuang *et al.* (2004) and seek surface stabilizing features in the atomic structure.

An arrangement of the atoms that has lowest surface energy is most likely to reconstruct the surface. Due to a large number of local minima in the surface energy landscape, the lowest energy atomic reconstruction is searched using genetic algorithm. In genetic algorithm (GA), a set of admissible structures are subjected to Darwinian evolution process Deaven and Ho (1995), Landree *et al.* (1997), Chuang *et al.* (2004) as explained in the following procedure.

Genetic algorithm (GA)

1. An initial pool of 50 structures is created by perturbing the atoms lying within top 6Å by a random value less than 10% of the bulk lattice parameter.

[6] Finding atomic reconstruction is an optimization problem where positions of the entire surface and near-surface atoms are optimized in the energy landscape with large number of local minima. Deterministic optimization techniques cannot be used to predict such atomic arrangements Deaven and Ho (1995), Landree *et al.* (1997).

2. These structures are then subjected to conjugate gradient minimization to find free energy of the surface. Forces on the atoms during this minimization are calculated using highly optimized empirical potential developed by Lenosky *et al.* (2000) [7].

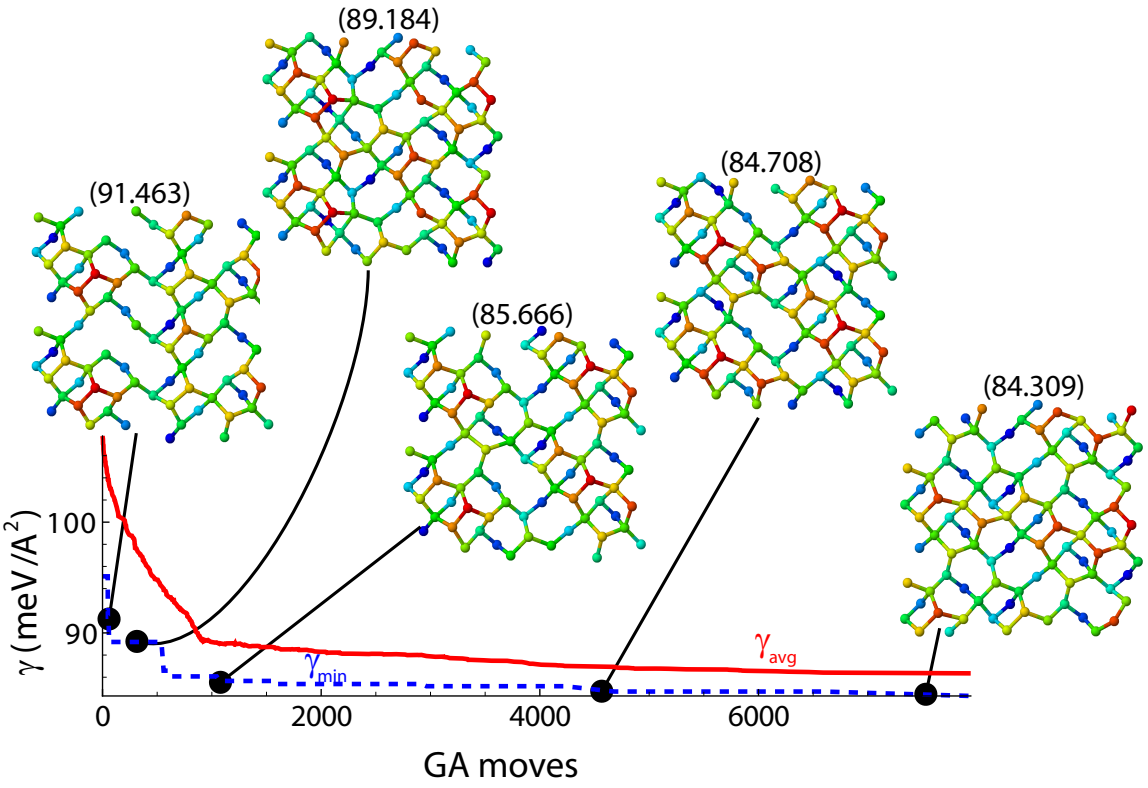

Figure 5.2: Optimization of free energy of (104) surface using genetic algorithm. Average surface energy γ_{avg} (shown by solid line) and minimum surface energy γ_{min} (shown by dashed line) of a pool of 50 structures evolving continuously towards lower surface energy is plotted as a function of number of crossover and/or mutation operations. The lowest energy reconstructions amongst the evolving pool after 50, 200, 1100, 4500, and 8000 genetic operations are shown along with their surface energies (in meV/Å^2).

[7] It is an orthogonal tight binding model of silicon fitted with a minimal *sp* basis and repulsive pair potential and it is known to be more accurate than the potential proposed by Tersoff (1989).

3. Structures of this pool are then subjected to a repeated cycle of genetic operations[8] to create new structures followed by conjugate gradient minimization to evaluate surface energy.

    - After every GA step, if the newly created structures have lower and distinct energy compared to any structure inside the pool then the highest energy structure from the pool is replaced with this new structure.

4. As shown in Figure 5.2, after many such GA moves the average surface energy γ_{avg} of the entire pool reduces and in the process it also gives best candidates to reconstruct the surface.

5. When average surface energy of the pool saturates, the procedure is stopped and the surface energy is recalculated using empirical potential proposed by Tersoff (1989) for germanium[9].

The best 2×1 structure for (104) surface obtained from this search method is shown in Figure. 5.3 (b). Other competing reconstructions are given in Appendix A. As shown in Table 5.1, periodic unit of the (104) surface is larger than (105) surface and hence the (104) surface has a potential for better optimization of its energy and provide a structure which can compete with the SR reconstruction of (105) surface. The free energy density of unstrained surface $\gamma(\theta, 0)$ has major contributions from dangling bonds (db), which are high energy defects on the surface, and stretched bonds, which provide tensile nature to the average surface stress $\sigma_{11} + \sigma_{22}$. Reduction in surface energy with biaxial compression is the product of tensile nature of the

[8] Crossover is done by drawing a rectangular grid of random spacing on the surface of the parent structure and the offspring is created by selecting atoms alternately from the grid-cells of each of the parents. Mutation is performed by either removing or displacing a randomly selected surface atoms.

[9] The structure obtained from genetic algorithm is scaled appropriately to the Ge lattice parameter obtained from Tersoff potential.

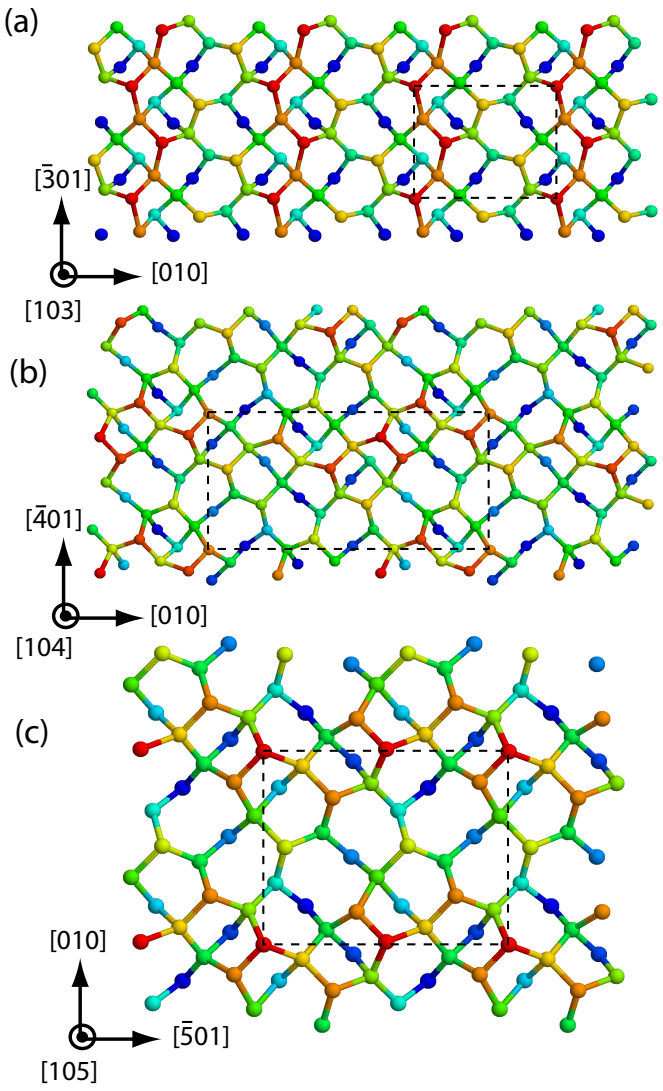

Figure 5.3: Reconstruction of the (103), (104), and (105) surfaces used in calculation of surface energy density. (1×4) reconstruction (Ciobanu *et al.* (2007)) surface (subplot(a)) and SR reconstruction (Khor and Das Sarma (1997)) surface (subplot (c)) are the lowest energy structures known for (103) and (105) surfaces respectively. In this work we obtain the 2×1 reconstruction of (104) surface (subplot (b)) using genetic algorithm. Color of the atoms denote out of plane elevation of the atoms. Unit unit cell of the reconstructed surface is shown by the dashed rectangle

average surface stress and relative arrangement of bonds. As shown in Table 5.1, the best 2×1 reconstruction for (104) surface has high strain sensitivity, its free energy density $\gamma(\theta, 1)$ at 4% compressive strain is close to the corresponding value for SR reconstructed (105) surface. This strain sensitivity of the surface energy density has important implications on the shape of a quantum dot.

Surface	L_x	L_y	L_z	$\gamma(\theta,1)$	$\gamma(\theta,0)$	db/area	$\sigma_{11}+\sigma_{22}$
(103)	a	$\sqrt{5/2}$ a	$\sqrt{5/2}$ a	82.508	85.937	1.581	249.887
(104)	a	$\sqrt{17}$ a	$\sqrt{17}$ a	80.485	83.240	1.455	258.14
(105)	$\sqrt{13/2}$ a	a	$\sqrt{13/2}$ a	80.406	82.054	1.569	145.783

Table 5.1: Comparison of structure, energy, and average stress of reconstructions shown in Figure 5.3. Major contribution to the free energy density of the unstrained surface $\gamma(\theta, 0)$ comes from dangling bonds db and stretched bonds on the surface. The average stress $\sigma_{11} + \sigma_{22}$ of the surface is proportional to the number of stretched bonds per unit cell. Due to the tensile nature of the surface stress, the free energy density of the surface that is subjected to 4% biaxial compression $\gamma(\theta, 1)$ is lower than the energy density of an unstrained surface.

5.3.2 Role of mismatch strain on stability of a pyramidal morphology

At zero strain, the steeper facets have much higher surface energy than shallow facets. Therefore, an unstrained pyramidal island will have shallow facets at equilibrium. However the lattice mismatch strain, present in the islands, can be relaxed better if the facets of the pyramid are steeper (see Figure 5.4). As shown in the Figure 5.5, the surface energies of all three surfaces reduce under biaxial compression.

Free energy of the system, which is sum of surface and relaxation energy, will be lower for the preferred island shape, Figure 5.6 shows one such comparison. Difference in free energies of two shapes 'p' and 'q' are plotted as a function of island size. For lower Ge content (¡20%), the (105) facets are preferred over all physically relevant

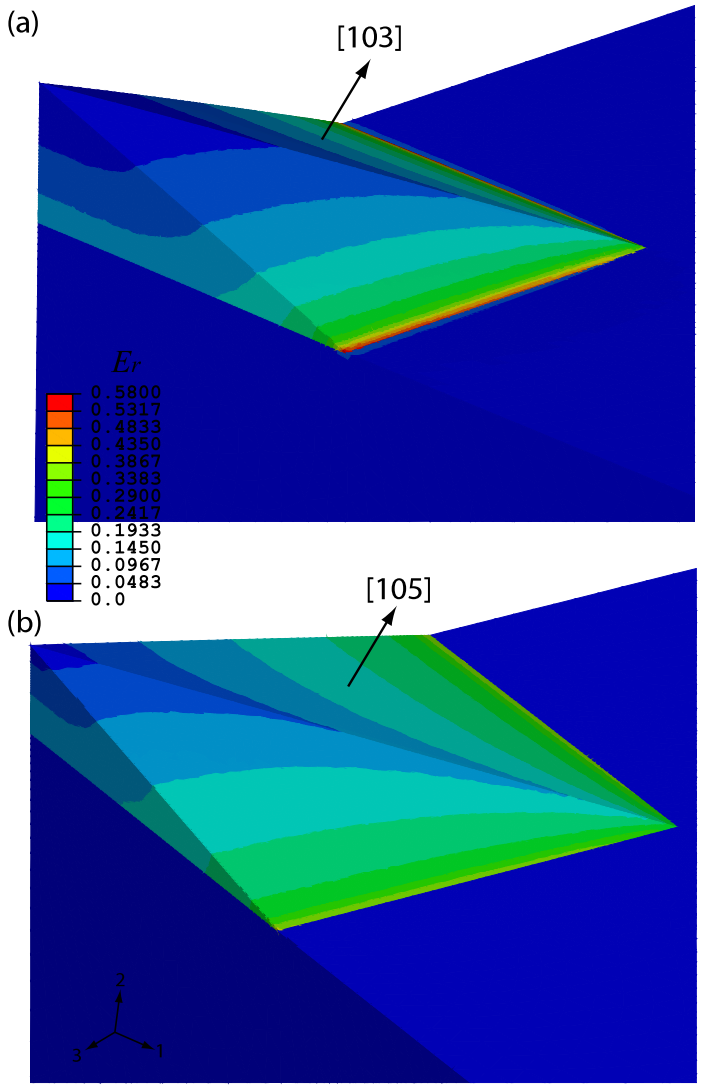

Figure 5.4: Relaxation energy density E_r of (103) and (105) pyramidal island calculated using finite element method. For a fixed volume of a pure Ge island, the (103) facets provide better relaxation of lattice mismatch strain compared to the (105) facets.

sizes of the island. With increase in the size of island the surface energy becomes less important, hence low energy configurations are those which provide better relaxation of mismatch strain. But since the surface energy density of (104) facet is close to that of (105), the pyramidal island does not require excessively high mismatch strain or island size to acquire (104) facet. As seen from Figure 5.6, for a pyramidal islands it

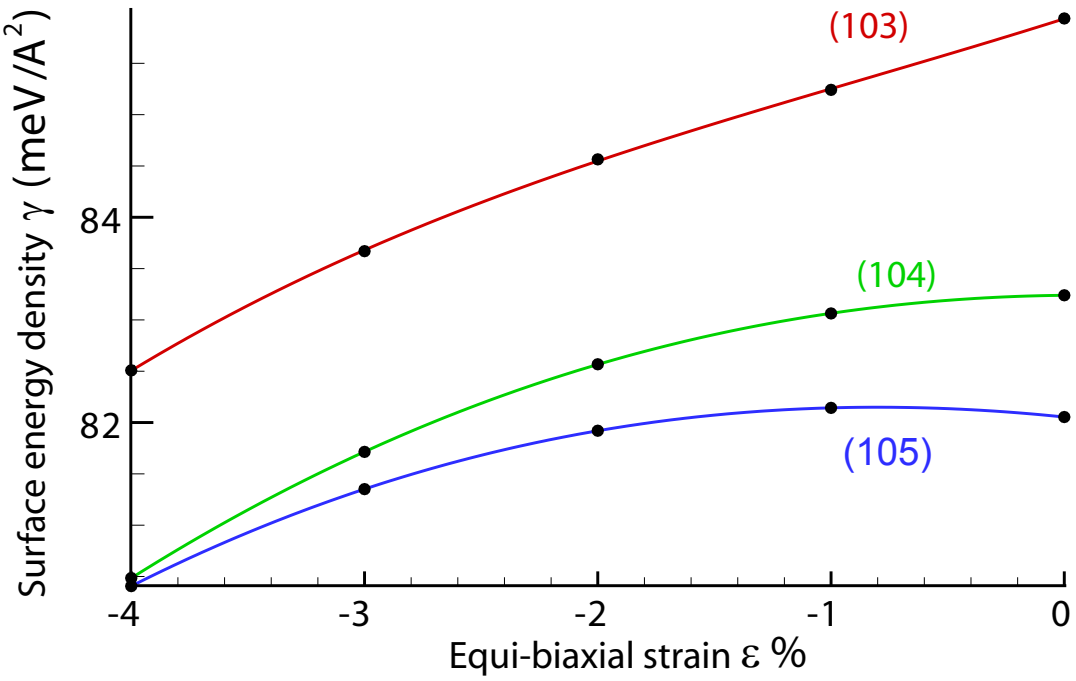

Figure 5.5: Energy density of the reconstructed surface as a function of compressive strain calculated using empirical potential proposed by Tersoff (1989). The surface energy γ reduces with increase in the magnitude of equi-biaxial compression ϵ. At higher compressive strain, the 2×1 reconstruction for (104) surface has surface energy density close to that of SR reconstruction of (105) surface.

takes only 75% average Ge content and 100nm base width to acquire steeper (104) facets.

From the values of free energy per unit volume of the island we construct phase diagram (Figure 5.7) where preferred facet orientations can be traced from average composition and volume of the island. As shown in Figure 5.7, all the (105) pyramidal islands reported by Rastelli *et al.* (2001) and Capellini *et al.* (2005) lie in the (105) domain derived from our calculations. Boundary between different phases of island morphology can be obtained from the length scale imposed by thermodynamics of the system by means of ratio of surface energy density γ and mismatch strain of the

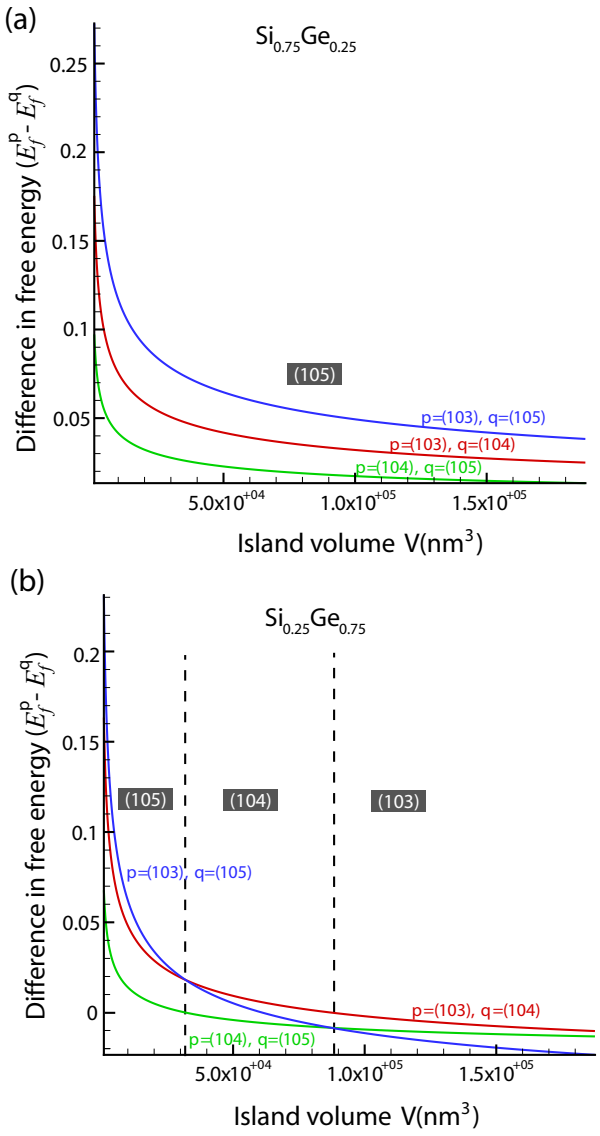

Figure 5.6: Difference in normalized free energy between the configurations 'p' and 'q' as a function of volume of the pyramidal island. Normalization factor is the initial energy, $M\epsilon^2 V$, of a pure germanium island of the same volume. Low energy phases are indicated with filled gray boxes and span of the phase is demarcated by dashed lines where the difference in free energy $E_f^p - E_f^q$ vanishes. For the complete range of volume considered in the subplot(a), the (105) facets have smallest value of E_f/V. However, as the Ge content is increased to 75% (subplot (b)), steeper facets are preferred for the island base width as small as 100nm.

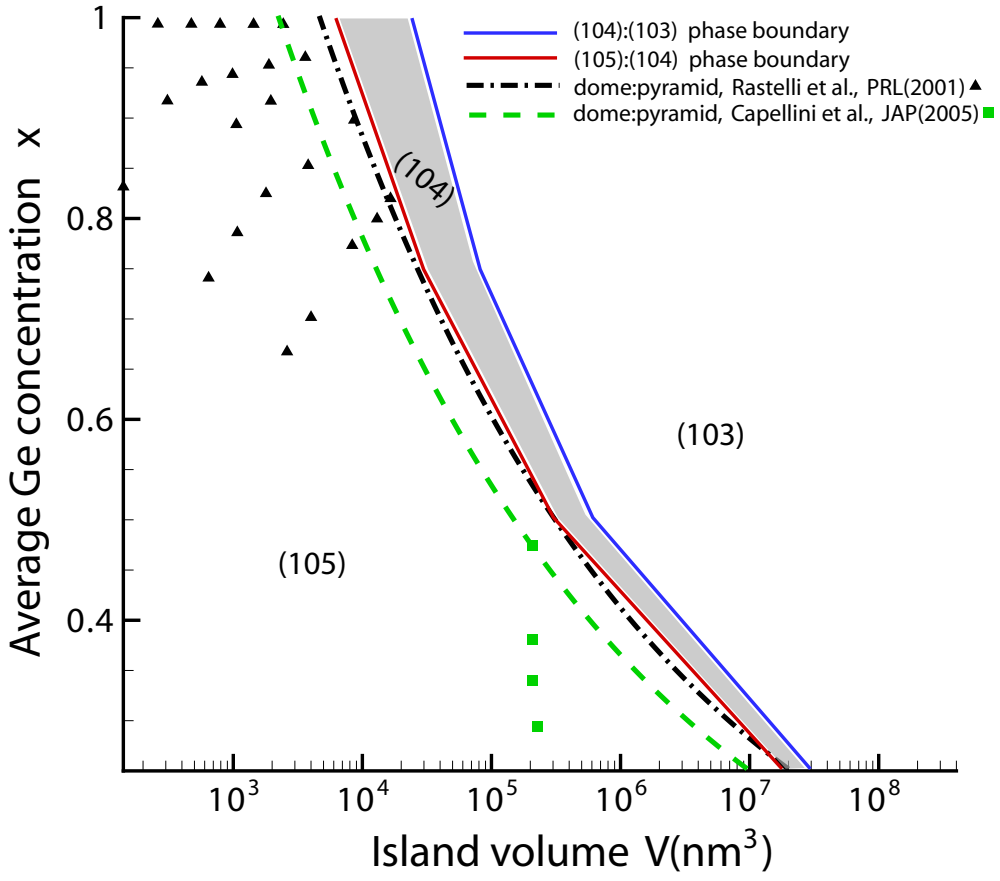

Figure 5.7: Phase diagram for pyramidal islands overlaid with analytical estimates of phase boundaries and experimental observations of island morphologies. The blue solid line is the boundary between (103) and (104) pyramidal islands, the red solid line is the boundary between (104) and (105) pyramidal islands, and the green dashed line and the black dash dot line denote phase boundary between the dome and pyramidal islands estimated by Rastelli *et al.* (2001) and Capellini *et al.* (2005) respectively. The points shown by squares (■) and triangles (▲) are the (105) pyramids observed by Capellini *et al.* (2005) and Rastelli *et al.* (2001) respectively.

island $M\epsilon^2$. From this relation the volume of the island V should scale as a negative sixth power of the average compositon ($V \sim \mathrm{x}^{-6}$). (see Floro *et al.* (1999), Rastelli *et al.* (2001), Capellini *et al.* (2005)). Fortuitously, the phase boundary between

pyramid and dome shape obtained from this scaling relation [10] coincides with the boundary between (104) and (105) pyramids predicted from our calculations. The phase diagram show existence of (104) facets in a small area where (105) begins to be unstable.

5.4 Conclusions

In conclusion, through molecular statics and finite element analysis we have simulated (103) and (104) pyramidal islands reported during growth Yam *et al.* (2001), Le Thanh *et al.* (2000) as well as Si overgrowth Wu *et al.* (2005, 2007) experiments and derived a phase diagram where the region in which the (105) pyramidal island begins to be unstable is shown to coincide with the region where (103) and (104) pyramidal islands are preferred configuration. Our calculations raises an important question: why are the steeper pyramidal islands not observed frequently during the growth experiments? Answer to this question demand experiments which can spot the regions in this phase diagram that are more accessible to capping experiments. We also propose 2×1 reconstruction for Ge(104) surface which, at the level of empirical potential (Tersoff (1989)), has surface energy density close to the SR reconstruction of (105) surface in a biaxially compressed state. Our calculations indicate that, to observe (104) facet the surface should be subjected to biaxial compression [11].

[10] Dome to pyramid transition curve is estimated by Capellini *et al.* (2005) (Rastelli *et al.* (2001)) from $V \sim \epsilon^{-6}$ with a reference point V=9000 nm^3 for x=0.8 (V=5000 nm^3 for x=1).

[11] On a clean and well annealed Ge vicinal (103) surface Gai *et al.* (1997) see shallower (105) facets but do not observe (104) facets.

Chapter 6

Traces of the growth front of actin network bundles

6.1 Introduction

Actin polymerization is one of the key motility machinery used by the eukaryotic cells to transport the endocytic vesicles within the cell, to increase cell surface area by forming microvilli, and to initiate cell crawling by forming pseudopod. This motility machinery is exploited by the pathogenic micro-organisms like *Listeria, Shigella, Rickettsia* and *vaccinia* virus to move within and across the cells. Discovery of actin polymerization as a propulsion means for *Listeria* Theriot *et al.* (1992) has provided a new *in vitro* setup to study this nanomachine. With this setup, biochemistry of the actin-based motility of *Listeria* is understood to the extent that it can be reconstituted with functionalized polystyrene beads using only four purified proteins (Loisel *et al.* (1999)): actin, arp2/3, capping protein and cofilin. *In vitro* experiments have also been carried out using extracts from frog egg, bovine brain cells, and platelet cells with functionalized lipid vesicles and oil drops.

Several models (Gerbal *et al.* (2000), Carlsson (2001), Dickinson and Purich (2002), Mogilner and Oster (2003), Alberts and Odell (2004), Dickinson (2006)) have been proposed to gain theoretical understanding of this actin motility machinery. Microscopic models of Mogilner and Oster (2003) and Alberts and Odell (2004) are based on a postulate that thermal fluctuations of individual actin filaments provide ratcheting effect which propels the bacterium while incorporating new monomer on the filament. Continuum model of Gerbal *et al.* (2000) are based on viscous-type resistance arising from breakage of bonds at the surface of the bacterium. Dickinson and Purich (2002) have proposed existence of an end-tracking motor that uses energy of ATP hydrolysis to regulate the polymerization process. Dickinson (2006) have argued that motion of vesicles, beads and *Listeria* are limited by diffusion of actin proteins to the core of the comet tail. All of these models have focused on either force velocity relation and/or saltatory (jerky) motion arising from the actin polymerization motor, none of the models attempt to reproduce long term trajectories of motion.

A completely different, top-down, approaches of Rutenberg and Grant (2001), Balter and Tang (2005), Shenoy *et al.* (2007) interpret kinematics of the motion based on information stored in shapes of the trajectories. Rutenberg and Grant (2001) propose a statistical model where a distribution of curvatures of the trajectories is obtained from randomness of the fiber orientation and distribution of surface proteins enable actin-based propulsion of the "cargo". Balter and Tang (2005) propose a hydrodynamic model where drag on the actin filament network is considered to be the cause for helical shape of the trajectories of unconstrained motion of the bacterium. These two models do not provide a clear explanation for variety of trajectories displayed by the actin propelled bacterium. Shenoy *et al.* (2007) propose a model based on a hypothesis of an effective force and provide a unified description of variety of trajectories observed during *in vitro* experiments on *Listeria monocytogenes*. By reproducing

the planar as well as 3D trajectories of *Listeria*, Shenoy *et al.* show that this motion can be captured by deterministic equations. However, this model assumes that the effective force remains parallel to the axis of the bacterium. In this chapter, we will discover that if this constraint is lifted, the model will also reproduce the trajectories of spherical beads[1]. Evidence for this additional degree of freedom of the force will be shown by reproducing the observed trajectories (Cameron *et al.* (1999) and Sykes [2]). We will also see that this generalization of the effective force model also explains trajectories of elliptical beads. We will begin with noting differences in the shape of continuous trajectories of *Listeria*, spherical bead, and elliptical beads. After analyzing trajectories with this model, we will discuss possible connection of this model with microscopic details of the actin based propulsion. This section is included to describe some logical deductions from the experimental data and it is meant for future development of the kinematic model to the microscopic scale.

6.2 Differences in the trajectories of various objects

Many groups have reconstituted motility with engineered cargoes such as polystyrene beads of different shapes, vesicles, and oil drops in variety of motility medium. The surface of the cargo is functionalized with certain proteins (eg. ActA, VCA, WASP) and placed in the motility medium containing at least ATP, actin, arp2/3, cofilin, and capping proteins. This mixture is kept between a glass slide and a cover slip and the motion of particle is observed under optical microscope typically at 100X

[1] We will focus only on planar motion of the objects constrained by a slide and a cover slip as shown in Figure 6.2

[2] Long trajectories of funcitonalized 0.5μm spherical beads in HeLa cell extract are published on Cécile Sykes group webpage http://www.curie.fr/recherche/themes/detail_equipe.cfm/lang/_gb/id_equipe/221.htm

magnification. We will focus on only those experiments where long term trajectories are reported. It is important to note that this model does not take into account the detailed biochemistry of the medium so this information is omitted from the following discussion.

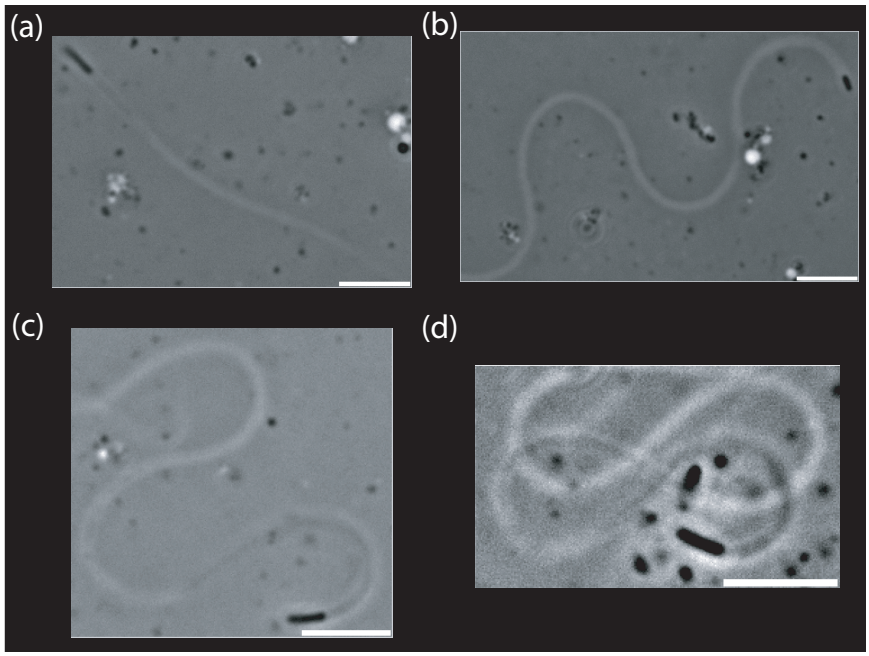

Figure 6.1: *In vitro* trajectories of *Listeria monocytogens* moving in a Xenopus egg extract. All the trajectories shown here have at least one complete period of motion and all of them have zero mean curvature. Scale bar shown in the phase contrast images correspond to 5 μm.

Figure 6.1 shows representative long term trajectories of *Listeria monocytogenes* moving in a two dimensionally constrained Xenopus egg extract (also see Lasa *et al.* (1997), Rosenblatt *et al.* (1997), Gerbal *et al.* (2000), Soo and Theriot (2005), Shenoy *et al.* (2007)). All these trajectories have zero mean curvature but the trajectories of the spherical bead (Cameron *et al.* (1999) and Sykes [2]) have non-zero mean curvature with a magnitude that stays constant over a period of several minutes. Cameron *et al.* (1999) also observed that some spherical beads display quasi-periodic sharp turns.

Functionalized elliptical beads [3] , on the other hand, prefer to move along its long or short axis rather than any other orientation. When these elliptical beads are coated with lipid membrane, they move only along a circular path (Theriot [3]). In the next section we will see that all of these observations can be explained by the effective force model Shenoy *et al.* (2007).

6.3 Model based on kinematics of an effective force

According to the effective force model (Shenoy *et al.* (2007)), a constant force that rotates about the axis of the bacterium with a velocity ω provides a constant translational velocity $\dot{s} = v(F)$ and a constant torque $\tau_\perp = Fd$. The resulting angular velocity of the growth front of the comet tail is $\dot{\theta} = \Omega(\tau_\perp)\cos(\omega t)$ [4] and curvature of the trajectory is $\kappa = \dot{\theta}/\dot{s} = (\Omega/v)\cos(\omega t)$. Mean curvature κ_m of such trajectory is zero. Trajectories of the spherical beads, however, have non-zero mean curvature (Cameron *et al.* (1999) and Sykes [2]) that remains constant over several minutes. Equation for the curvature of such trajectories can be written as $\kappa = (\Omega/v)\cos(\omega t) + (\beta/v)$, where β/v is the constant mean curvature. Now since we observe a non-zero κ_m for spherical beads, which remains constant over several minutes, the equation for curvature of the trajectory of spherical bead is Angular velocity of the growth front becomes $\dot{\theta} = \Omega\cos(\omega t) + \beta$, which conveys physical meaning of β as an angular velocity of the force about an axis normal to the plane of motion. Physically Ω is the rate of change of normal of the growth front for $\omega = 0$. From this analysis we propose that effective force on the spherical beads have an additional degree of freedom β

[3] Julie Theriot's presented an observation that at American Physical Society meeting 2002 that the functionalized elliptical beads either move along minor axis or major axis inside the cell extract. Link: http://www.aps.org/meetings/multimedia/biology-2002.cfm

[4] All the arbitrary constants are eliminated from the equations to keep them transparent.

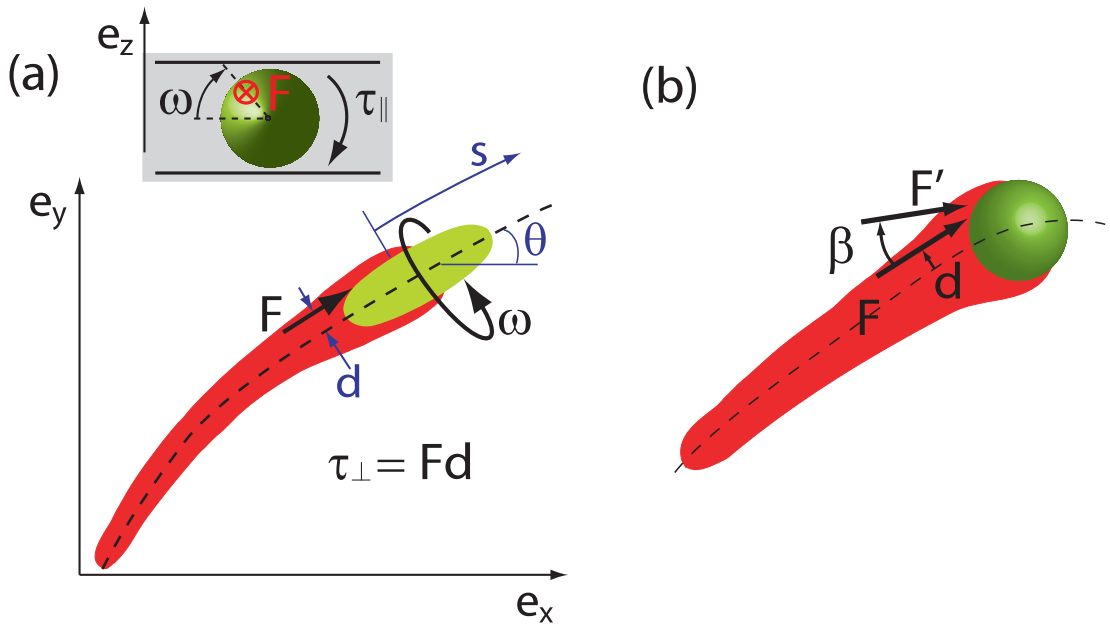

Figure 6.2: Kinematics of the effective force F acting on the bacterium (a) and spherical bead (b). Shenoy *et al.* (2007) assumes the force to remain parallel to the axis of the bacterium while acting at an offset d and rotating at a velocity ω about the tangent to the trajectory. Additional degree of freedom β, interpreted from the information conveyed by the trajectories of spherical bead, is the angular velocity of the force about the axis normal to the plane of motion. The force F' on the spherical bead is the same force F rotated by an angle β after a unit time. $\tau_\perp$ is the torque arising from the offset of the force with respect to the tangent of the trajectory. $\tau_\parallel$ is the torque due to rotation of the force about the tangent of the trajectory with a velocity ω.

that provides nonzero mean curvature to the trajectories. Physical reasons for such additional degree of freedom for force are discussed in Section 6.5.1.

Figure 6.3 shows the effect of introducing β in the equation of motion. This additional degree of freedom makes the object to turn back rather than moving forward. A more detailed analysis of the equation of motion reveals that most of the trajectories are closed as opposed to the trajectories of *Listeria*. For the trajectories of *Listeria*, when (Ω/ω) = one of the zeros of the Bessel function $J_{(\Omega/\omega)}$ the resulting trajectory is a closed loop with two lobes. With every higher zero of the Bessel function there is addition of a sub-loop in the lobes of the trajectory. This condition comes from equating total distance traveled by the object over a complete period to zero (for similar calculation see Shenoy *et al.* (2007)). For spherical beads, in addition to (Ω/ω) = one of the zeros of the Bessel function $J_{(\beta/\omega)}$ (see Figure 6.5), closed trajectories are also obtained if (β/ω) is a rational number. In the second condition, let (β/ω) = (p/q) where p and q are integers, then p gives number of periodic repeats and the time required to close the trajectory, with q lobes, is $(2\pi q/\omega)$ (see Fig.6.4). This new equation of motion also predicts sharp turns (Cameron *et al.* (1999)) in the trajectory (see Figure 6.4 with $p/q = 1/2$). The equation for orientation of the propulsive force is

$$\theta = \left(\frac{\Omega}{\omega}\right)\sin(\omega t) + \left(\frac{\beta}{\omega}\right)\omega t. \tag{6.1}$$

This equation provides complete description of the trajectories using only two independent parameters (Ω/ω and β/ω). As shown in Figure 6.3, if $\beta > \Omega$ the curvature of the trajectory never switches sign. Now let us understand the physical meaning of all the variables of the model.

In the next section, the Equation 6.1 is shown to reproduce two set of experimental trajectories (Sykes [2], Cameron *et al.* (1999)).

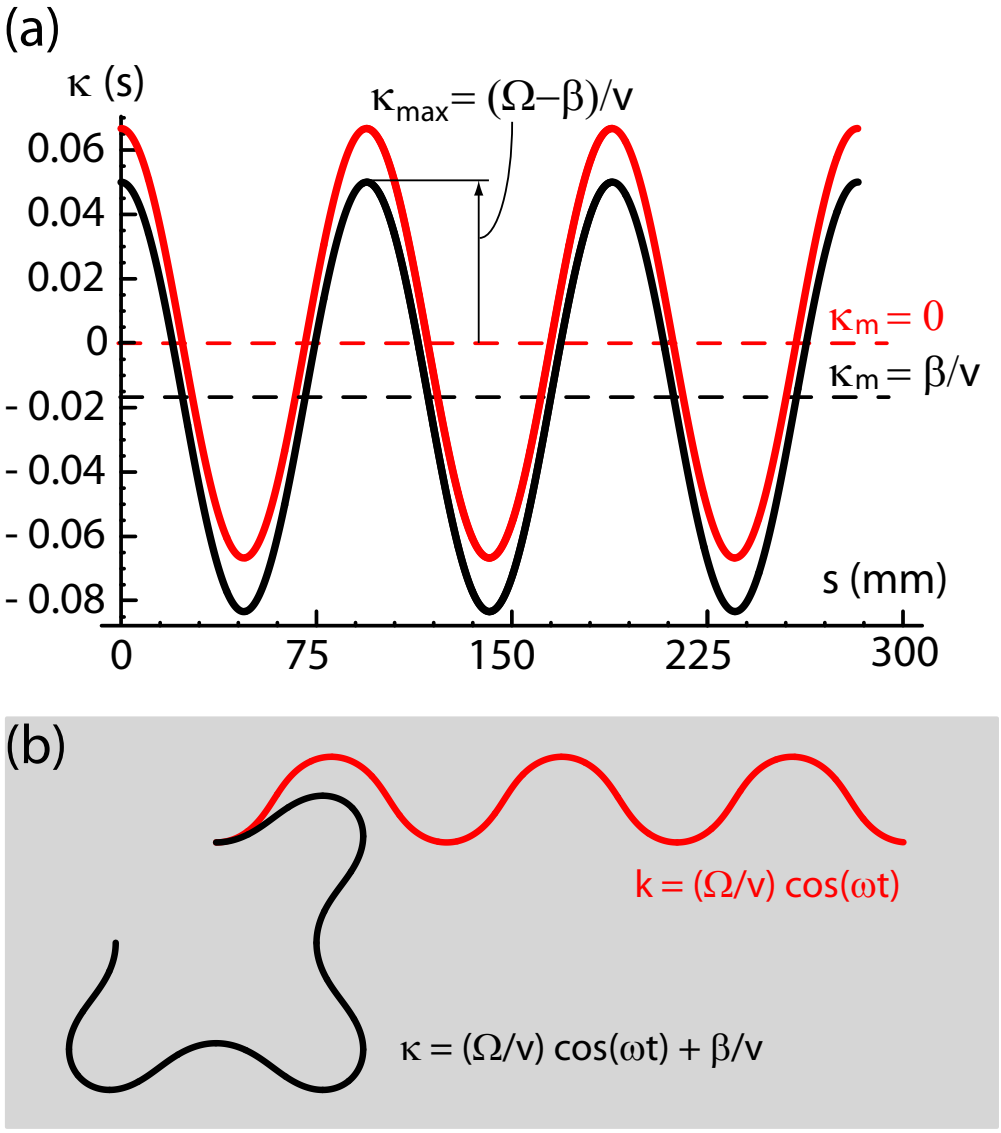

Figure 6.3: Difference in the shape of representative trajectory (b) of *Listeria* (red curves) and spherical bead (black curves) and their curvatures (a). Values of the parameters used to obtain the trajectories are, v = 0.15 μm/s, ω = 0.01 rad/s, Ω = 0.01 rad/s, $\theta_0 = \phi_0 = 0$, β = -(1/4)ω, T = 2000 s.

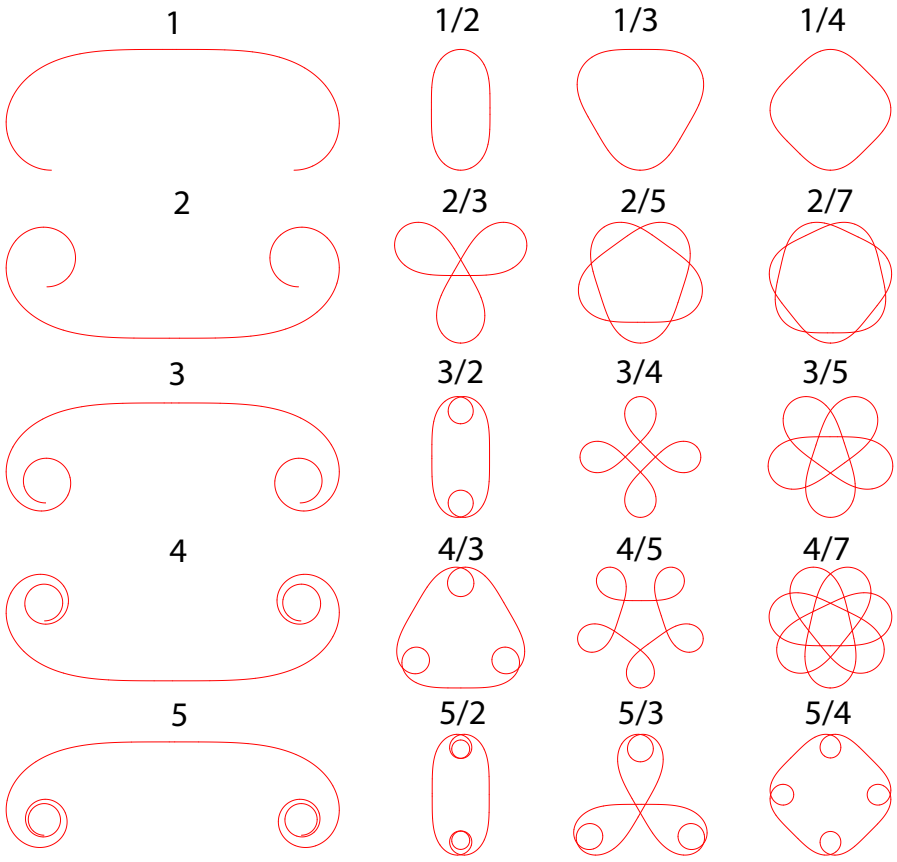

Figure 6.4: Shape of the trajectories with $(\Omega/\omega) = \beta/\omega$. Values of other parameters are, $\beta = p(\omega/q)$, v = 0.1 μm/s, ω = 0.03 rad/s, $\Omega = \omega(\beta/\omega)$ rad/s, $\theta_0 = \phi_0 = 0$, T $= (2\pi/\omega)(\beta/\omega)$ s where p and q are integers. Corresponding value of $\beta/\omega = p/q$ is written above the trajectory.

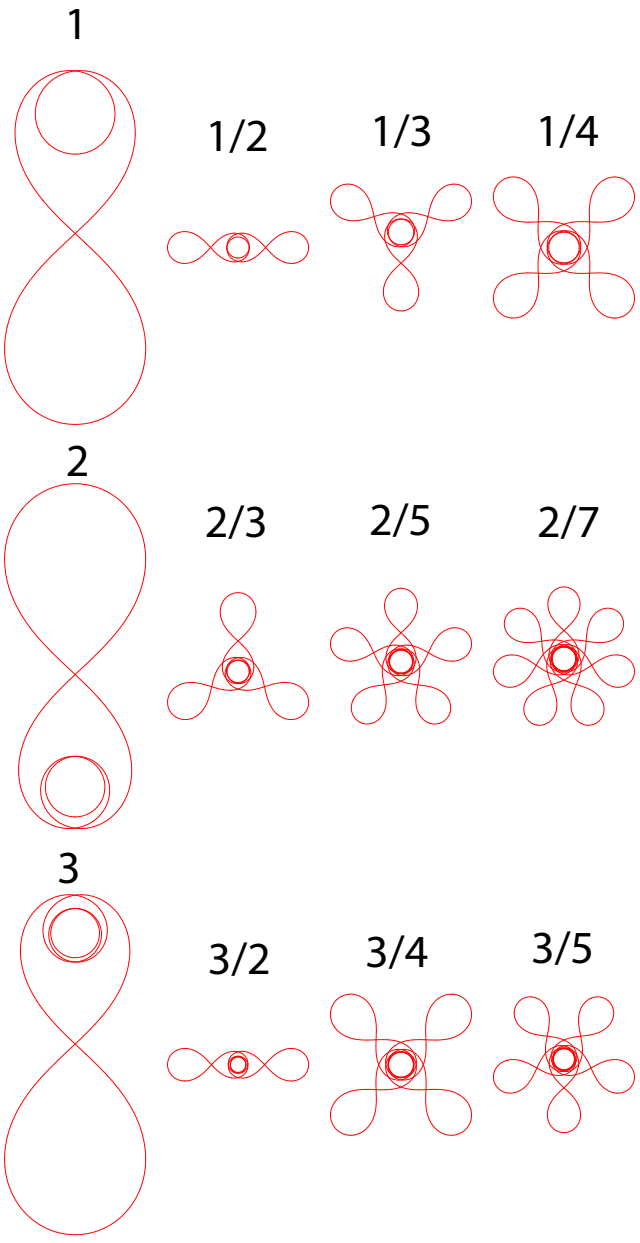

Figure 6.5: Shape of the trajectories with (Ω/ω) = first zero of the Bessel function $J_{(\beta/\omega)}$. Other parameters are, $\beta = p(\omega/q)$, v = 0.1 μm/s, ω = 0.03 rad/s, $\Omega = \omega\ \mathrm{J}_0(\beta/\omega)$ rad/s, $\theta_0 = \phi_0 = 0$, T = $(2\pi/\omega)(\beta/\omega)$ s where p and q are integers. Corresponding value of $\beta/\omega = p/q$ is written above the trajectory.

6.4 Comparison of theoretical and experimental trajectories of motion

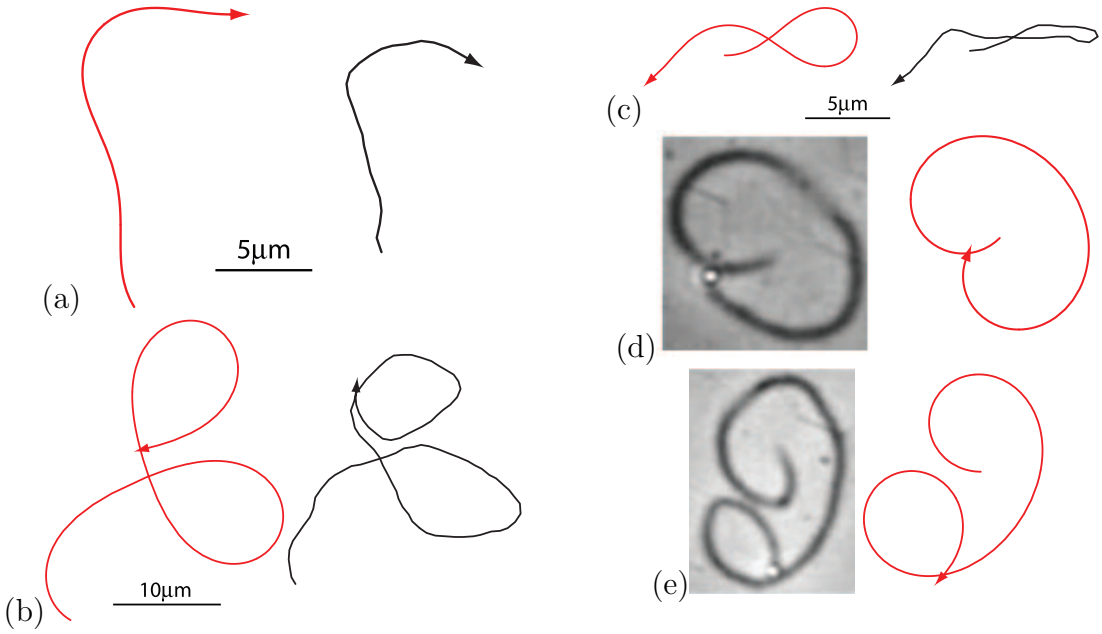

Figure 6.6: Comparison of theoretical (red curve) and experimental (black curve) trajectories of motion of spherical beads. Data from two set of experiments (Cameron *et al.* (1999), Sykes [2]) which have long term trajectories is used in this comparison. Cameron *et al.* (1999) have 0.5m beads symmetrically coated with ActA moving in the Xenopus egg extract, images (a), (b), and (c). Sykes [2] have 0.5m beads asymmetrically coated with the VCA and placed in HeLa cell extracts, images (d) and (e). The comets appear dark in the phase contrast image of the trajectory, the bead diameter is 0.5μm. Trajectories (d) and (e) are still images and we do not have time lapsed data leading to the state shown there.

There are only a couple of experimental studies on the motility of spherical beads with long term trajectories are even rare. Major difficulty is the numerous delicate processes that each ingredient of the experiments has to go through to get the right combination for motility to take place. In Figure 6.6 two set of experiments that have clear and long term trajectories parameters used to obtain the theoretical estimates shown in red are given in Table 6.1.

	ω	Ω	$\dot{\beta}$	Ω/ω	$\dot{\beta}/\omega$	θ_0	ϕ_0	t_{max}	p	q
(a)	0.06	-0.034	-0.0162	-0.567	-0.27	-1	0.6	144	-10	37
(b)	0.025	0.015	-0.0192	0.6	-0.77	$-\pi/6$	3.3	610	-10	13
(c)	0.05	-0.07	-0.024	-1.4	-0.47	-0.024	3.17	170	-9	19
(d)	-0.048	0.024	-0.06	-0.5	1.25	$\pi/4$	3.7	145	5	4
(e)	-0.048	0.028	-0.055	-0.58	1.14	0	4.2	195	8	7

Table 6.1: Values of parameters used to make the theoretical trajectory in Figure 6.6. All the trajectories have same velocity of 0.15μm/s.

6.4.1 Comments on elliptical beads

The elliptical beads are observed to move along their geometric axis (Theriot [3]). We interpret this type of motion as manifestation of some stabilizing mechanism acting at the symmetric region of the object. This stabilizing mechanism makes force prefer regions close to the points of symmetry. On the other hand, the elliptical beads coated with lipid membrane move only along a circular path with bead oriented along the long axis. We interpret this as the symmetric points of high curvature (black colored region in Figure 6.7) being more stable than the flatter symmetric points (red colored band on Figure 6.7) and mobility of surface proteins make more stable region accessible. As a result, the comet tail the elliptical bead oriented along the long axis. Equation of motion of the spherical bead can be generalized further by including the stabilizing effects of the symmetric points.

A geometric term Γ, which depends on the orientation of the tangent of the trajectory with respect to a reference axis of the bead (βt), can be introduced in the equation of motion,

$$\dot{\theta}(t) = \Omega \cos(\omega t) + \beta\ \Gamma(\beta, t). \tag{6.2}$$

A general form for the geometric term is $\Gamma = \Gamma_0(\kappa''/\kappa_0'')$, where Γ_0 is a parameter defining magnitude of the geometric effect, κ'' locates symmetric points, and κ_0'' is a normalizing constant.

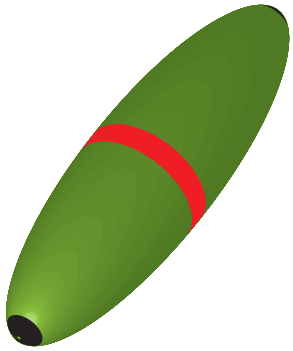

Figure 6.7: Points where the force is stable against rotation (β) about the axis normal to the plane of rotation. The region shown by black color is more stable compared to the region colored in red.

The model proposed by Shenoy et al. and its modification described in this chapter has several assumptions regarding effective force and its kinematics, in the next section we discuss microscopic basis for these assumptions.

6.5 Microscopic basis for kinematics of the effective force

The effective force model explains trajectories of spherical and elliptical beads, various bacteria and oil drops (Shenoy *et al.* (2007)). This section draws attention to some microscopic reasons for an effective force and its kinematics. The microscopic basis presented here is based on various microbiological experiments and it is amenable to simple computational and experimental verification. It is, however, important to note that the computational implementation necessarily needs discrete

modeling [5].

6.5.1 Microscopic origin of an effective force

Actin based motility is a result of localized polymerization of actin filaments on the surface of the cargo. Once a dense network forms around the cargo further polymerization can take place only by pushing the object forward. We adopt a hypothesis where all the filaments touching the surface of the object are considered as "active" filaments. These filaments can push or pull the object based on their rate of elongation compared to the neighboring active filaments. The distributed forces can be replaced with an equivalent force and a effective torque by placing this effective force at an offset from the axis of the object. Since the trajectories considered in this chapter are planar, the direction of unbalanced force also lies in the plane of motion. Any out-of-plane component of the force is balanced by the reaction from the slide and the cover slip (see inset from Figure 6.2(a)). The kinematic model assumes the effective force to have two degrees of freedom ω and β as shown in Figure 6.8. In the following discussion, these degrees of freedom are attributed to collective *rearrangement of the filaments* that are part of the comet tail network.

6.5.2 Microscopic mechanism for ω

ω represents the angular velocity of effective force about the tangent of the trajectory and can be best explained with motility of *Listeria*. Since the effective force is constrained to the pole, with its direction parallel to the axis of the bacterium, the trajectory will have a constant nonzero torsion only if the force rotates about the axis of the bacterium with a constant angular velocity ω (Shenoy *et al.* (2007)). But

[5] There is no continuum model which captures, for example, rotation of the force about the axis of the bacterium arising from the mechanism described in Figure 6.9(a).

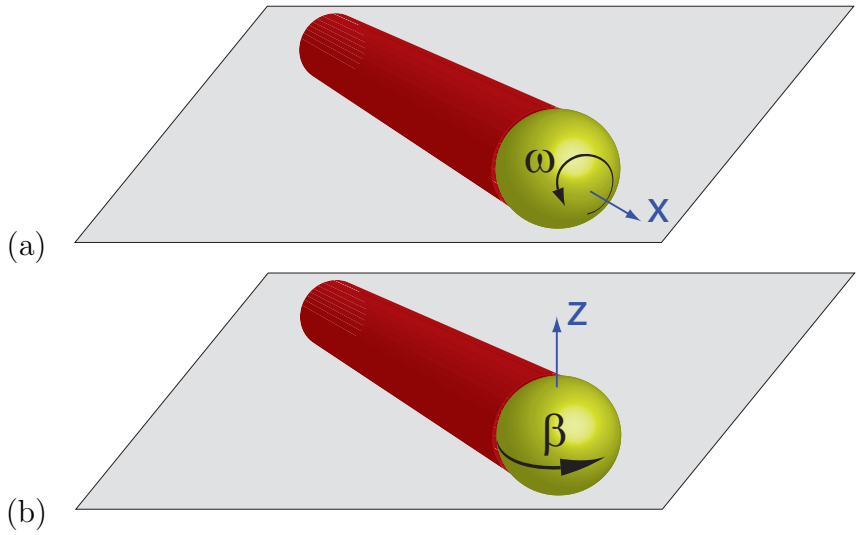

Figure 6.8: Degrees of freedom of the effective force arising from 2D constraint. Any other motion of force is balanced by the constraints.

the rotation of the force does not necessarily mean rotation of the cargo, hence, the rotation of force is not correlated to the rotation of the object.

Cameron *et al.* (2004) attached a tiny bead on the side of *Listeria monocytogenes* and for each turn in the trajectory they noted whether the projected position of the bead lies inside or outside of the curve. It was observed that there is no correlation between the location of the bead and the direction of turn. These experiments prove that the effective force rotates relative to the bacterium and rules out any significant variation ActA density at the polar end of the bacterium. An important data missing from Cameron *et al.* (2004) is the direction of rotation of the bacterium, which, if compared with the direction of rotation of the effective force can guide further development of a model for such rotation. Oil drops and lipid vesicles, which also serve as a force transducers (Upadhyaya and van Oudenaarden (2003)), have mobile surface proteins. Tricher *et al.* (2007) report sinusoidal trajectories for actin propelled oil drops which indicate presence of torsion these trajectories.

Zeile et al. (2005) propose a point torque model for torsion of the trajectories

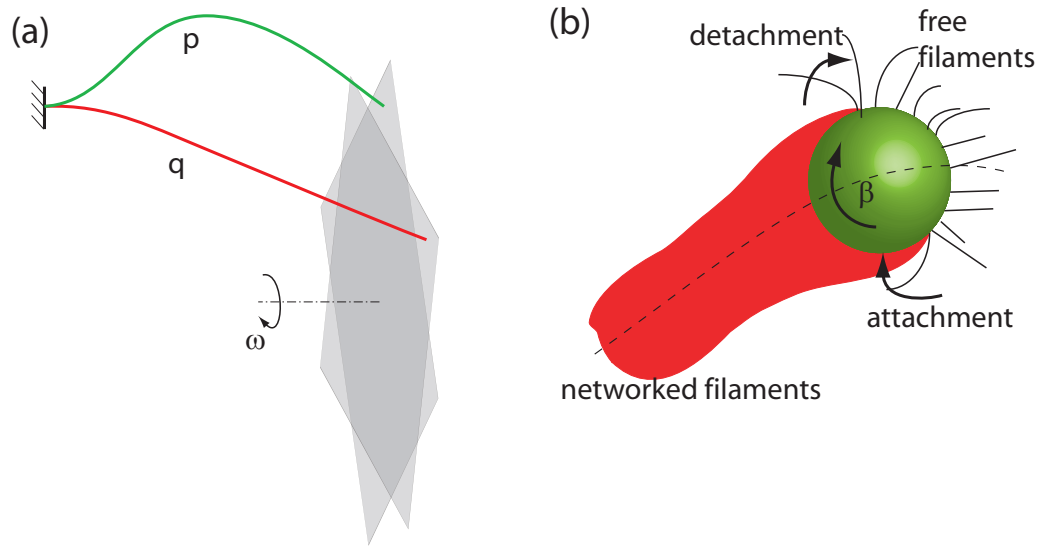

Figure 6.9: Filament elasticity based model for rotation of the force about the axis of the bacterium. (a) Energetically it is favorable to accommodate the change in end-to-end distance of the actin filament by bending (state q) it rather than compressing or buckling (state p) it. It is important to note that similar mechanism must be active when the cargo surface moves towards a filament. (b) The actin filaments polymerize all around the bead, some are part of the network that forms comet tail and others are free. Steady incorporation and release of active filaments from the edge of the comet tail is shown as a possible mechanism for the degree of freedom β.

of *Listeria monocytogenes*. This model, based on point torques applied by twisted filaments, will predict zero torsion for the trajectory of oil drops since the fluid surface cannot support point torques. We propose a mechanism shown in Figure 6.9(a) for torsion in the trajectories of the soft as well as hard cargoes. According to this mechanism, compression of the filaments is accomodated by low energy bending mode of relaxation. Such a relaxation can lead to a directed motion of the surface proteins away from the axis of the object and around the tangent of the trajectory. Now if large number of filaments under compression, then cooperative bending relaxation can introduce torsion in the comet tail. This cooperative non-affine deformation will introduce higher torsion in the comet tails with tighter network as indicated by straighter trajectories with fimbrin as cross linkers as opposed to α-actinin (see Brieher *et al.* (2004)). Further progress in the microscopic model requires experimental measurement of bending of the filaments of the comet tail under different chemical environment.

6.5.3 *Symmetry of the object and distribution of the surface proteins gives rise to* β

β represents angular velocity of the force or tangent of the trajectory with respect to the object about an axis normal to the plane of motion. A constant non-zero mean curvature of the trajectory where the force lies in the plane of motion is interpreted as a constant rotation of force with respect to the cargo. However in the wild-type *Listeria*, the force stays aligned with the bacterial axis (i.e. β=0) due to a geometrical constraint arising from the envelope of actin network formed around the cylindrical object (see Figure 6.2(a)). In addition to this constraint, the bacterium has polarized distribution of ActA (Rafelski and Theriot (2006)) which makes polar region even more favorable for the comet tail and hence β is not present in the wild-type *Listeria*.

In case of the spherical beads, geometric symmetry and non-polarized distribution of surface proteins allow motion of the effective force around the bead as shown in Figure 6.2(b). Microscopically, such motion must be sustained by steady incorporation of new filaments from one side and release of existing filaments from the other side of the comet tail as shown in Figure 6.9(b).

From this perspective, the skidding motion of mutated *Listeria* (Lauer *et al.* (2001)) can be inferred as manifestation of reduced "hoop strength" of the comet tail[6] due to the specific set of proteins recruited by mutated ActA.

For oil drops and vesicles, the mechanism shown in Figure 6.9(b) will cause accumulation of surface proteins towards the rear end of the object. Hence this mechanism will predict zero mean curvature (i.e. β=0) for the trajectories of oil drops and vesicles. Long term trajectories of oil drops reported by Tricher *et al.* (2007) confirms this prediction of zero mean curvature. Further development of microscopic model require experimental confirmation of filament incorporation mechanism shown in Figure 6.9(b) and its kinetic properties.

6.6 Conclusions

In this chapter we have generalized the kinematic model of Shenoy *et al.*, which was developed for the motion of *Listeria monocytogenes*, and explained the shapes of trajectories of spherical and elliptical beads. The trajectories of the spherical beads have nonzero mean curvature, whereas the trajectories of *Listeria* have zero mean curvature. The modified kinematic model presented in this chapter emphasizes relative motion between the cargo and its comet tail and provides qualitative explanation for the trajectories of oil drops. The microscopic basis for kinematics of the force, and

[6]Movies in the supplementary material of this paper indicate alignment of long axis with the tangent to the trajectories is still a preferred orientation (possibly due to polarity of the ActA proteins).

its predictions, provide guidelines for further experiments and modeling to develop a microscopic theory of actin-based motility.

Appendix A

Other structures for (104) surface

Genetic algorithm gives best possible choices for a surface. The solution set also include some structures that are slightly higher in energy but might be more stable in certain environment. In this appendix four best structures obtained from the stochastic search are reported along with their surface energy density γ as a function of equi-biaxial strain ϵ.

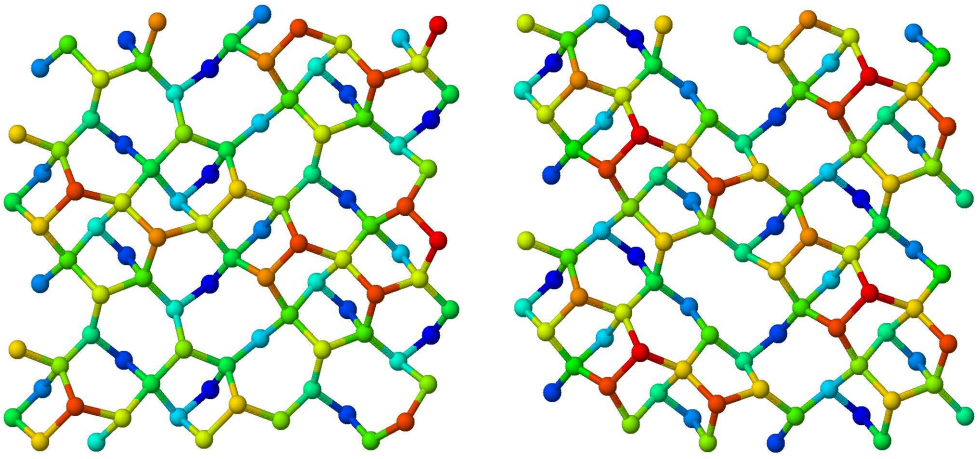

(a) (b)

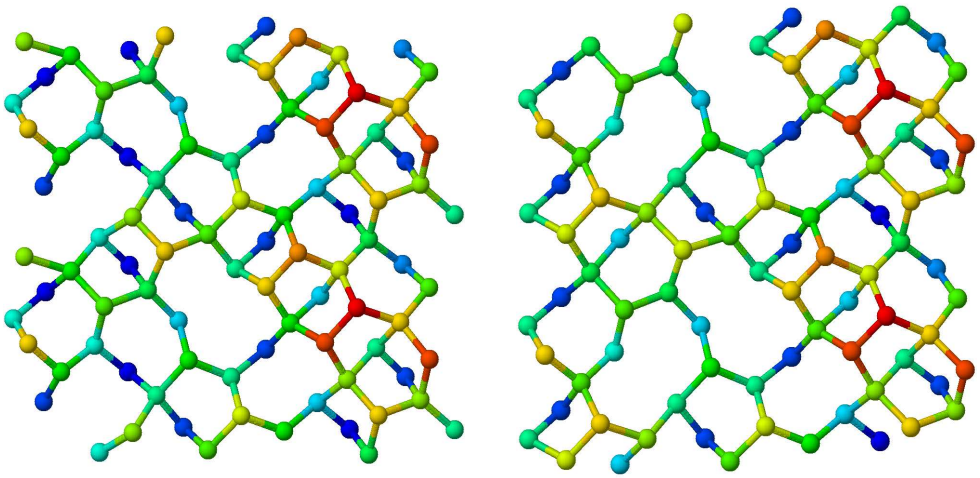

(c) (d)

Figure A.1: Atomic structure of the four best structures for (104) surface obtained from genetic algorithm. Structure shown in (a) is same as the one in Figure 5.3(b).

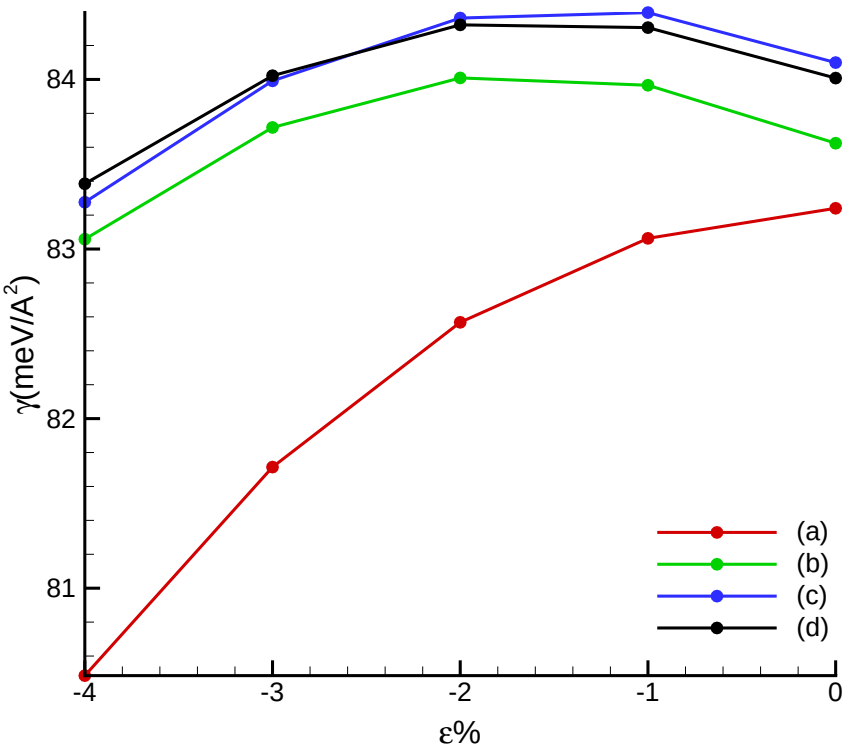

Figure A.2: Surface energy density γ as a function of strain ϵ for the four best structures obtained from genetic algorithm. The label for each curve corresponds to the structure in Figure A.1.

Bibliography

Alberts, J. B. and Odell, G. M. (2004), 'In silico reconstitution of Listeria propulsion exhibits nanoscale saltations', *Public Library of Science, Biology* **2**, e412. 1.2, 6.1

Alerhand, O. L., Vanderbilt, D., Meade, R. D. and Joannopoulos, J. D. (1988), 'Spontaneous Formation of Stress Domains on Crystal Surfaces', *Physical Review Letters* **61**, 1973. 3.3

Balter, A. and Tang, J. X. (2005), 'Hydrodynamic stability of helical growth at low Reynolds number', *Physical Review E* **71**, 051912. 6.1

Brieher, W. M., Coughlin, M. and Mitchison, T. J. (2004), 'Fascin-mediated propulsion of Listeria monocytogenes independent of frequent nucleation by the Arp2/3 complex', *Journal of Cell Biology* **165**, 233. 6.5.2

Cameron, L. A., Footer, M. J., van Oudenaarden, A. and Theriot, J. A. (1999), 'Motility of ActA protein-coated microspheres driven by actin polymerization', *Proceedings of National Academy of Sciences U. S. A.* **96**, 4908. 6.1, 6.2, 6.3, 6.3, 6.3, 6.6

Cameron, L. A., Robbins, J. R., Footer, M. J. and Theriot, J. A. (2004), 'Biophysical parameters influence actin-based movement, trajectory and initiation in a cell-free system', *Molecular Biology of the Cell* **15**, 2312. 6.5.2

Capellini, G., De Seta, M., Di Gaspare, L., Evangelist, F. and dAcapito, F. (2005), 'Evolution of Ge/Si(001) islands during Si capping at high temperature', *Journal of Applied Physics* **98**, 124901. 5.2, 5.3.2, 5.7, 10

Carlsson, A. E. (2001), 'Growth of branched actin networks against obstacles', *Biophysical Journal* **81**, 1907. 1.2, 6.1

Chang, C. S., Huang, Y. M., Chen, C. C. and Tsong, T. T. (1996), 'Anisotropic interaction of Ag-induced missing dimer vacancies on Si(001) surfaces', *Surface Science* **367**, L8. 2.1, 2.2, 2.3.1, 2.5.1, 2.5.2

Chaparro, S. A., Zhang, Y. and Drucker, J. (2000), 'Strain relief via trench formation in Ge/Si(100) islands', *Applied Physics Letters* **76**, 3534. 4.1, 4.2, 4.3, 4, 4.3, 4.5, 5.2

Chaparro, S. A., Zhang, Y., Drucker, J., Chandrashekhar, D. and Smith, D. J. (2000), 'Evolution of Ge/Si(100) islands: Island size and temperature dependence', *Journal of Applied Physics* **87**, 2245. 4.1, 4.2, 4.3, 4.3

Chen, X., Wu, F., Zhang, Z. and Lagally, M. (1994), 'Vacancy-Vacancy Interaction on Ge-Covered Si(001)', *Physical Review Letters* **73**, 850. 2.1, 2.5.1, 2.5.2

Chey, S. and Cahill, D. (1997), 'Surface defects created by low energy (20 ¡ E ¡ 240 eV) ion bombardment of Ge(001)', *Surface Science* **380**, 377. 2.1, 2.5.1, 2.5.3

Chuang, F., Ciobanu, C., Shenoy, V., Wang, C. and Ho, K. (2004), 'Finding the reconstructions of semiconductor surfaces via a genetic algorithm', *Surface Science* **573**, L375. 5.3.1

Ciobanu, C., Chuang, F. and Lytle, D. (2007), 'On the structure of the Si(103) surface', *http://arxiv.org/abs/0709.0753*. 5.3, 5.3

Ciobanu, C. V., Tambe, D. T. and Shenoy, V. (2004), 'Comparative study of dimer-vacancies and dimer-vacancy lines on Si(001) and Ge(001)', *Surface Science* **556**, 171. 3.3, 3.3, 3.5, 3.5

Deaven, D. M. and Ho, K. M. (1995), 'Molecular Geometry Optimization with a Genetic Algorithm', *Physical Review Letters* **75**, 288. 5.3.1, 6

Denker, U., Dashiell, M. W., Jin-Phillipp, N. Y. and Schmidt, O. G. (2002), 'Trenches around and between self assembled silicon/germanium islands grown on silicon substrates investigated by atomic force microscopy', *Materials Science and Engineering B* **89**, 166. 4.1, 4.3

Denker, U., Rastelli, A., Stoffel, M., Tersoff, J., Katsaros, G., Costantini, G., Kern, K., Jin-Phillip, N. Y., Jesson, D. E. and Schmidt, O. G. (2005), 'Lateral Motion of SiGe Islands Driven by Surface-Mediated Alloying', *Physical Review Letters* **94**, 216103. 4.1

Denker, U., Schmidt, O. G., Jin-Phillipp, N. Y. and Eberl, K. (2001), 'Trench formation around and between self-assembled Ge islands on Si', *Applied Physics Letters* **78**, 3723. 4.1, 4.2, 4.3

Denker, U., Stoffel, M. and Schmidt, O. G. (2003), 'Probing the Lateral Composition Profile of Self-Assembled Islands', *Physical Review Letters* **90**, 196102. 2

Dickinson, R. B. (2006), 'Diffusion rate limitations in actin-based propulsion of hard and deformable particles', *Biophysical Journal* **91**, 1548. 1.2, 6.1

Dickinson, R. B. and Purich, D. L. (2002), 'Clamped-filament elongation model for actin-based motors', *Biophysical Journal* **82**, 605. 1.2, 6.1

Ding, K. and Andersen, H. (1986), 'Molecular-dynamics simulation of amorphous germanium', *Physical Review B* **34**, 6987. 2.6

Drucker, J. (2002), 'Self-assembling Ge(Si)/Si(100) quantum dots', *IEEE Journal of Quantum Electronics* **38**, 975. 4.1

Drucker, J., Zhang, Y., Chaparro, S. A., Chandrashekhar, D., Mccartney, M. R. and Smith, D. J. (2000), 'Activated strain relief of Ge/Si(100) islands', *Surface Review Letters* **7**, 527. 4.1, 4.3, 4.3

Feil, H., Zandvliet, H., Tsai, M., Dow, J. and Tsong, I. (1992), 'Random and ordered defects on ion-bombarded Si(100)-(2x1) surfaces', *Physical Review Letters* **69**, 3076. 2.2, 2.5.1, 2.5.3

Floro, J. A., Chason, E., Freund, L. B., Twesten, R. D., Hwang, R. Q. and Lucadamo, G. A. (1999), 'Evolution of coherent islands in $Si_{1-x}Ge_x$ /Si(001)', *Physical Review B* **59**, 1990. 5.3.2

Floro, J. A., Chason, E., Twesten, R. D., Hawang, R. Q. and Freund, L. B. (1997), 'SiGe Coherent Islanding and Stress Relaxation in the High Mobility Regime', *Physical Review Letters* **79**, 3946. 4.1

Fujikawa, Y., Akiyama, K., Nagao, T., Sakurai, T., Lagally, M. G., Hashimoto, T., Morikawa, Y. and Terakura, K. (2002), 'Origin of the Stability of Ge(105) on Si: A New Structure Model and Surface Strain Relaxation', *Physical Review Letters* **88**, 176101. 5.3.1

Fukuda, T. and Ogino, T. (1998), 'STM study of the initial oxidation stage of Ge(100) 2x1', *Applied Physics A: Materials Science and Processing* **66**, S969. 2.5.1, 2.5.3

Gai, Z., Zhao, R. G., Ji, H., Li, X. and Yang, W. S. (1997), 'Atomic structure of high-index Ge surfaces consisting of periodic nanoscale facet', *Physical Review B* **56**, 12308. 11

Gavini, V., Knap, J., Bhattacharya, K. and Ortiz, M. (2007), 'Non-periodic finite-element formulation of orbital-free density-functional theory', *Journal of the Mechanics and Physics of Solids* **55**, 669. 1.1

Gerbal, F., Chaikin, P., Rabin, Y. and Prost, J. (2000), 'An elastic analysis of Listeria monocytogenes propulsion', *Biophysical Journal* **79**, 2259. 1.2, 6.1, 6.2

Giesen, M. (2001), 'Step and island dynamics at solid/vacuum and solid/liquid interfaces', *Progress in Surface Science* **68**, 1. 2.3.2

Jeong, H. and Williams, E. (1999), 'Steps on surfaces: experiment and theory', *Surface Science Reports* **34**, 171. 2.3.2

Johnson, H. T. and Freund, L. (1997), 'Mechanics of coherent and dislocated island morphologies in strained epitaxial material systems', *Journal of Applied Physics* **81**, 6081. 2

Kamins, T. I., Carr, E. C., Williams, R. S. and Rosner, S. J. (1997), 'Deposition of three-dimensional Ge islands on Si(001) by chemical vapor deposition at atmospheric and reduced pressures', *Journal of Applied Physics* **81**, 211. 4.1

Katsaros, G., Stoffel, M., Rastelli, A., Schmidt, O. G., Kern, K. and Tersoff, J. (2007), 'Three-dimensional isocompositional profiles of buried SiGe/Si(001) islands', *Applied Physics Letters* **91**, 013112. 4.1

Khor, K. E. and Das Sarma, S. (1997), 'Surface morphology and quantum dot self-assembly in growth of strained-layer semiconducting films', *Journal of Vacuum Science and Technology B: Microelectronics and Nanometer Structures* **15**, 1051. 5.3, 5.3

Kim, E. and Chen, C. (2002), 'Local bonding behavior and domain size relation for vacancy lines on Si(001)', *Physical Review B* **66**, 205418. 2.3.2

Köhler, U., Jusko, O., Müller, B., Horn-von Hoegen, M. and Pook, M. (1992), 'Layer-by-layer growth of germanium on Si(100): strain-induced morphology and the influence of surfactants', *Ultramicroscopy* **832**, 42. 2.1

Koo, J.-Y., Yi, J.-Y., Hwang, C., Kim, D.-H., Lee, S. and Shin, D.-H. (1995), 'Dimer-vacancy defects on the Si(001)-2x1 and the Ni-contaminated Si(001)-2xn surfaces', *Physical Review B* **52**, 17269. 2.1, 2.2, 2.3.1, 2.5.2

Kummer, M., Vögeli, B. and von Känel, H. (2000), 'Si overgrowth of self-assembled Ge clusters on Si(001) - a scanning tunnelling microscopy study', *Material Science and Engineering B69* **70**, 247. 5.2

Landree, E., Collazo-Davila, C. and Marks, L. D. (1997), 'Multi-solution genetic algorithm approach to surface structure determination using direct methods', *Acta Crystallographica* **B53**, 916. 5.3.1, 6

Lang, C., Kodambaka, S., Ross, F. M. and Cockayne, D. J. H. (2006), 'Real Time Observation of GeSi/Si(001) Island Shrinkage due to Surface Alloying during Si Capping', *Physical Review Letters* **97**, 226104. 5.2

Lasa, I., Gouin, E., Goethals, M., Vancompernolle, K., David, V., Vandekerckhove, J. and Cossart, P. (1997), 'Identification of two regions in the N-terminal domain of ActA involved in the actin comet tail formation by *Listeria monocytogenes*', *The European Molecular Biology Organization Jornal* **16**, 1531. 6.2

Lauer, P., Theriot, J. A., Skoble, J., Welch, M. D. and Portnoy, D. A. (2001), 'Systematic mutational analysis of the amino-terminal domain of the Listeria monocytogenes ActA protein reveals novel functions in actin-based motility', *Molecular Microbiology* **42**, 1163. 6.5.3

Le Thanh, V., Yam, V., Zhengb, Y. and Bouchier, D. (2000), 'Three-dimensional isocompositional profiles of buried SiGe/Si(001) islands', *Thin Solid Films* **380**, 2. 5.1, 5.2, 5.4

Lenosky, T. J., Sadigh, B., Alonso, E., Bulatov, V. V., Diaz de la Rubia, T., Kim, J., Voter, A. F. and Kress, J. D. (2000), 'Highly optimized empirical potential model of silicon', *Modeling and Simulations in Materials Science and Engineering* **8**, 825. 2

Li, F. H., Fan, Y. L., Yang, X. J., Jiang, Z. M., Wu, Y. Q. and Zou, J. (2006), 'Atomic composition profile change of SiGe islands during Si capping', *Applied Physics Letters* **89**, 103108. 5.2

Li, F. H., Tao, Z. S., Qin, J., Wu, Y. Q., Zou, J., Lu, F., Fan, Y. L., Yang, X. J. and Jiang, Z. M. (2007), 'Shape preservation of self-assembled SiGe quantum rings during Si capping', *Nanotechnology* **18**, 115708. 5.2

Li, J.-L., Liang, X.-J., Jia, J.-F., Liu, X., Wang, J.-Z., Wang, E.-G. and Xue, Q.-K. (2001), 'Spontaneous formation of ordered indium nanowire array on Si(001)', *Applied Physics Letters* **79**, 2826. 2.1

Li, K., Bowler, D. and Gillan, M. (2003), 'Tight binding studies of strained Ge/Si(001) growth', *Surface Science* **526**, 356. 2.3.2, 2.3.2

Lin, J. H., Yang, H. B., Qin, J., Zhang, B., Fan, Y. L., Yang, X. J. and Jiang, Z. M. (2007), 'Strain analysis of Ge/Si(001) islands after initial Si capping by Raman spectroscopy', *Journal of Applied Physics* **101**, 083528. 5.2

Liu, F. and Lagally, M. (1996), 'Interplay of Stress, Structure, and Stoichiometry in Ge-Covered Si(001)', *Physical Review Letters* **76**, 3156. 1.1, 2.1, 2.2, 2.2, 2.3.1, 2.3.2, 2.3.2, 2.4, 2.1, 2.3, 2.5.1

Liu, F., Wu, F. and Lagally, M. G. (1997), 'Effect of Strain on Structure and Morphology of Ultrathin Ge Films on Si(001)', *Chemical Reviews* **97**, 1045. 2.1, 2.2, 2.2, 2.3.1, 2.3.2, 2.4, 2.5.1

Loisel, T. P., Boujemaa, R., Pantaloni, D. and Carlier, M.-F. (1999), 'Reconstitution of actin-based motility of *Listeria* and *Shigella* using pure proteins', *Nature* **401**, 613. 1.2, 1.2, 6.1

Louwsma, H., Zandvliet, H., Kersten, B., Chesneau, J., van Silfhout, A. and Poelsema, B. (1997), 'Strain relaxation induced 1-dimensional and 0-dimensional structures: Bi on Ge(001)', *Surface Science* **381**, L594. 2.5.3

Marchenko, V. (1981), 'Theory of the equilibrium shape of crystals', *Soviet Physics JETP* **54**, 605. 3.3, 4

Marchenko, V. and Parshin, A. (1980), 'Elastic Properties of Crystal Surfaces', *Soviet Physics JETP* **52**, 129. 2.2, 2.4

Men, F.-K. and Hsu, C.-R. (1998), 'Ge/Si(001)-2xN: Surface stress and interaction of dimer vacancy lines', *Physical Review B* **58**, 1130. 2.2

Men, F.-K., Smith, A., Chao, K.-J., Zhang, Z. and Shih, C.-K. (1995), 'Dimer-vacancydimer-vacancy interaction on the Si(001) surface: The nature of the 2xn structure', *Physical Review B* **52**, R8650. 2.2, 2.3.1, 2.5.3, 2.5.3

Miki, K., Owen, J. H. G., Bowler, D. R., Briggs, G. A. D. and Sakamoto, K. (1999), 'Bismuth-induced structures on Si(001) surfaces', *Surface Science* **421**, 397. 2.1

Mitchison, J. M. (1950), 'Birefringence of Amoebae', *Nature* **166**, 313. 1

Mo, Y.-W. and M.G., L. (1991), 'Scanning tunneling microscopy studies of the growth process of Ge on Si(001)', *Journal of Crystal Growth* **111**, 876. 2.1

Mogilner, A. and Oster, G. (2003), 'Force generation by actin polymerization II: the elastic ratchet and tethered filaments', *Biophysical Journal* **84**, 1591. 1.2, 6.1

Natori, A., Nishiyama, R. and Yasunaga, H. (1997), 'Stability of ordered missing-dimer structures and the ordering dynamics on Si(001)', *Surface Science* **397**, 71. 2.2

Oviedo, J., Bowler, D. and Gillan, M. (2002), 'A first principles study of sub-monolayer Ge on Si(001)', *Surface Science* **515**, 483. 2.3.2, 2.3.2

Owen, J. H. G., Miki, K. and Bowler, D. R. (2003), 'Interaction between electronic structure and strain in Bi nanolines on Si(001)', *Surface Science* **527**, L177. 2.1

Pandey, K. (1985), *in* 'Proceedings of the 17-th International Conference on Physics of Semiconductors edited by D.J. Chadi and W.A. Harrison', Springer-Verlag, New York. 2.1, 2.2, 2.2, 2.3.1, 2.5.1

Park, C., Bakhitzin, R. Z., Hashizume, T. and Sakurai, T. (1994), 'Strain relief and ordering of (2n)-Bi structure on Si(100)', *Journal of Vacuum Science and Technology B: Microelectronics and Nanometer Structures* **12**, 2049. 2.1, 2.2

Poon, T., Yip, S., Ho, P. and Abraham, F. (1992), 'Ledge interactions and stress relaxations on Si(001) stepped surfaces', *Physical Review B* **45**, 3521. 1.1, 2.3.2, 3.3, 3.3, 2

Rafelski, S. M. and Theriot, J. A. (2006), 'Mechanism of polarization of Listeria monocytogenes surface protein ActA', *Proceedings of National Academy of Sciences U. S. A.* **59**, 4. 6.5.3

Raiteri, P., Migas, D. B., Miglio, L., Rastelli, A. and von Känel H. (2002), 'Critical Role of the Surface Reconstruction in the Thermodynamic Stability of {105} Ge Pyramids on Si(001)', *Physical Review Letters* **88**, 256103. 5.3.1

Rastelli, A., Kummer, M. and von Känel, H. (2001), 'Reversible Shape Evolution of Ge Islands on Si(001)', *Physical Review Letters* **87**, 256101. 1.1, 5.2, 5.3.2, 5.7, 10

Rastelli, A., Müller, E. and von Känel, H. (2002), 'Shape preservation of Ge/Si(001) islands during Si capping', *Applied Physics Letters* **80**, 1438. 5.2

Rastelli, A., von Känel, H., Albini, G., Raiteri, P., Migas, D. and Miglio, L. (2003), 'Morphological and Compositional Evolution of the Ge/Si(001) Surface During Exposure to a Si Flux', *Physical Review Letters* **90**, 216104. 2.1, 2.4

Rosenblatt, J., Agnew, B. J., Abe, H., Bamburg, J. R. and Mitchison, T. J. (1997), 'Xenopus actin depolymerizing factor/cofilin (XAC) is responsible for the turnover of actin filaments in *Listeria monocytogenes* tails', *Journal of Cell Biology* **136**, 1323. 6.2

Rutenberg, A. D. and Grant, M. (2001), 'Curved tails in polymerization-based bacterial motility', *Physical Review E* **64**, 021904. 6.1

Shenoy, V. B., Ciobanu, C. V. and Freund, L. B. (2002), 'Strain induced stabilization of stepped Si and Ge surfaces near (001)', *Applied Physics Letters* **81**, 364. 5.3.1

Shenoy, V. B., Tambe, D. T., Prasad, A. and Theriot, J. A. (2007), 'A kinematic description of the trajectories of *Listeria monocytogenes propelled by actin comet tails',* Proceedings of National Academy of Sciences U. S. A. **104**, *20. 1.2, 6.1, 6.2, 6.3, 6.2, 6.3, 6.5, 6.5.2*

Smith, A., Men, F.-K., Chao, K.-J., Zhang, Z. and Shih, C.-K. (1996), 'Scanning tunneling microscopy investigation of the dimer vacancydimer vacancy interaction on the Si(001) 2xn surface', Journal of Vacuum Science and Technology B: Microelectronics and Nanometer Structures **14**, *909. 2.2, 2.3.1, 2.5.3, 2.5.3*

Soo, F. S. and Theriot, J. A. (2005), 'Large-Scale Quantitative Analysis of Sources of Variation in the Actin Polymerization-Based Movement of Listeria monocytogenes*'*, Biophysical Journal **89**, *703. 6.2*

Spencer, B. J. and Tersoff, J. (2001), 'Stresses and first-order dislocation energetics in equilibrium Stranski-Krastanow islands', Physical Review B **63**, *205424. 2*

Stillinger, F. and Weber, T. (1985), 'Computer simulation of local order in condensed phases of silicon', Physical Review B **31**, *5262. 2.6*

Sutter, P. and Lagally, M. G. (2000), 'Nucleationless Three-Dimensional Island Formation in Low-Misfit Heteroepitaxy', Physical Review Letters **84**, *4637. 3.1*

Sutter, P., Schick, I., Ernst, W. and Sutter, E. (2003), 'Initial Surface Roughening in Ge/Si(001) Heteroepitaxy Driven by Step-Vacancy Line Interaction', Physical Review Letters **91**, *176102. (document), 1.1, 3.1, 3.1, 3.2, 3.5, 3.5, 3.6, 3.4*

Tersoff, J. (1988), 'Empirical interatomic potential for silicon with improved elastic properties', Physical Review B **38**, *9902. 2.1, 2.3.2, 2, 2.3, 2.2, 2.5.2, 2.6*

Tersoff, J. (1989), 'Modeling solid-state chemistry: Interatomic potentials for multicomponent systems', Physical Review B **39**, *5566. (document), 1.1, 2.1, 2.3.2, 2, 2.1, 2.3, 2.2, 2.5.2, 2.5.2, 2.6, 3.2, 3.1, 3.5, 5.1, 7, 5, 5.5, 5.4*

Tersoff, J. (1992), 'Missing dimers and strain relief in Ge films on Si(100)', Physical Review B **45**, *8833. 2.1, 2.2, 2.2, 2.3.1, 2.5.1*

Theriot, J. A., Mitchison, T. J., Tilney, L. G. and Protnoy, D. A. (1992), 'The rate of actin-based motility of intracellular Listeria monocytogenes *equals the rate of actin polymerization'*, Nature **357**, *257. 1.2, 6.1*

Tricher, L., Campas, L., Sykes, C. and Plastino, J. (2007), 'VASP Governs Actin Dynamics by Modulating Filament Anchoring', Biophysical Journal **92**, *1081. 6.5.2, 6.5.3*

Tromp, R. M., Ross, F. M. and Reuter, M. C. (2000), 'Instability-Driven SiGe Island Growth', Physical Review Letters **84**, *4641. 3.1*

Tsai, M.-H., Tsai, Y.-S., Chang, C., Wei, Y. and Tsong, I. (1997), 'Optimum widths of dimer vacancy lines on Si(100)-(2x1)', Physical Review B **56**, *7435. 2.3.2*

Upadhyaya, A. and van Oudenaarden, A. (2003), 'Biomimetic Systems for Studying Actin-Based Motility', Current Biology **13**, *R734. 6.5.2*

Voigtländer, B. (2001), 'Fundamental processes in Si/Si and Ge/Si epitaxy studied by scanning tunneling microscopy during growth', Surface Science Reports **43**, *127. 2.1*

Voigtländer, B. and Kästner, M. (1999), 'Evolution of the strain relaxation in a Ge layer on Si(001) by reconstruction and intermixing', Physical Review B **60**, *R5121. 2.2, 2.3.2, 2.4*

Wang, J., Arias, T. A. and Joannopoulos, J. D. (1993), 'Dimer vacancies and dimer-vacancy complexes on the Si(100) surface', Physical Review B **47**, *10497. (document), 2.2, 2.3.1, 2.5.2, 2.5.2, 2.3*

Wang, J.-Z., Jia, J.-F., Liu, X., Chen, W.-D. and Xue, Q.-K. (2002), 'Ordered Ga wires formed on Si(100)-2xn: Scanning tunneling microscopy study', Physical Review B **65**, *235303. 2.1*

Weakliem, P. C., Zhang, Z. and Metiu, H. (1995), 'Missing dimer vacancies ordering on the Si(100) surface', Surface Science **336**, *303. 2.1, 2.5.1, 2.5.2, 2.3, 2.5.2*

Webb, M. B., Men, F. K., Swartzentruber, B. S., Kariotis, R. and Lagally, M. G. (1991), 'Surface step configurations under strain: kinetics and step-step interactions', Surface Science **242**, *23. 1.1*

Wu, Y. Q., Li, F. H., Cui, J., Lin, J. H., Wu, R., Qin, J., Zhu, C. Y., Fan, Y. L., Yang, X. J. and Jiang, Z. M. (2005), 'Shape change of SiGe islands with initial Si capping', Applied Physics Letters **87**, *223116. 5.1, 5.2, 5.4*

Wu, Y. Q., Zou, J., Li, F. H., Cui, J., Lin, J. H., Wu, R. and Jiang, Z. M. (2007), 'The stability of faceted SiGe quantum dots capped with a thin Si layer', Nanotechnology **18**, *025404. 5.1, 5.2, 5.4*

Yam, V., Le Thanh, V., Zheng, Y., Boucaud, P. and Bouchier, D. (2001), 'Photoluminescence study of a bimodal size distribution of Ge/Si(001) quantum dots', Physical Review B **63**, *033313. 5.1, 5.2, 5.4*

Yang, W., Wang, X., Cho, K., Kishimoto, J., Fukatsu, S., Hashizume, T. and Sakurai, T. (1994), 'Missing-dimer complexes and dimers on the Ge(001) surface', Physical Review B **50**, *2406. 2.1, 2.5.1, 2.5.3*

Yeom, H., Sasaki, M., Suzuki, S., Sato, S., Hosoi, S., Iwabuchi, M., Higashiyama, K., Fukutani, H., Nakamura, M., Abukawa, T. and Kono, S. (1997), 'Existence of a stable intermixing phase for monolayer Ge on Si(001)', Surface Science **381**, *L533. 2.4*

Yu, B. and Oshiyama, A. (1995), 'Local bonding behavior and domain size relation for vacancy lines on Si(001)', Physical Review B **52**, *8337. 2.3.2, 2.3.2*

Zandvliet, H. (2000), 'Energetics of Si(001)', Review of Modern Physics **72**, *593. 1.1, 2.3.2*

Zandvliet, H. (2003), 'The Ge(001) surface', Physics Reports **388**, *1. 2.1, 2.5.3*

Zandvliet, H., Louwsma, H., Hegeman, P. and Poelsema, B. (1995), 'Energetics of Ni-Induced Vacancy Line Defects on Si(001)', Physical Review Letters **75**, *3890. 2.1, 2.2, 2.3.1, 2.5.1, 2.5.2*

Zandvliet, H., Schwartzentruber, B., Wulfhekel, W., Hattink, B. and Poelsema, B. (1998), 'Spontaneous formation of an ordered c(4x2)-(2x1) domain pattern on Ge(001)', Physical Review B **57**, *R6803. 2.5.1, 2.5.3*

Zhang, Z. and Metiu, H. (1993), 'Kinetic stability of missing-dimer and single-atom defects on Si(100)', Physical Review B **48**, *8166. 2.6*